

# Application of the Gaussian sum filter to magnetic field localization for achieving both accurate and efficient estimates in the case of multimodality

Sing-Chi Hsu

Master of Science Thesis



# **Application of the Gaussian sum filter to magnetic field localization for achieving both accurate and efficient estimates in the case of multimodality**

MASTER OF SCIENCE THESIS

Sing-Chi Hsu

12<sup>th</sup> June, 2024



Copyright © Delft Center for Systems and Control (DCSC)  
All rights reserved.



---

# Abstract

Magnetometers are widely equipped in smartphones. They measure the direction and the magnitude of the magnetic field of the environment. Since the measurements are not transition data, there is no drift when estimating position and orientation using a magnetometer. Furthermore, magnetic field localization using magnetometers requires no extra devices set in the environment, and this indicates the cost of localization using a magnetometer can be lower than other localization methods that need multiple devices set in the localizing area. Therefore, magnetic field localization is an interesting method for indoor localization. However, there exists a research gap in the algorithms that have been applied to magnetic field localization. In the current research, the Extended Kalman filter (EKF) and the Particle filter (PF) are applied to magnetic field localization. The EKF is more efficient than the PF, but has low accuracy when the distribution is multimodal. On the other hand, the PF is more computationally costly compared to the EKF but is more robust to the multimodality. As a result, a survey of the possible solutions to the current research gap was carried out. From this survey, Gaussian sum filter (GSF) was found to be a promising candidate as the solution to the research gap. To test the performance and assumptions of the GSF, the GSF was applied to a fully simulated magnetic field localization system and a localization system with the measurements obtained from a real-world magnetometer. The results from these simulations show that the GSF is more suitable for multimodality than the EKF. Besides, the computational cost of the GSF is found to be lower than the PF while the GSF has an equivalent or even better accuracy than the PF.



---

# Table of Contents

<b>Preface</b>	<b>xiii</b>
<b>Acknowledgements</b>	<b>xv</b>
<b>1 Introduction</b>	<b>1</b>
1-1 Background . . . . .	1
1-2 Motivation . . . . .	2
1-2-1 Multimodal distribution . . . . .	2
1-2-2 The EKF and the PF for magnetic field localization . . . . .	4
1-2-3 Research gap . . . . .	5
1-3 Organization . . . . .	6
<b>2 Preliminary knowledge of magnetic field localization</b>	<b>9</b>
2-1 Position and orientation . . . . .	10
2-1-1 World frame and body frame . . . . .	10
2-1-2 Position . . . . .	10
2-1-3 Orientation . . . . .	11
2-2 Models of magnetic field localization . . . . .	12
2-2-1 State . . . . .	13
2-2-2 Dynamic model . . . . .	13
2-2-3 Measurement model . . . . .	14
2-3 Algorithms . . . . .	18
2-3-1 Extended Kalman Filter (EKF) . . . . .	18
2-3-2 Particle filter (PF) . . . . .	20

<b>3</b>	<b>Gaussian sum filter and its modified form for magnetic field localization</b>	<b>23</b>
3-1	General form of the GSF . . . . .	23
3-1-1	Gaussian mixture . . . . .	23
3-1-2	Gaussian sum filter (GSF) . . . . .	24
3-2	The GSF for magnetic field localization . . . . .	27
<b>4</b>	<b>Simulation results of fully-simulated magnetic field localization with the GSF applied as an estimator</b>	<b>31</b>
4-1	Settings kept constant through all simulations . . . . .	31
4-1-1	Trajectory . . . . .	31
4-1-2	Models . . . . .	32
4-1-3	Algorithms . . . . .	33
4-2	Simulation results . . . . .	36
4-2-1	Varied initial error $\epsilon_0$ . . . . .	38
4-2-2	Varied numbers of Gaussian components of the GSF $M_{GSF}$ . . . . .	41
4-2-3	Varied initial covariance matrices of the GSF $P_{1 1}^i$ . . . . .	44
4-3	Conclusion . . . . .	48
<b>5</b>	<b>Simulation results of magnetic field localization with real-world magnetometer measurements and the GSF applied as an estimator</b>	<b>49</b>
5-1	Choices of the parameters for building the magnetic field map . . . . .	50
5-2	Settings kept constant through all simulations . . . . .	51
5-2-1	Trajectory . . . . .	52
5-2-2	Models . . . . .	52
5-2-3	Algorithms . . . . .	53
5-3	Simulation settings and results . . . . .	54
5-3-1	Varied initial error $\epsilon_0$ . . . . .	55
5-3-2	Varied numbers of Gaussian components of the GSF $M_{GSF}$ . . . . .	57
5-3-3	Varied initial covariance matrices of the GSF $P_{1 1}^i$ . . . . .	60
5-4	Conclusion . . . . .	63
<b>6</b>	<b>Conclusion</b>	<b>65</b>
<b>A</b>	<b>Measurement model</b>	<b>69</b>

<b>B</b>	<b>Magnetic field map selection process</b>	<b>71</b>
B-1	Conditional distribution for evaluation . . . . .	72
B-1-1	Full-rank Gaussian process (GP) . . . . .	72
B-1-2	Reduced-rank Gaussian process . . . . .	73
B-2	Evaluation methods . . . . .	74
B-3	Evaluation results . . . . .	76
B-3-1	Length scale $l_{SE}$ . . . . .	79
B-3-2	$\sigma_{SE}$ . . . . .	80
B-3-3	Down sampling the data . . . . .	81
B-3-4	Measurement noise $\sigma_m$ . . . . .	81
B-3-5	Final decision of the parameters . . . . .	83
<b>C</b>	<b>Unimodal Gaussian distribution</b>	<b>85</b>
C-1	Joint distribution of Gaussian variables . . . . .	86
C-2	Marginal and conditional distributions of Gaussian variables . . . . .	86
<b>D</b>	<b>Extended Kalman filter</b>	<b>87</b>
D-1	Kalman filter (KF) . . . . .	87
D-2	Extended Kalman filter . . . . .	89
D-3	Analytical expression of the general form of the EKF . . . . .	90
D-4	Extended Kalman filter for magnetic field localization . . . . .	90
<b>E</b>	<b>Particle filter</b>	<b>93</b>
<b>F</b>	<b>Gaussian sum filter</b>	<b>97</b>
<b>G</b>	<b>Analysis of the performance of the GSF in Section 4-2-3 and 5-3-3</b>	<b>99</b>
G-1	Results from Section 4-2-3 . . . . .	99
G-2	Results from Section 5-3-3 . . . . .	101
<b>H</b>	<b>Simulation results with measurement noise <math>\sigma_m</math> set as 1</b>	<b>109</b>
H-1	Simulation results . . . . .	109
H-1-1	Varied initial error $\epsilon_0$ . . . . .	109
H-1-2	Varied number of Gaussian components of the GSF $M_{GSF}$ . . . . .	110
H-1-3	Varied initial covariance matrices of the GSF $P_{1 1}^i$ . . . . .	113
	<b>Bibliography</b>	<b>115</b>
	<b>Glossary</b>	<b>119</b>
	List of Acronyms . . . . .	119
	List of Symbols . . . . .	119



---

# List of Figures

1-1	An 1-dimensional example of multimodal distribution . . . . .	3
1-2	The change of the probability through the function $f(x) = \sin(x)$ with different covariance . . . . .	4
1-3	The relationship between the initial error and the multimodality of the magnetic field observed from a simulation result (the heat map is set with transparency for easier observation of the estimations) . . . . .	5
1-4	Comparison of time duration at each experiment of the PF and the EKF in one run in the simulation of magnetic field localization . . . . .	6
1-5	The structure of the chapters in this thesis report . . . . .	7
2-1	A flow chart of the magnetic field localization process using the reduced-rank GP . . . . .	9
2-2	An illustration of the world frame “w” and the body frame “b” at time $t_1$ and $t_2$ . . . . .	10
3-1	An 1-dimensional example of a Gaussian mixture approximating a multimodal distribution . . . . .	24
4-1	The 2-dimensional plot of the ground truth trajectory of the simulations of magnetic field localization (red arrow representing the direction of the trajectory) . . . . .	32
4-2	An example of how the GSF is designed to approximate the EKF . . . . .	35
4-3	The visualization of the algorithm initializations for the magnetic field localization with varied initial error $\epsilon_0$ . . . . .	39
4-4	The root mean squared error (RMSE) of the estimated trajectories of the algorithms under different values of initial errors $\epsilon_0$ for the magnetic field localization . . . . .	40
4-5	The estimations of the algorithms at $t = 2$ with varied initial error $\epsilon_0$ . . . . .	41
4-6	The possible trade-off when increasing the number of Gaussian components of the GSF . . . . .	42

4-7	The visualization of the algorithm initializations for the magnetic field localization with varied numbers of Gaussian components of the GSF $M_{GSF}$ . . .	43
4-8	The RMSE of the estimated trajectories of the algorithms under different numbers of Gaussian components of the GSF for the magnetic field localization	44
4-9	The time duration of each algorithm at each value of the number of Gaussian components $M_{GSF}$ . . . . .	45
4-10	The visualization of the algorithm initializations for the magnetic field localization with varied initial covariance matrices of the GSF (Initial error = 0.1) . . . . .	46
4-11	The RMSE of the estimated trajectories of the algorithms under different values of initial GSF covariance matrices for the magnetic field localization (Initial error = 0.1) . . . . .	47
4-12	The visualization of the algorithm initializations for the magnetic field localization with varied initial covariance matrices of the GSF (Initial error = 0.2) . . . . .	47
4-13	The RMSE of the estimated trajectories of the algorithms under different values of initial GSF covariance matrices for the magnetic field localization (Initial error = 0.2) . . . . .	48
5-1	The norm of the measurements from the real-world magnetometer . . . . .	50
5-2	The structure of Chapter 4 and Chapter 5 (Similar sections are without dashed outline) . . . . .	51
5-3	The true trajectory to estimate (arrow represents the direction of the trajectory)	52
5-4	The estimated trajectory through dead reckoning . . . . .	53
5-5	The illustration showing how the trajectories are analyzed partially . . . . .	56
5-6	The initialization of the EKF and the GSF with varied values of initial error $\epsilon_0$	57
5-7	The RMSE of the estimated trajectories from different algorithms under varied values of initial error $\epsilon_0$ . . . . .	58
5-8	The distribution estimated by the algorithms when $t = 2$ under varied values of initial error $\epsilon_0$ . . . . .	59
5-9	The initialization of the EKF and the GSF with different values for the number of the Gaussian components of the GSF $M_{GSF}$ . . . . .	60
5-10	Time duration of the algorithms under different values of the number of Gaussian components of the GSF $M_{GSF}$ . . . . .	61
5-11	The RMSE of the estimated trajectories of different algorithms under varied values of the number of the Gaussian components of the GSF $M_{GSF}$ . . . . .	62
5-12	The visualization of the algorithm initializations for the magnetic field localization with the smallest and largest initial covariances the GSF (Initial error = 0.07) . . . . .	63
5-13	The illustration showing the last 50% of the trajectory compared with the whole trajectory . . . . .	63
5-14	The RMSE of the estimated trajectories of different algorithms under varied values of the initial covariances of the GSF $P_{1 1}^i$ . . . . .	64

B-1	The parts of the data from the data gathered through real-world measurement	75
B-2	An illustration showing how the data set is divided into a training data set and a test data set	76
B-3	The measurement data used for map training	78
B-4	The RMSE of the trajectory with different ranges for localization	79
B-5	The heat map of the trained magnetic field map with varied range for localization	79
B-6	A heat map showing the norm value of the true magnetometer measurement in different positions	80
B-7	The norm of the magnetometer measurements corresponding to their positions	84
F-1	An example of the GSF with different shapes designed for the initial arrangement of the Gaussian components	98
G-1	The indices of the 4 Gaussian components which were initially closest to the ground truth (marked with white numbers)	100
G-2	The weights change through time for different initial covariance values of the Gaussian components of the GSF	101
G-3	The RMSE of the Gaussian components of the GSF that were initially closest to the ground truth	102
G-4	The max eigenvalues of the covariance matrices change through time for different initial covariance values of the Gaussian components of the GSF	103
G-5	The max eigenvalues of the covariance matrices change through time for different initial covariance values of the Gaussian components of the GSF (enlarged two-dimensional plots of the figures shown in Figure G-4)	104
G-6	The indices of the 4 initially closest Gaussian components and the ground truth	104
G-7	The weights change through time for different initial covariance values of the Gaussian components of the GSF	105
G-8	The RMSE of the estimated trajectories of Gaussian components and the GSF under varied values of the initial covariances of the GSF $P_{11}^i$	106
G-9	The max eigenvalues of the covariance matrices change through time for different initial covariance values of the Gaussian components of the GSF	107
H-1	The RMSE of the estimated trajectories of different algorithms under varied values of initial error $\epsilon_0$	110
H-2	Time duration of the algorithms under different values of the number of Gaussian components of the GSF $M_{GSF}$	111
H-3	The RMSE of the estimated trajectories of different algorithms under varied values of the number of the Gaussian components of the GSF $M_{GSF}$	112
H-4	The RMSE of the estimated trajectories of different algorithms under varied values of the initial covariances of the GSF $P_{11}^i$	113



---

## List of Tables

4-1	Initialization of the algorithms for the simulations of the magnetic field localization . . . . .	37
5-1	Final decision of the parameters for establishing the magnetic field map using the reduce-rank GP . . . . .	51
B-1	Magnetic field map evaluation results with varied ranges . . . . .	78
B-2	Magnetic field map evaluation results with varied length scale $l_{SE}$ . . . . .	80
B-3	Magnetic field map evaluation results with varied measurement noise $\sigma_{SE}$ . . . . .	81
B-4	Magnetic field map evaluation results with varied data sizes for map estimation . . . . .	82
B-5	Magnetic field map evaluation results with varied measurement noise $\sigma_m$ . . . . .	82
B-6	Final decision of the parameters for establishing the magnetic field map using the reduce-rank GP . . . . .	83
H-1	Parameters for building the magnetic field map using reduced-rank GP . . . . .	109



---

# Preface

The idea of this project was established after the discussion with my daily supervisor Frida Viset about the multimodality concern in magnetic field localization based on her previous research. Taking this concern as a start of the research, a literature review was carried out for a survey of possible solutions.

During the discussion with Frida and my supervisor dr. Manon Kok while building up this survey, the idea and direction for the thesis project became clearer and eventually resulted in the investigation of algorithms that can outperform the accuracy of the EKF and the efficiency of the PF, which are algorithms that were employed in magnetic field localization.

After the literature survey, the GSF was concluded to be a potential solution to the research gap and was thus implemented into magnetic field localization for study.

The study started with extending the simulations published in [38] as my research assignment. Besides comparing the results of the GSF to the previous works, several trials were also conducted for the discussion of the properties of the GSF.

Following the work done in my research assignment, the simulations were later expanded with real-world magnetometer measurements implemented to strengthen the discussion made of the GSF, which were collected by Frida Viset, Gustaf Hendeby, and Ola Johansson at Linköping University.



---

# Acknowledgements

I would like to express my gratitude to my supervisor, Manon Kok, for instructing me through my thesis project. Her inspiring suggestion helped me break through the bottlenecks I encountered during my research.

I would also like to show my appreciation to my daily supervisor, Frida Viset, for her constant guidance on my research. Without her instruction, I would have struggled during my thesis project dealing with relentless difficulties. Her patience and helpful advice allowed me to complete this thesis project smoothly.

Moreover, I would like to thank my parents for providing me with persistent support through my study abroad. Their effort enabled me to accomplish my pursuit of my studies with little concern about a lot of uncertainties in life.

Finally, I would like to acknowledge my boyfriend, Kung-Han Lee, for his support during my time studying abroad. His encouragement and consolation helped me through the tough times while working hard to achieve my studies in a foreign country.

Delft University of Technology

Hsu, Sing-Chi

12<sup>th</sup> June, 2024



---

# Chapter 1

---

## Introduction

### 1-1 Background

Localization is a widely studied field in both outdoor and indoor environments. For outdoor localization, Global navigation satellite system (GNSS) is one of the broadly applied techniques [11]. Global positioning system (GPS), one of the two core constellations of GNSS, is a USA-operated well-known positioning system that utilizes satellites for positioning the target on the Earth. GNSS is widely applied for military and commercial use. This system is applied to, for example, navigation, terrain awareness warning systems, and timing [11]. For indoor localization, there are also various applications for multiple purposes. For example, the location of the customers in a building could be utilized to analyze where the customers are and allow themselves to receive more suited advertisements and notifications according to their current standing area [41]. Another example is the localization of the patients and workers in a hospital. With the location information of the patients, it will allow the staff to reach them more easily. Besides, emergency notifications can be more accurately sent to workers that are in the range close to the event to avoid spamming all the workers in the building with a large amount of irrelevant notifications [41]. Furthermore, there is an increase in the use of automated machines with the implementation of smart manufacturing [4]. Therefore, the localization of machines in indoor manufacturing environments, such as unmanned robots for transporting materials, is important for the management of the manufacturing process. As a result, indoor localization is a research field with large potential and a promising future.

Although the positioning system using GPS is well developed, it is not applicable to indoor environments due to the existence of building walls that will block the radio signal that the GPS relies on [5].

As a result, multiple indoor localization systems have been developed by researchers over time as alternatives. For example, inertial measurement unit (IMU) [31], WiFi

[40, 3], and ZigBee [19] are some of the techniques applied to substitute the role of GPS in indoor localization. Some localization systems require additional devices set in the indoor environment, such as localization systems employing WiFi or ZigBee. The additional equipment represents extra cost in such localization systems. Therefore, the idea of utilizing only the sensors that are already equipped on smartphones raised the interest of researchers [25, 31, 23].

The sensors that are often seen equipped in smartphones are accelerometers, gyroscopes, cameras, and magnetometers [22]. By integrating the measurements from the accelerometers and gyroscopes, the position and orientation could be estimated. However, the accuracy could be low due to the drift caused by the integration of the existing noise in the measurement signals and inevitable process noise while estimating [7, 16]. Fortunately, a magnetometer, which is also equipped in most smartphones, measures the direction and magnitude of the magnetic field and can be used for position and orientation estimation.

Since modern buildings contain metallic materials that are either building materials, such as the steel framing system and the beams and columns, or equipped as furniture, the anomalies of the magnetic field in a building could be utilized for localization[8]. Because the measurements of a magnetometer are not deviation values, such as acceleration and the deviation of orientation, the position and orientation estimation using magnetometer measurements will not encounter drift. As a result, it can be applied to calibrate the unwanted drift from the integration of the noises while calculating the position and orientation from the measurements of accelerometers and gyroscopes. Localizing using magnetometers is proved to be feasible in one-dimensional [10], two-dimensional [30, 27], and three-dimensional indoor localization [37]. Localization using magnetic field measurement is similar to terrain navigation, a magnetic map has to be built beforehand by using, for instance, a reduced-rank Gaussian process [28]. With the established map, the position and orientation can be estimated by comparing the measurements from the magnetometer and the estimated position and orientation through iterations over time.

## 1-2 Motivation

Currently, two algorithms have been applied to magnetic field localization for position and orientation estimation, the Extended Kalman filter (EKF) [38] and the Particle filter (PF) [30]. The research gap addressed in this thesis exists in the disadvantages of these algorithms, multimodal distributions and computational cost.

### 1-2-1 Multimodal distribution

A multimodal distribution is a distribution that has to be described with multiple means and corresponding variances or covariances. An example of a multimodal distribution of 1-dimensional data is shown in Figure 1-1. As there exist three separate peaks,

it indicates that the distribution of this data should be described with at least three means.

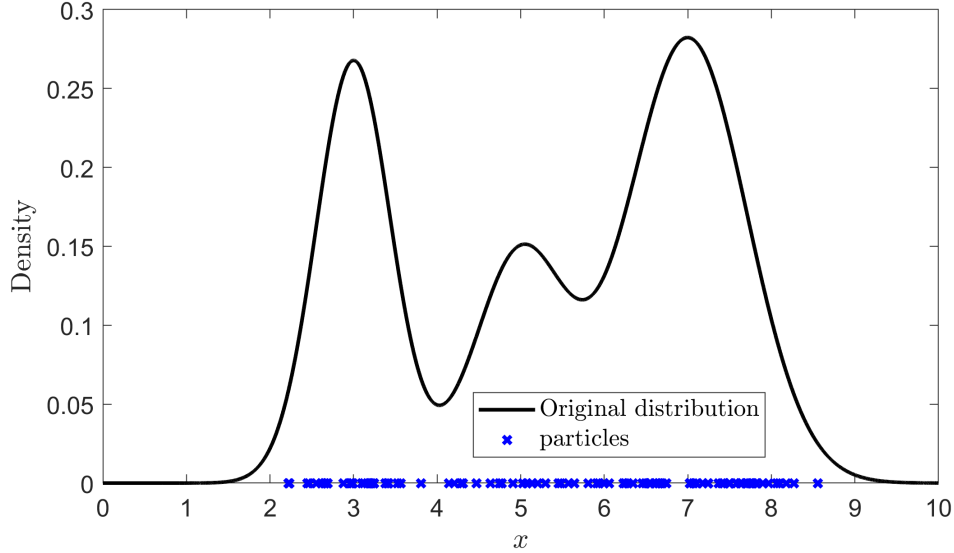


**Figure 1-1:** An 1-dimensional example of multimodal distribution

The measurement model of magnetic field localization could lead to multimodal distributions. The derivation of the close form of the magnetic field localization measurement model, given in Appendix A, shows that the resulting model is a function of the multiplication of sinusoidal functions of positions. When the function is periodic, the distribution of the input given the output of this function could be multimodal. This happens especially when the distribution of the input value has a large covariance. The reason for this phenomenon is shown with a simple numerical example applying the weight update of the PF using prior sampling.

Suppose there is a system with no dynamic model and a measurement model

$$y = f(x) = \sin(x), \quad (1-1)$$

where  $y$  is the output of the function and  $x$  is the input of the function with covariance  $\sigma_x^2$ . Assume the received output is  $y = 0$ , the distribution  $p(y = 0|x)$  will be multimodal with at least two peaks as shown by the blue bars in 1-2a. This is because the periodic function has non-unique outputs. When the distribution of  $x$  is with small covariance  $\sigma_x$  as shown by the orange bars in Figure 1-2a, the resulting update of the weights will be kept as unimodal as shown by the yellow bars in Figure 1-2a as long as the covariance of  $x$  is small. Therefore, the newly sampled particles depending on this situation will still be in a Gaussian distribution.

However, when the covariance of the  $x$  is larger, with a value of 1 as shown in Figure 1-2b, the resulting distribution will not be that ideal. As shown in Figure 1-2b, the large covariance reaches to larger region and makes the weight update result in a non-Gaussian distribution, as shown by the yellow bars in Figure 1-2b. Moreover, if only looking at a part of the non-Gaussian distribution shown in Figure 1-2b, it can be

seen as a distribution similar to a Gaussian distribution. Therefore, the non-Gaussian distribution that exists in magnetic field localization can be assumed to be multimodal.

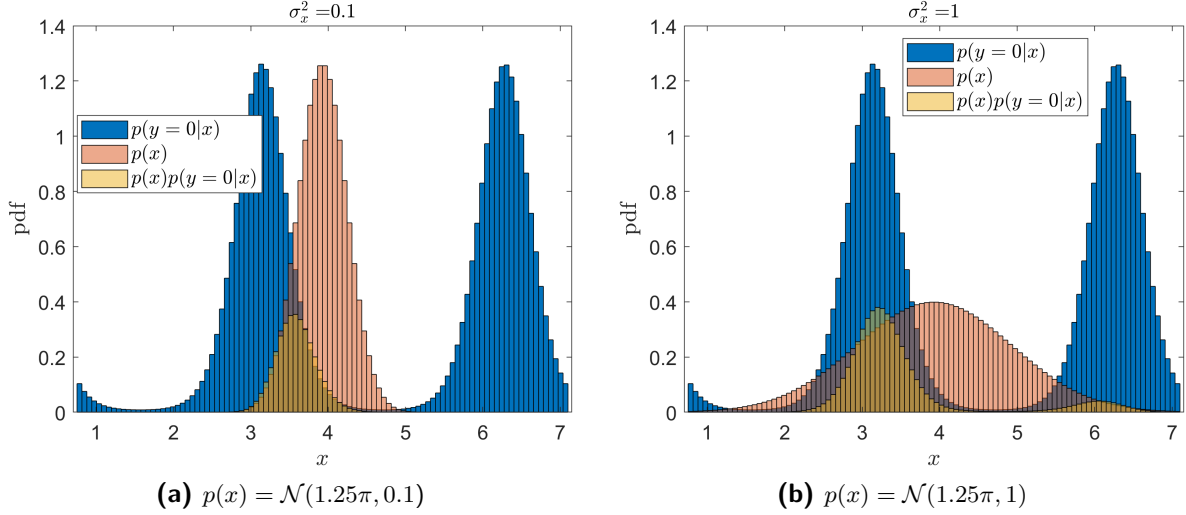


**Figure 1-2:** The change of the probability through the function  $f(x) = \sin(x)$  with different covariance

### 1-2-2 The EKF and the PF for magnetic field localization

The EKF has been employed for magnetic field localization by Viset et al. [38] and was proved to be accurate when the initial uncertainty is low. However, it is worth noticing that, as often discussed [20, 14, 21, 34], the EKF is not an ideal algorithm for systems that have multimodal distributions as it is heavily based on the assumption that all distributions are unimodal Gaussian distributions. Therefore, when the initial uncertainty is large enough to trigger the multimodal distributions, the EKF might fail in position and orientation estimation.

On the other hand, Solin et al. localized pedestrians with the PF and magnetic terrain as a PF is often used for terrain navigation[30]. The results revealed that the algorithm was capable of providing localization results within the acceptable range of error in distance. As the PF utilizes particles to describe the distributions, it is not limited to certain types of distributions. However, the amount of particles in this estimator could lead to high computational complexity.

Figure 1-3 is an example of simulated magnetic field localization where the PF is capable of illustrating the distribution when it is multimodal but the EKF does not have the estimation correctly describing such distribution. The results are from the modified code that is based on previous research in magnetic field localization [38]. As shown in Figure 1-3, the distribution described by the particles of the PF shows the multimodality when the initial error reaches 1. This shows the larger the initial error is set in the simulation, the more possible the system shows multimodality. As the EKF has larger root mean squared error (RMSE) when the initial error grows, it is indicated that when the multimodality is more likely to happen the EKF might

have lower accuracy. Such a result reflects the concern that the EKF might fail in estimating correctly when multimodal distributions exist. While the PF is suitable

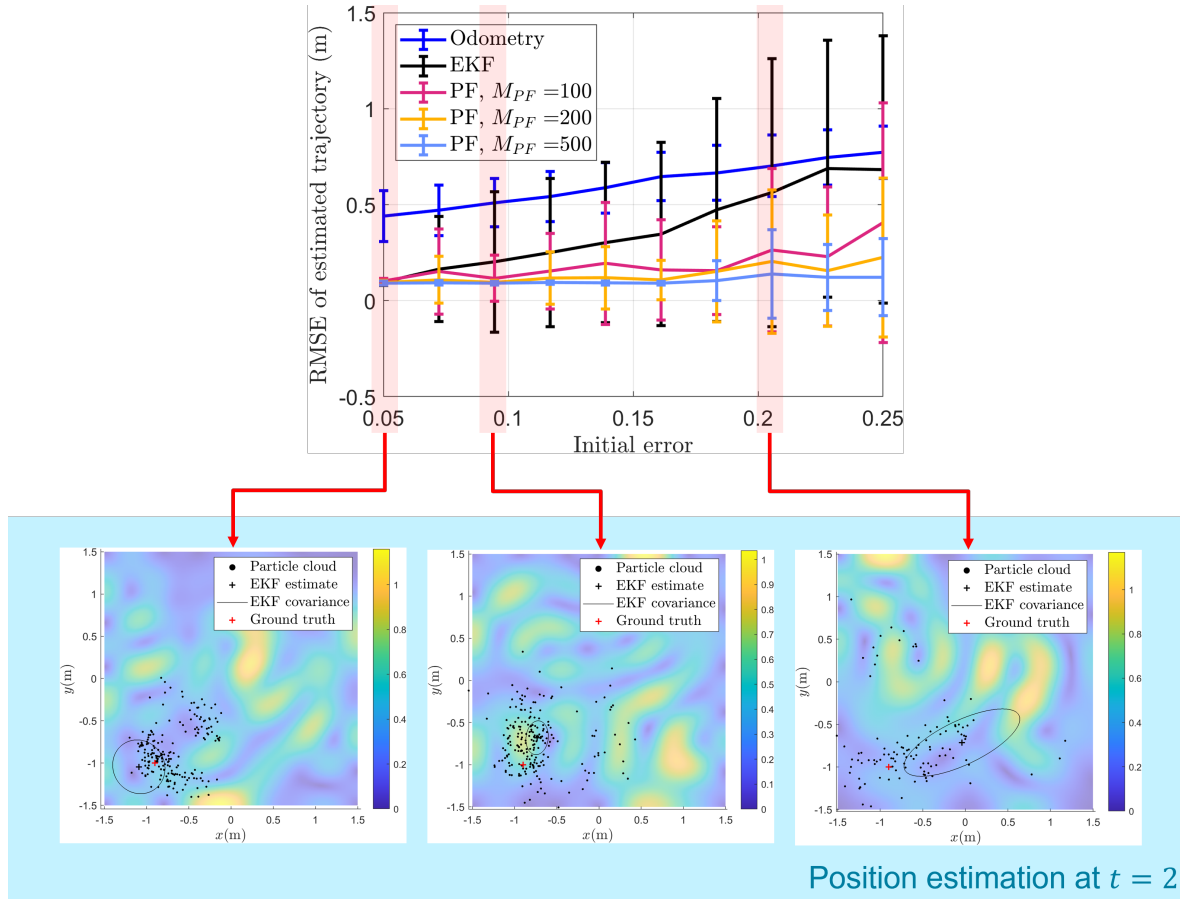


**Figure 1-3:** The relationship between the initial error and the multimodality of the magnetic field observed from a simulation result (the heat map is set with transparency for easier observation of the estimations)

for the multimodality of the estimation using magnetic field localization, it is also considered a high computational cost algorithm compared with the EKF (as shown in Figure 1-4). This can be problematic when running such an algorithm on low-cost devices, such as smartphones.

### 1-2-3 Research gap

To the best of the author's knowledge, there is no research applying an algorithm that is more suitable for multimodality but more efficient than the PF to magnetic field localization. As a result, in magnetic field localization, there exists a research gap in that there is no algorithm that is suitable for multimodality but also less computationally costly yet applied for position and orientation estimation.

Several algorithms were applied in other research for dealing with multimodality, such as the Gaussian sum filter (GSF)[1], the Uniformly random design based Gaussian sum

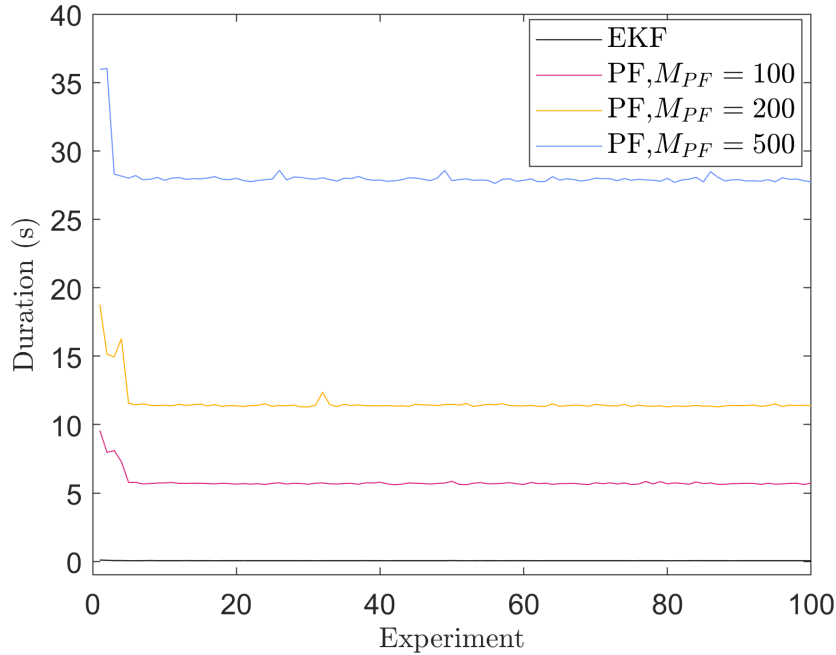


**Figure 1-4:** Comparison of time duration at each experiment of the PF and the EKF in one run in the simulation of magnetic field localization

filter (UGSF)[42], and the Unscented particle filter (UPF)[35]. These algorithms are all based on the GSF. In the GSF, the Gaussian components of the GSF are updated using the time and measurement updates adopted from the EKF parallelly. Since the GSF does not assume the distribution of the state to be an unimodal Gaussian distribution and the number of the Gaussian components  $M_{GSF}$  needed in this algorithm is much lower than the number of the particles of the PF, the GSF is a potential solution for the research gap mentioned previously. As a result, the GSF is chosen as the algorithm to be studied acting as the potential solution to the current research gap in this thesis project.

### 1-3 Organization

In this thesis report, several preliminary knowledge from previous research will be first introduced in Chapter 2. The notation for the position and orientation used in magnetic field localization will be presented in Section 2-1. The models of magnetic field localization will be explained in Section 2-2, and the algorithms that have been applied to magnetic field localization will be shown in Section 2-3.

An introduction to the GSF, the considered potential solution to the research gap, will be given in Chapter 3. In Section 3-1, the general form of the GSF will be introduced. Later, a modified GSF for magnetic field localization will be shown with analytical expression.

After the necessary preliminary knowledge and the introduction of the GSF are given,

the settings and the simulation results of a completely simulated magnetic field localization system with the GSF as the position and orientation estimator will be discussed in Chapter 4. In this chapter, there were 3 simulations run with some settings varied. At the beginning of this chapter, the settings kept constant in these 3 simulations will be first shown in Section 4-1. Later on, the unique settings of each simulation will then be explained separately with the discussion of the simulation results in Section 4-2. At the end of this chapter, a conclusion for these simulations will be given in Section 4-3.

Following the introduction and the discussion of the purely simulated magnetic field localization system with the GSF applied as an estimator, the simulations with the GSF applied to the magnetic field localization system with real-world magnetometer measurements will be introduced and discussed in Chapter 5. Different from Chapter 4, this chapter will start with an introduction of the parameters selected for building the magnetic field map using the reduced-rank Gaussian process (GP). After this section, the following sections are similar to Chapter 4, with the settings kept constant through the simulations introduced in Section 5-2 and the simulation results discussed in Section 5-3. At the end of this chapter is the conclusion for the simulations where the measurements were from real-world magnetometers.

Finally, a conclusion and a discussion of the possible future work of this thesis project will be given in Chapter 6.

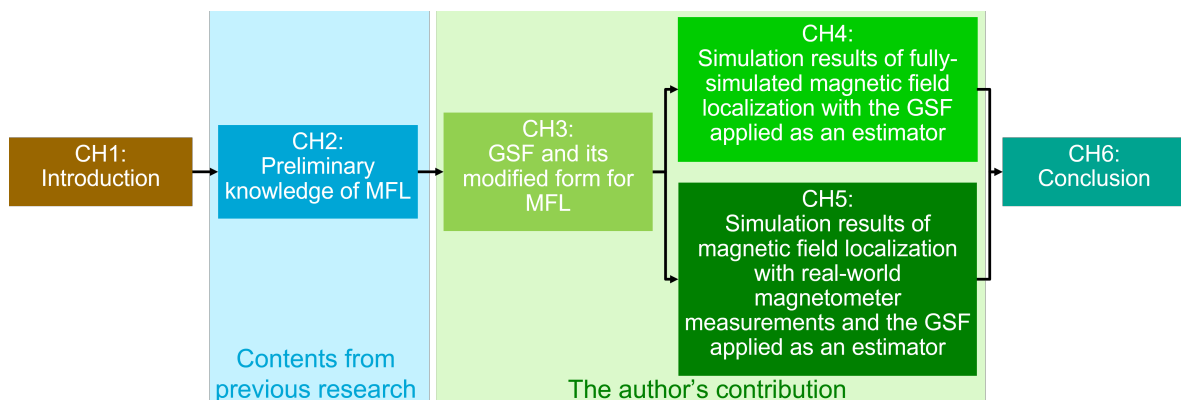


**Figure 1-5:** The structure of the chapters in this thesis report



# Preliminary knowledge of magnetic field localization

A magnetic field localization is an indoor localization system with the measurements of magnetometers, accelerometers, and gyroscopes as the input for the estimation of the position and orientation. Before carrying out the estimation online, a magnetic field map has to be estimated first, which is the offline mapping procedure marked with blue outlines in Figure 2-1. The resulting estimated magnetic field map from this offline mapping is a key element for the measurement model of the position and orientation estimation.

The online position and orientation estimation will be carried out with the results of the offline mapping and the online measurements. This online procedure is marked with green outlines in Figure 2-1.

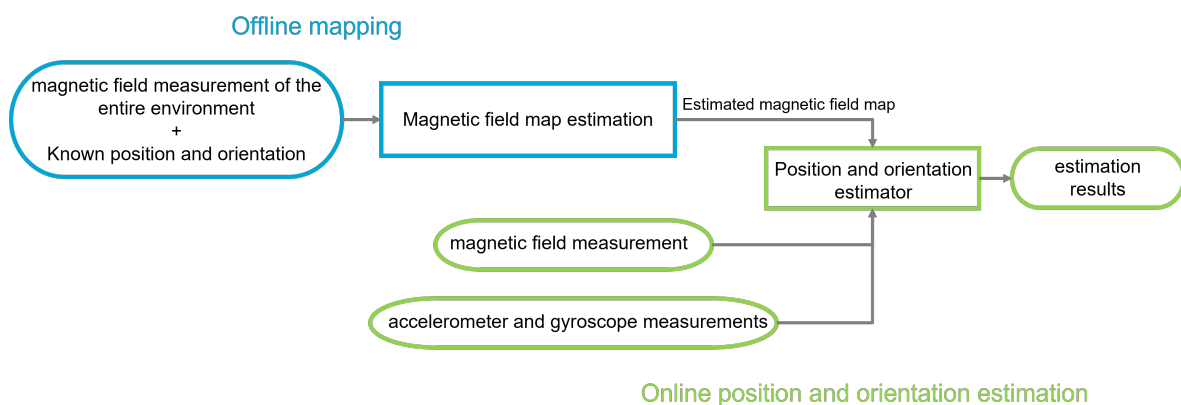


**Figure 2-1:** A flow chart of the magnetic field localization process using the reduced-rank Gaussian process (GP)

In this chapter, the notation of the position and the orientation will be introduced

in Section 2-1. Furthermore, the dynamic and measurement models that have been implemented in magnetic field localization for position and orientation estimation will be explained in Section 2-2. In this section, the learning of the map using a full-rank and reduced-rank GP will be mentioned when presenting the measurement model. At the end of this chapter, the algorithms, the Extended Kalman filter (EKF) and the Particle filter (PF), that have been applied in previous studies of magnetic field localization as position and orientation estimators will be introduced in Section 2-3.

## 2-1 Position and orientation

### 2-1-1 World frame and body frame

To introduce the notations for positions and orientations, it is worth noticing the difference between the world frame and a body frame. The body frame, represented as “b”, rotates with the target object’s orientation and the origin of the body frame moves with the object. The world frame, represented as “w”, will not change over time and is the coordinate that we would like to navigate in [38]. An example of the relationship between the world frame and the body frame is illustrated in Figure 2-2, where the body frame moves from time  $t_1$  to  $t_2$  while the world frame stays at the same location.

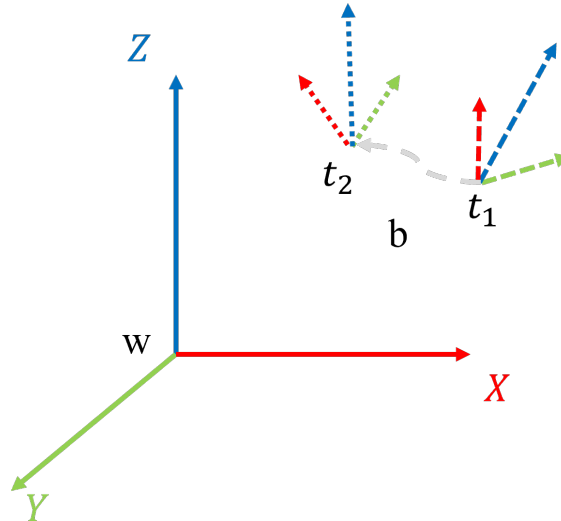


**Figure 2-2:** An illustration of the world frame “w” and the body frame “b” at time  $t_1$  and  $t_2$

### 2-1-2 Position

To localize the target object using magnetometers, the estimation of position and orientation is an important process of the algorithm. In this report, the position and

orientation are considered to be estimated in a three-dimensional space. To represent the three-dimensional position, the notation

$$p_t^w = [p_{x,t}^w \quad p_{y,t}^w \quad p_{z,t}^w]^T \in \mathbb{R}^3, \quad (2-1)$$

has been employed, where  $p_t^w$  represents the position  $p$  at time  $t$  in the world frame “w” and the elements in  $p_t^w$  represent the scalar values that indicate the target object’s position at each axis of the three-dimensional coordinates,  $X$ ,  $Y$ , and  $Z$ .

### 2-1-3 Orientation

As introduced in Section 2-1-1, the body frame has been defined as the coordinate that has its origin following the target object and the axes following the target object’s rotation corresponding to its position. The orientation here has been defined as the difference in angles between the body frame and the fixed world frame. Since here only the rotation is considered, the length of the position vector in  $\mathbb{R}^3$  will not change after rotated with the orientation. Such a group of rotations has been defined as the special orthogonal group  $SO(3)$ . There exist multiple methods for the representation of orientation, such as rotation matrices, rotation vectors, Euler angles, and unit quaternions[16]. Here, unit quaternions have been chosen as the representation for the linearization point of the orientation since this research is based on previous research [38] and [18], which also used unit quaternions for some of the orientation representation. Furthermore, rotation matrices will be used in the mathematical derivation in the following chapters when discussing the models and algorithms. Below is a more detailed definition of rotation matrices and unit quaternions.

- **Rotation matrices**

A rotation matrix,  $R$ , is a  $3 \times 3$  matrix that can represent the orientation of a point in a three-dimensional space [16]. Moreover, it has to be orthogonal, that is  $RR^T = \mathcal{I}_3$ ,  $\det R = 1$ , and  $R \in \mathbb{R}^{3 \times 3}$ .

In this report, the rotation matrix representing the difference between the world and a body frame will be denoted as  $R_t^{wb}$ . The upper notation “wb” means the matrix can rotate a position in a body frame “b” to the world frame “w”, and the lower notation  $t$  shows the time step since the body frame is time variant. For instance, if  $p_t^b$  is a position vector in a body frame at time  $t$ , then its equivalent position vector in the world frame at time  $t$  will be

$$p_t^w = R_t^{wb} p_t^b. \quad (2-2)$$

- **Unit quaternions**

Likewise, unit quaternions could also represent the orientation. A unit quaternion is noted as

$$q = [q_0 \quad q_1 \quad q_2 \quad q_3]^T = \begin{bmatrix} q_0 \\ q_v \end{bmatrix}, \quad (2-3)$$

where  $q \in \mathbb{R}^4$  and  $\|q\|_2 = 1$  [16].

Unlike rotation matrices, the position coordinate transformation using unit quaternions is not simply a linear algebra multiplication. Instead, quaternion multiplication is employed for the transformation, which is noted as  $\odot$ . Given two vectors,  $p = [p_0 \ p_v]^\top \in \mathbb{R}^4$  and  $q = [q_0 \ q_v]^\top \in \mathbb{R}^4$ , the quaternion multiplication is as

$$p \odot q = \begin{bmatrix} p_0 q_0 - p_v \cdot q_v \\ p_0 q_v + q_0 p_v + p_v \times q_v \end{bmatrix} = p^L q = q^R p, \quad (2-4)$$

where

$$p^L \triangleq \begin{bmatrix} p_0 & -p_v^\top \\ p_v & p_0 \mathcal{I}_3 + [p_v \times] \end{bmatrix}, \quad q^R \triangleq \begin{bmatrix} q_0 & -q_v^\top \\ q_v & q_0 \mathcal{I}_3 - [p q_v \times] \end{bmatrix}, \quad [q_v \times] \triangleq \begin{bmatrix} 0 & -q_{v,3} & q_{v,2} \\ q_{v,3} & 0 & -q_{v,1} \\ -q_{v,2} & q_{v,1} & 0 \end{bmatrix}. \quad (2-5)$$

Similar to rotation matrices, the unit quaternion for the rotation from a body frame to the world frame is denoted as  $q^{\text{wb}}$ .

### Linearization

The linearization of unit quaternions has been employed in the EKF and the Gaussian sum filter (GSF) adjusted for magnetic field localization, the two algorithms that will be introduced later. Since unit quaternions are  $SO(3)$ , also termed as matrix Lie Group, an exponential map from Lie algebra can be applied to an orientation deviation in  $\mathbb{R}^3$  to represent the difference between two orientations in a quaternion form. In other words,

$$q_t^{\text{wb}} = \exp_{\mathfrak{q}}\left(\frac{\eta_t^{\text{w}}}{2}\right) \odot \tilde{q}_t^{\text{wb}}, \quad (2-6)$$

where  $\tilde{q}_t^{\text{wb}}$  is the linearization point,  $\eta_t^{\text{w}}$  is the vector in  $\mathbb{R}^3$  representing the orientation deviation in angle-axis representation,  $q_t^{\text{wb}}$  is a unit quaternion representing the true orientation, and  $\exp_{\mathfrak{q}}(\eta) = \begin{pmatrix} \cos \|\eta\|_2 \\ \frac{\eta}{\|\eta\|_2} \sin \|\eta\|_2 \end{pmatrix}$  [16].

## 2-2 Models of magnetic field localization

The models utilized for the simulations of magnetic field localization are based on the ones introduced in [38]. In this section, the state will be first introduced. Then the dynamic model and the measurement model that have been applied in [38] will be explained.

### 2-2-1 State

The state of this system is composed of the 3-dimensional position  $p_t^w$  and the orientation  $q_t^{wb}$  represented with a unit quaternion introduced in Section 2-1. The mathematical expression of the state is written as

$$x_t = \begin{bmatrix} p_t^w \\ q_t^{wb} \end{bmatrix} = \begin{bmatrix} p_{x,t}^w \\ p_{y,t}^w \\ p_{z,t}^w \\ q_{0,t}^{wb} \\ q_{1,t}^{wb} \\ q_{2,t}^{wb} \\ q_{3,t}^{wb} \end{bmatrix} \in \mathbb{R}^7, \quad (2-7)$$

where  $p_t^w \in \mathbb{R}^3$  is the 3-dimensional position in the world frame, and  $q_t^{wb}$  is the unit quaternion representing the orientation between the body frame “b” and the world frame “w” [18, 38].

### 2-2-2 Dynamic model

The development of the system over time can be mathematically described by dynamic models. When given the current states and the process noise, the future states can be calculated using the dynamic model. Here the dynamic models for position and orientation estimation that have been applied in [38] will be introduced sequentially in the following content.

#### Position

The dynamics of the position estimation have been simply modeled as the accumulation of the position change and the realization of a zero-mean Gaussian noise at each time step. In other words, the dynamic model for position can be written as

$$p_{t+1}^w = p_t^w + \Delta p_t^w + e_{p,t}^w, \quad e_{p,t}^w \sim \mathcal{N}(0, R_p) \quad (2-8)$$

where  $\Delta p_t^w$  is the difference of the position between time  $t$  and  $t+1$  and  $e_{p,t}^w$  is the zero-mean measurement noise with covariance matrix  $R_p$  [18, 38]. Notice that the noise has been assumed to be a vector of variables with the same size of  $p_t^w$  which are uncorrelated, so the covariance  $R_p$  is commonly seen to be replaced with  $\sigma_p^2 \mathcal{I}_3$ .

#### Orientation

Referring to [6], a unit quaternion can be updated by the exponential map

$$q_{t+1}^{wb} = q_t^{wb} \odot \exp_q(\Delta q_t^b), \quad (2-9)$$

where  $\Delta q_t^b$  is the deviation of the unit quaternion of time step  $t$  and  $t+1$ . Now considering the measurement noise,  $e_{q,t}^w \sim \mathcal{N}(0, R_q)$ , that acts on the orientation measurement, the dynamic model for the orientation update can be written as

$$q_{t+1}^{wb} = q_t^{wb} \odot \exp_q(\Delta q_t^b) \odot \exp_q(e_{p,t}) \cong q_t^{wb} \odot \exp_q(\Delta q_t^b + e_{p,t}) \quad (2-10)$$

[38], where the approximation  $\exp_q(\Delta q_t^b) \odot \exp_q(e_{p,t}) \cong \exp_q(\Delta q_t^b + e_{p,t})$  holds because when two vectors,  $\eta$  and  $e$ , have Euclidean norm values as 1, the approximation

$$\exp_q(\eta) \odot \exp_q(e) \quad (2-11a)$$

$$\cong \begin{bmatrix} 1 \\ \eta \end{bmatrix} \odot \begin{bmatrix} 1 \\ e \end{bmatrix} = \begin{bmatrix} 1 \\ \eta \end{bmatrix}^L \begin{bmatrix} 1 \\ e \end{bmatrix} = \begin{bmatrix} 1 - \eta_1 e_1 - \eta_2 e_2 - \eta_3 e_3 \\ \eta_1 + e_1 - \eta_3 e_2 + \eta_2 e_3 \\ \eta_2 + \eta_3 e_1 + e_2 - \eta_1 e_3 \\ \eta_3 + \eta_2 e_1 + \eta_1 e_2 + e_3 \end{bmatrix} \cong \begin{bmatrix} 1 \\ \eta_1 + e_1 \\ \eta_2 + e_2 \\ \eta_3 + e_3 \end{bmatrix} \quad (2-11b)$$

$$\cong \exp(\eta + e) \quad (2-11c)$$

holds since the value of  $\eta_i e_j$  is small compared to other elements in the matrix for all  $\{i, j\} \in \{1, 2, 3\}$ .

### 2-2-3 Measurement model

In magnetic field localization, the measurement model has been built with the position and the orientation as the inputs and the measurement of the magnetometer as the output. The model can be learned using a GP. In this localization method, the model is based on the knowledge of Maxwell's equations. In this section, a brief explanation of how a model can be learned via GP regression will be given. First, the model with the magnetic field map learned using a full-rank GP [39] will be introduced. Second, the model with the full-rank GP replaced by a reduced-rank GP will be described.

#### Gaussian process (GP) regression

Gaussian process (GP) is a distribution with the mean and the covariance as functions of the inputs, which are the train data  $x_t$  and test data  $x_t^*$  [26]. Suppose the function  $f(x_t)$  is the target to learn and there exists a zero-mean Gaussian noise  $e_t$  that makes the output of this function  $y_t$  noisy. The relationship of the output  $y_t$  and the function  $f(x_t)$  can thus be written as a model

$$y_t = f(x_t) + e_t, \quad e_t \sim \mathcal{N}(0, \sigma_y^2 \mathcal{I}), \quad (2-12)$$

where

$$f(x_t) \sim \mathcal{GP}(\mu(x_t), \kappa(x_t, x_t^*)) \quad (2-13)$$

, where  $x_t$  is the training input and  $x_t^*$  is the testing input. In magnetic field localization, the mean function  $\mu(x_t)$  is assumed to be

$$\mu(x_t) = 0, \quad (2-14)$$

and this will be applied in this thesis project.

In a GP regression, the distribution of the function  $f$  is learned given the input of test data, the output and the input of the train data. That is, the distribution

$$p(\mathbf{f}^*|X, X^*, Y) = \mathcal{N}(\boldsymbol{\mu}^*, \boldsymbol{\Sigma}^*) \quad (2-15)$$

will be learned, where the output of the train data  $Y = [y_1 \ y_2 \ \dots \ y_N]^\top$ , the input of the train data  $X = [x_1 \ x_2 \ \dots \ x_N]^\top$ , the input of the test data  $X^* = [x_1^* \ x_2^* \ \dots \ x_{N^*}^*]^\top$ , and the estimated output of the test data given the input of the test data  $\mathbf{f}^* = [f(x_1^*) \ f(x_2^*) \ \dots \ f(x_{N^*}^*)]^\top$ .

This conditional distribution can be calculated by applying Eq. (C-6e). The joint distribution can be achieved by Eq. (C-5b) and results in

$$\begin{bmatrix} Y \\ \mathbf{f}^* \end{bmatrix} \sim \mathcal{N}\left(\mathbf{0}, \begin{bmatrix} \kappa(X, X) + \sigma_y^2 \mathcal{I} & \kappa(X, X^*) \\ \kappa(X^*, X) & \kappa(X^*, X^*) \end{bmatrix}\right), \quad (2-16)$$

where

$$\kappa(X, X^*) = \begin{bmatrix} \kappa(x_1, x_1^*) & \dots & \kappa(x_1, x_{N^*}^*) \\ \vdots & \ddots & \vdots \\ \kappa(x_N, x_1^*) & \dots & \kappa(x_N, x_{N^*}^*) \end{bmatrix}. \quad (2-17)$$

The means and the covariances of the conditional distribution can then be calculated using Eq. (C-6e), which can be written as

$$\boldsymbol{\mu}^* = \kappa(X, X^*)^\top (\kappa(X, X) + \sigma_y^2 \mathcal{I})^{-1} Y, \quad (2-18a)$$

and

$$\boldsymbol{\Sigma}^* = \kappa(X^*, X^*) - \kappa(X, X^*)^\top (\kappa(X, X) + \sigma_y^2 \mathcal{I})^{-1} \kappa(X, X^*). \quad (2-18b)$$

- **Measurement model learned with the magnetic field map learned using Full-rank GP regression[38]**

By employing Maxwell's equations and classical electromagnetism, the magnetic field can be modeled with the gradient of a latent scalar potential field  $\varphi(p_t^w) \in \mathbb{R}$  since the measured signal from a magnetometer is the derivation of this potential [18]. Because the measurements from a magnetometer are under body frame "b", a rotation matrix  $R_t^{bw}$  to rotate the gradient of the potential from the world frame "w" to a body frame "b" is added. By introducing a Gaussian measurement noise  $e_{m,t}^b \sim \mathcal{N}(0, \sigma_m^2 \mathcal{I}_3)$ , the mathematical expression for the model can be written as

$$y_t^b = R_t^{bw} \nabla_p \varphi(p_t^w) + e_{m,t}^b. \quad (2-19)$$

For notation simplification, the position  $p_t^w$  will be denoted as  $p$  in the following discussion of this model.

The potential  $\varphi(p)$  has been assumed to be a realization of a Gaussian process prior

$$\varphi(p) \sim \mathcal{GP}(0, \kappa_{\text{lin}}(p, p') + \kappa_{\text{SE}}(p, p')) \quad (2-20)$$

, where  $p$  is the train position and  $p'$  is the test position. The linear kernel  $\kappa_{\text{lin}}(p, p')$  has been applied to remove the Earth's magnetic field to make the mean equal to 0 and is defined as

$$\kappa_{\text{lin}}(p, p') = \sigma_{\text{lin}}^2 p^\top p', \quad (2-21)$$

where  $\sigma_{\text{lin}}$  is the magnitude hyperparameter. The squared exponential kernel  $\kappa_{\text{SE}}(p, p')$  is defined as

$$\kappa_{\text{SE}}(p, p') = \sigma_{\text{SE}}^2 \exp\left(-\frac{\|p-p'\|_2^2}{2l_{\text{SE}}^2}\right), \quad (2-22)$$

where  $\sigma_{\text{SE}}$  is the magnitude hyperparameter and  $l_{\text{SE}}$  is the characteristic length-scale hyperparameter.

As a result, the Gaussian process prior of the gradient of the potential  $\varphi(p)$  can be written as

$$\nabla_p \varphi(p) \sim \mathcal{GP}(0, \sigma_{\text{lin}}^2 \mathcal{I}_3 + \nabla_p \nabla_{p'} \kappa_{\text{SE}}(p, p')). \quad (2-23)$$

Comparing the measurement model shown in Eq. (2-19) and the model we want to learn in a GP regression that is shown in Eq. (2-12), the conditional distribution derived from Eq. (2-23) is the target of the GP regression. Therefore, it can be used for the evaluation of the learned map. The use of this conditional distribution is introduced in detail in Appendix B when evaluating the maps built using the full-rank GP and the reduce-rank GP.

- **Measurement model learned with the magnetic field map learned using reduced-rank GP regression [38]**

Due to the concern of the computational cost for implementing the above model with computational complexity  $\mathcal{O}(n^3)$ , the reduced-rank Gaussian process has been introduced as an alternative for modeling the measurements [18]. With this method, the measurement model can be rewritten as

$$y_t^b = R_t^{\text{bw}} \nabla_p \Phi(p_t^w) m + e_{m,t}^b, \quad (2-24)$$

where the potential  $\varphi(p)$  is approximated with the set of basis functions  $\Phi(p)$  multiplying the weight vector  $m$  [38]. The set of basis functions  $\Phi(p)$  is formed by basis functions  $\phi_i$ ,  $\forall i \in \{1, 2, \dots, N_m\}$ , which can be written as

$$\Phi(p) = [p^\top \quad \phi_1(p) \quad \phi_2(p) \quad \dots \quad \phi_{N_m}(p)]. \quad (2-25)$$

The basis functions are the solutions to the eigendecomposition of the Laplace operator under Dirichlet boundary conditions

$$\begin{cases} -\nabla_p^2 \phi_i(p) = \lambda_i^2 \phi_i(p), & p \in \Omega, \\ \phi_i(p) = 0, & p \in \delta\Omega \end{cases} \quad (2-26)$$

[18], and the close form of the solution can be written as

$$\phi_i(p) = \prod_{d=1}^3 \frac{\sqrt{2}}{\sqrt{L_{u,d} - L_{l,d}}} \sin\left(\frac{\pi n_{j,d}(p_d - L_{l,d})}{L_{u,d} - L_{l,d}}\right), \quad (2-27a)$$

and

$$\lambda_i = \sum_{d=1}^3 \left(\frac{\pi n_{j,d}}{L_{u,d} - L_{l,d}}\right)^2 \quad (2-27b)$$

[38]. The gradient of the set of basis functions is analytically derived in Appendix A.

Since the gradient of the set of basis functions is deterministic with the position given as the input, the distribution of  $\nabla_p \Phi(p_t^w) m$  depends only on the distribution of the weight vector  $m$ . The distribution of the vector  $m$  is

$$m \sim \mathcal{N}(\hat{m}, \Lambda), \quad (2-28)$$

where  $\hat{m}$  is the estimated mean and  $\Lambda$  is the estimated covariance. The distribution of  $m$  is calculated by a recursive update of its mean  $\hat{m}_t$  and the covariance matrix  $\Lambda_t$  [18]. The initial values for this recursive update are set as

$$m \sim \mathcal{N}(\hat{m}_0, \Lambda_0), \quad (2-29a)$$

where  $\hat{m}_0 = 0$  and

$$\Lambda_0 = \text{diag} \left[ \sigma_{\text{lin}}^2 \mathcal{I}_3 \quad S_{\text{SE}}(\sqrt{\lambda_1}) \quad \dots \quad S_{\text{SE}}(\sqrt{\lambda_{N_m}}) \right]. \quad (2-29b)$$

The diagonal elements of the covariance of the magnetic field map  $\Lambda_0$  are calculated from the spectral density function

$$S_{\text{SE}}(\omega) = \sigma_{\text{SE}}^2 (2\pi l_{\text{SE}}^2)^{3/2} \exp\left(-\frac{\omega^2 l_{\text{SE}}^2}{2}\right), \quad (2-30)$$

where  $\sigma_{\text{SE}}$  is the magnitude hyperparameter and  $l_{\text{SE}}$  is the length scale. The update of the distribution of the vector  $m$  for  $t \in \{1, 2, 3, \dots, N_{\text{train}}\}$  can be written as

$$S_t = C_t \Lambda_{t-1} C_t^\top + \sigma_m^2 \mathcal{I}_3, \quad (2-31a)$$

$$K_t = \Lambda_{t-1} C_t^\top S_t^{-1}, \quad (2-31b)$$

$$\hat{m}_t = \hat{m}_{t-1} + K_t (R_{\text{train},t}^{\text{wb}} y_{\text{train},t}^{\text{b}} - C_t \hat{m}_{t-1}), \quad (2-31c)$$

$$\Lambda_t = \Lambda_{t-1} - K_t S_t K_t^\top, \quad (2-31d)$$

where

$$C_t = \nabla_p \Phi(p_{\text{train},t}^w). \quad (2-31e)$$

The equivalent Gaussian process prior of Eq. (2-23) can be calculated by applying the joint distribution introduced in Eq. (C-5b) and be written as

$$\nabla_p \Phi(p_t^w) m \sim \mathcal{GP}(\nabla_p \Phi(p_t^w) \hat{m}, \nabla_p \Phi(p_t^w) \Lambda (\nabla_p \Phi(p_t^w))^\top). \quad (2-32)$$

This distribution will be used to compare with the conditional distribution of the full-rank GP for the evaluation of the magnetic field approximation in Appendix B.

## 2-3 Algorithms

In this section, the two algorithms that have been applied to magnetic field localization, the EKF and the PF, will be introduced.

### 2-3-1 Extended Kalam Filter (EKF)

Viset et al. implemented the EKF to magnetic field localization [38] for position and orientation estimation. In this section, the EKF in the form adapted to magnetic field localization that has been applied in [38] will be introduced.

The EKF applied to magnetic field localization contains two main updates, the time and the measurement updates. Besides, there's an additional step to correct the linearized point at the end due to the fact that the update depends on the linearization with respect to an error state based on the state in Eq. (2-7).

- **Time update**

The time update for position and orientation is based on the dynamic models described in Section 2-2-2 and can be written as

$$\hat{p}_{t|t-1}^w = \hat{p}_{t-1|t-1}^w + \Delta p_t^w, \quad (2-33a)$$

$$\hat{q}_{t|t-1}^{wb} = \hat{q}_{t-1|t-1}^{wb} \odot \exp_q(\Delta q_t^b). \quad (2-33b)$$

The covariance matrix is updated by approximating the dynamic model with respect to the error state

$$\hat{\zeta}_{t|t-1} = \begin{bmatrix} \hat{\delta}_{t|t-1} \\ \hat{\eta}_{t|t-1}^w \end{bmatrix} = \begin{bmatrix} p_t^w - \hat{p}_{t|t-1}^w \\ \hat{\eta}_{t|t-1}^w \end{bmatrix}, \quad (2-33c)$$

where the relationship between  $\hat{\eta}_{t|t-1}$  and  $q_t^{wb}$  is  $q_t^{wb} = \exp_q(\hat{\eta}_{t|t-1}^w) \odot \hat{q}_{t|t-1}^{wb}$  [38]. The propagation of the error state can be approximated with

$$\hat{\zeta}_{t|t-1} \cong \begin{bmatrix} \hat{\delta}_{t-1|t-1}^w + e_{p,t}^w \\ \hat{\eta}_{t-1|t-1}^w + \tilde{R}_{t|t-1}^{wb} e_{q,t}^b \end{bmatrix} = \hat{\zeta}_{t-1|t-1} + e_{\text{dyn},t}, \quad e_{\text{dyn},t} \sim \mathcal{N}(0_{(N_m+9) \times 1}, Q_\zeta), \quad (2-33d)$$

where  $\hat{\zeta}_{t-1|t-1}$  denotes the error between the state and the posterior estimation and

$$Q_\zeta = \begin{bmatrix} R_p & 0_{3 \times 3} \\ 0_{3 \times 3} & R_q \end{bmatrix}. \quad (2-33e)$$

By defining the covariance of  $\hat{\zeta}_{t-1|t-1}$  as  $P_{t-1|t-1}$  and with the known noise covariance  $Q_\zeta$ , the update for the covariance matrix of  $\hat{\zeta}_{t|t-1}$  can be written as the sum of these two covariances, which is given as

$$P_{t|t-1} = P_{t-1|t-1} + Q_\zeta \quad (2-33f)$$

[38].

- **Measurement update**

The measurement update utilizes the linearized measurement model derived based on the error state 2-33c, which can be written as

$$y_t^b = \hat{R}_t^{\text{bw}} \nabla \Phi(p_{t|t-1}^w) m + H_t \zeta_t + e_{m,t}^b, \quad e_{m,t}^b \sim \mathcal{N}(0, \sigma_m^2 \mathcal{I}_3). \quad (2-34)$$

The reader could refer to [38] for a detailed mathematical representation of the linearized measurement model.

Referring to the measurement model shown at 2-34 and the measurement update of the EKF for general nonlinear systems that is presented at Eq. (D-11), the measurement update for magnetic field system can be written as

$$\hat{\zeta}_{t|t} = K_t (\hat{R}_{t|t-1}^{\text{wb}} y_t^b - \nabla \Phi(\hat{p}_{t|t-1}^w) \hat{m}), \quad (2-35a)$$

$$P_{t|t} = P_{t|t-1} - K_t S_t K_t^\top, \quad (2-35b)$$

where  $S_t = H_t P_{t|t-1} H_t^\top + \sigma_m^2 \mathcal{I}_3$  and  $K_t = P_{t|t-1} H_t^\top S_t^{-1}$ .

- **Linearized point correction**

Besides the time and measurement updates, at the last step of this magnetic field EKF algorithm, a correction for the linearized point is performed as

$$\hat{p}_{t|t}^w = \hat{p}_{t|t-1}^w + \hat{\delta}_{t|t}^w, \quad (2-36a)$$

$$\hat{q}_{t|t}^{\text{wb}} = \exp_{\mathbf{q}}(\hat{\eta}_{t|t}^w) \odot \hat{q}_{t|t-1}^{\text{wb}}, \quad (2-36b)$$

where  $\hat{\delta}_{t|t}^w$  and  $\hat{\eta}_{t|t}^w$  are from  $\hat{\zeta}_{t|t}$  calculated in the measurement update.

The detailed analytical expression of this EKF algorithm is given in Algorithm 4.

Note that the code for the EKF used in the later simulations is based on the code from [38].

### 2-3-2 Particle filter (PF)

As mentioned in Chapter 1, the PF has been applied to the magnetic field localization system by [30]. In this section, the PF that has been adapted to magnetic field localization will be introduced. Note that the following PF implemented for magnetic field localization is based on the code from [38], which is based on Algorithm 1 in [30].

In the PF applied in [38], the proposal distribution

$$\pi(x_t^i | x_{t-1}^i, y_t) = p(x_t^i | x_{t-1}^i) \quad (2-37)$$

has been chosen [30], which is named as prior sampling and will result in the most common version of PF [9]. With this proposal distribution, the weight update can be simplified from Eq. (E-3) to

$$w_{t|t}^i \propto w_{t-1|t-1}^i p(y_t | x_t^i). \quad (2-38)$$

Note that the reader is suggested to keep in mind that the symbol for the positions of the particles  $p_t^i$  could be easily confused with the probabilities, such as  $p(y_t | x_t^i)$ .

- **Time update**

The dynamic update running in each time step will run for all  $M_{PF}$  particles. The time update for the position and orientation particles are based on the dynamic models introduced in Section 2-2-2, which can be written as

$$p_t^{w,i} = p_{t-1}^{w,i} + \Delta p_{t-1} + e_{p,t}^w, \quad e_{p,t}^w \sim \mathcal{N}(0, \sigma_p^2 \mathcal{I}_3), \quad (2-39a)$$

$$q_t^{wb,i} = q_{t-1}^{wb,i} \odot \exp_q(\Delta q_{t-1}^b + e_{q,t}^{wb}), \quad e_{q,t}^{wb} \sim \mathcal{N}(0, \sigma_q^2 \mathcal{I}_3), \quad (2-39b)$$

where the upper notation  $i$  represents the  $i$ th particle. Note that the weights are not updated at this step because it is combined with the update that will be shown in the discussion of the measurement update.

- **Measurement update**

The measurement update in the PF for the magnetic field localization system runs for  $M_{PF}$  iteration, one for each particle, at each time step. With the simplified weight update shown in Eq. (2-38), the update of the weights can be written as

$$w_{t|t}^i = w_{t-1|t-1}^i p(R_t^{wb,i} y_t^b; f, \sigma_m^2 \mathcal{I}_3), \quad (2-40a)$$

where  $f = \nabla \Phi(p_t^{w,i}) \hat{m}$  and  $R_t^{wb,i}$  is a rotation matrix converted from the orientation  $q_t^{wb,i}$ .

- **Resampling**

After the dynamic and measurement updates, the weights are first normalized. Later, the particles are resampled based on the weights. The probability the particles are selected during the resampling process depends on their weights. That is, the larger the weight is, the more possible that the particle is kept, or even duplicated, for the next time step iteration. After the resampling process, the weights are again reset to  $w_{t|t}^i = 1/M$ .

- **Estimation**

The mean of the position and orientation estimation is decided by extracting the particle with the largest weight in the PF applied to the magnetic field localization system [38]. Meanwhile, the covariance of the position is updated by calculating the covariance of the particles with

$$P_t = \frac{1}{M} \sum_{i=1}^M (p_t^{w,i} - \bar{p}_t^w)(p_t^{w,i} - \bar{p}_t^w)^\top. \quad (2-41)$$

Since the PF does not assume the distributions to be unimodal Gaussian distributions as the EKF does, it can estimate systems with multimodal distributions. Furthermore, since it does not rely on linearization in the updates, it can estimate highly nonlinear systems without considering the accuracy that the linearization can achieve. However, there exist extra  $M_{PF}$  iterations in each time step, and since the value of  $M_{PF}$  is often more than 100, it could be quite inefficient when applying a PF to online estimation compared with the EKF.

The analytical expression of this PF is shown in Algorithm 6. Note that the code for the PF used in the later simulations is based on [38].



# Gaussian sum filter and its modified form for magnetic field localization

As mentioned in the motivation of this thesis project in Section 1-2, there is no algorithm that is more suitable to multimodal distributions than the Extended Kalman filter (EKF) and more efficient compared with the Particle filter (PF) applied to magnetic field localization yet to the best of the author's knowledge. The Gaussian sum filter (GSF) is found to be a promising solution to this research gap in magnetic field localization and will be introduced in this chapter.

In this chapter, the key component of the GSF, Gaussian mixture, and the general analytical expression of the GSF will be presented. Following the introduction of the GSF, the GSF that is modified for magnetic field localization will be shown in Section 3-2.

### 3-1 General form of the GSF

#### 3-1-1 Gaussian mixture

There are some methods for describing a multimodal distribution. One is to describe it with particles, which is the method the PF introduced in Section 2-3-2 used. This is also shown in Figure 1-1 as an example. In addition, a Gaussian mixture can also be applied to approximate such distribution.

A Gaussian mixture describes a distribution as a sum of unimodal Gaussian components with corresponding weights and can be written as

$$p(x) = \sum_{i=1}^{M_{GSF}} w^i \mathcal{N}(\hat{x}^i, P^i), \quad (3-1)$$

where  $\mathcal{N}(\hat{x}^i, P^i)$  represents the distribution of the  $i$ th Gaussian component,  $w^i$  is the weight of the  $i$ th Gaussian component, and  $M_{GSF}$  is the number of the Gaussian components.

The multimodal distribution shown in Figure 1-1 can be approximated with a Gaussian mixture. The analytical expression of this Gaussian mixture can be written as

$$\begin{aligned} p(x) &= \sum_{i=1}^3 w^i \mathcal{N}(\hat{x}^i, P^i) \\ &= w^1 \mathcal{N}(\hat{x}^1, P^1) + w^2 \mathcal{N}(\hat{x}^2, P^2) + w^3 \mathcal{N}(\hat{x}^3, P^3) \\ &= 0.2 \mathcal{N}(2, 0.2) + 0.3 \mathcal{N}(3, 0.3) + 0.5 \mathcal{N}(5, 0.5) \end{aligned} \quad (3-2)$$

and a visualization of this approximation can be seen in Figure 3-1 where the three weighted unimodal Gaussian components are marked with dashed lines.

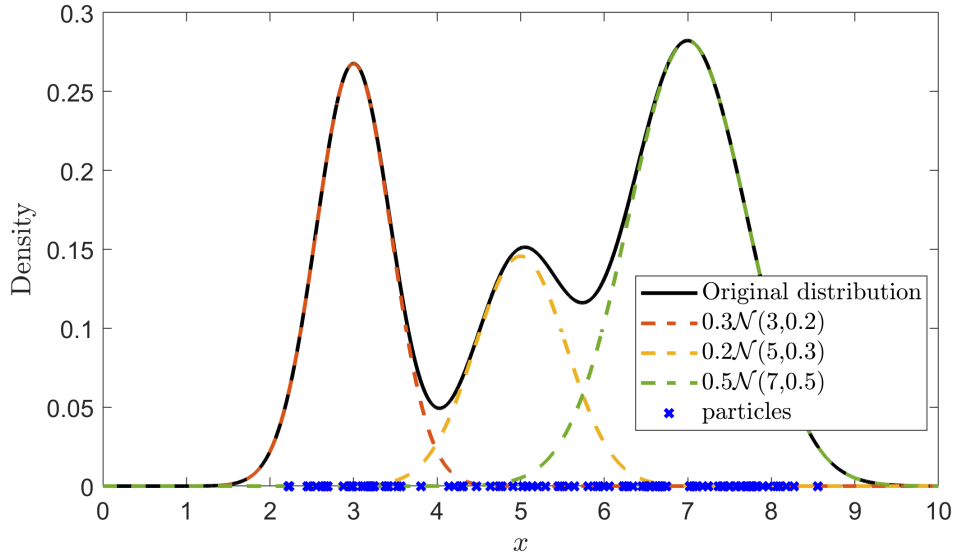


**Figure 3-1:** An 1-dimensional example of a Gaussian mixture approximating a multimodal distribution

### 3-1-2 Gaussian sum filter (GSF)

Gaussian sum filter (GSF) is a filter with distributions of the state approximated with Gaussian mixture (GM)s to preserve the multimodality. Therefore, it is considered as a potential solution to the research gap in this thesis project.

In a GSF, the posterior distribution  $p(x_t|y_{1:t})$  is approximated with a GM, which can be written as

$$p(x_t|y_{1:t}) = \sum_{i=1}^{M_{GSF}} w_t^i \mathcal{N}(\hat{x}_{t|t}^i, P_{t|t}^i), \quad (3-3)$$

where  $M_{GSF}$  is the number of the Gaussian components,  $w_t^i$  is the weight of the  $i$ th Gaussian component at time  $t$ ,  $\hat{x}_{t|t}^i$  is the mean of the  $i$ th Gaussian component, and

$P_{t|t}^i$  is the covariance matrix of the  $i$ th Gaussian components [1]. Furthermore, the distribution  $p(x_t|y_{1:t-1})$  is also approximated with a GM and can be written as

$$p(x_t|y_{1:t-1}) = \sum_{i=1}^{M_{GSF}} w_t^i \mathcal{N}(\hat{x}_{t|t-1}^i, P_{t|t-1}^i). \quad (3-4)$$

Similar to an EKF and a PF, a GSF has a time update and measurement update at each time iteration.

- **Time update**

In a time update of a GSF, the means and covariance matrices of each Gaussian component of the distribution  $p(x_t|y_{1:t-1})$  are updated with the same method as the time update in a EKF. In other words, the means  $\hat{x}_{t|t-1}^i$  and covariance matrices  $P_{t|t-1}^i$  of the GM-approximated distribution  $p(x_t|y_{1:t-1}) = \sum_{i=1}^{M_{GSF}} w_t^i \mathcal{N}(\hat{x}_{t|t-1}^i, P_{t|t-1}^i)$  are updated with

$$\hat{x}_{t|t-1}^i = f(\hat{x}_{t-1|t-1}^i), \quad (3-5a)$$

$$P_{t|t-1}^i = F_{t-1}^i P_{t-1|t-1}^i (F_{t-1}^i)^\top + Q, \quad (3-5b)$$

where  $F_{t-1}^i$  is the Jacobian of the time model at the point  $x_t = \hat{x}_{t-1|t-1}^i$ , which can be written mathematically as  $F_{t-1}^i = \left. \frac{df(x_t)}{dx_t} \right|_{x_t=\hat{x}_{t-1|t-1}^i} [1]$ .

- **Measurement update**

In the measurement update of a GSF, the means and the covariance matrices of each Gaussian component of the posterior distribution approximation  $p(x_t|y_{1:t}) = \sum_{i=1}^{M_{GSF}} w_t^i \mathcal{N}(\hat{x}_{t|t}^i, P_{t|t}^i)$  are updated using the same method as in an EKF. The analytical expression of the update of the posterior distribution can be written as

$$\hat{x}_{t|t}^i = \hat{x}_{t|t-1}^i + K_t^i (y_t - h(\hat{x}_{t|t-1}^i)), \quad (3-6a)$$

$$P_{t|t}^i = P_{t|t-1}^i - K_t^i S_t^i (K_t^i)^\top, \quad (3-6b)$$

where  $H_t^i = \left. \frac{dh(x_t)}{dx_t} \right|_{x_t=\hat{x}_{t|t-1}^i}$  is a Jacobian of the measurement model,  $S_t^i = H_t^i P_{t|t-1}^i (H_t^i)^\top + R$ , and  $K_t^i = P_{t|t-1}^i (H_t^i)^\top (S_t^i)^{-1} [1]$ .

- **Weight update** After the time and measurement updates that are similar to the EKF, there is an additional weight update for refreshing the weights  $w_t^i$ . The weights are updated with a similar approach as the one in a PF with the prior distribution as the proposal distribution [1].

The analytical expression of a GSF is also shown in Algorithm 1.

**Algorithm 1:** Gaussian sum filter (GSF)**Input:** Measurements  $\{y_t\}_{t=1}^N$ .**Output:** Estimated states  $\{\hat{x}_{t|t}\}_{t=1}^N$ .**Initialization:** Weights  $w_1^i = \frac{1}{M_{GSF}}$  for all  $i \in \{1, \dots, M_{GSF}\}$ , means of Gaussian components  $\{\hat{x}_{1|1}^i\}_{i=1}^{M_{GSF}}$ , and covariance matrices of Gaussian components  $\{P_{1|1}^i\}_{i=1}^{M_{GSF}}$ .1 **for**  $t = 2, \dots, N$  **do**2     **for**  $i = 1 : M_{GSF}$  **do**3         Time update

$$\hat{x}_{t|t-1}^i = f(\hat{x}_{t-1|t-1}^i), \quad (3-7a)$$

$$P_{t|t-1}^i = F_{t-1}^i P_{t-1|t-1}^i (F_{t-1}^i)^\top + Q, \quad (3-7b)$$

$$F_{t-1}^i = \left. \frac{df(x_t)}{dx_t} \right|_{x_t = \hat{x}_{t-1|t-1}^i}. \quad (3-7c)$$

(3-7d)

4         Measurement update

$$\hat{x}_{t|t}^i = \hat{x}_{t|t-1}^i + K_t^i (y_t - h(\hat{x}_{t|t-1}^i)), \quad (3-8a)$$

$$P_{t|t}^i = P_{t|t-1}^i - K_t^i S_t^i (K_t^i)^\top, \quad (3-8b)$$

$$H_t^i = \left. \frac{dh(x_t)}{dx_t} \right|_{x_t = \hat{x}_{t|t-1}^i}, \quad (3-8c)$$

$$S_t^i = H_t^i P_{t|t-1}^i (H_t^i)^\top + R, \quad (3-8d)$$

$$K_t^i = P_{t|t-1}^i (H_t^i)^\top (S_t^i)^{-1}. \quad (3-8e)$$

Weight update

$$w_t^i = w_{t-1}^i \mathcal{N}(y_t; h(\hat{x}_{t|t}^i), S_t^i). \quad (3-9a)$$

5     **end**6     Weight normalization

$$w_t^i = \frac{w_t^i}{\sum_{j=1}^{M_{GSF}} w_t^j}, \quad \forall i = 1, \dots, M_{GSF}, \quad (3-10)$$

7     Estimation

$$\hat{x}_{t|t} = \sum_{i=1}^{M_{GSF}} w_t^i \hat{x}_{t|t}^i \quad (3-11)$$

8 **end**

### 3-2 The GSF for magnetic field localization

Since the GSF is based on a EKF core, the GSF applied to the magnetic field localization will also be based on the EKF introduced in Section 2-3-1. As a result, besides the time and measurement updates introduced previously, there is also an additional correction of the linearization point made after the time and measurement updates. Furthermore, the weight of each Gaussian component is updated after this correction.

The EKF core run for  $M_{GSF}$  times in each time iteration is (the notation  $i \in \{1, 2, \dots, M_{GSF}\}$  on the up-right corner of the symbols represents the index of the Gaussian component):

- **Time update**

As the GSF utilizes the EKF as its core, the time update for each Gaussian component will be the same as seen in Eq. (2-33). Therefore, the time update for a Gaussian component can be written as

$$\hat{p}_{t|t-1}^{w,i} = \hat{p}_{t-1|t-1}^{w,i} + \Delta p_t^w, \quad (3-12a)$$

$$\hat{q}_{t|t-1}^{wb,i} = \hat{q}_{t-1|t-1}^{wb,i} \odot \exp_{\mathbf{q}}(\Delta q_t^b), \quad (3-12b)$$

$$P_{t|t-1}^i = P_{t-1|t-1}^i + Q_{\zeta}. \quad (3-12c)$$

- **Measurement update**

Similar to the time update, the measurement update of a Gaussian component of the GSF is also the same as the measurement update shown in Eq. (2-35). Thus, the analytical expression of the measurement update of a Gaussian component is

$$\hat{\zeta}_{t|t}^i = K_t(\hat{R}_{t|t-1}^{wb,i} y_t^b - \nabla \Phi(\hat{p}_{t|t-1}^{w,i}) \hat{m}), \quad (3-13a)$$

$$P_{t|t}^i = P_{t|t-1}^i - K_t^i S_t^i (K_t^i)^\top, \quad (3-13b)$$

where  $S_t^i = H_t^i P_{t|t-1}^i (H_t^i)^\top + \sigma_m^2 \mathcal{I}_3$ , and  $K_t^i = P_{t|t-1}^i (H_t^i)^\top (S_t^i)^{-1}$ .

- **Linearized point correction**

As mentioned previously, the GSF for magnetic field localization also has a correction of the linearized point as what the EKF has after the time and measurement updates. This correction for a Gaussian component is then

$$\hat{p}_{t|t}^{w,i} = \hat{p}_{t|t-1}^{w,i} + \hat{\delta}_{t|t}^{w,i}, \quad (3-14a)$$

$$\hat{q}_{t|t}^{wb,i} = \exp_{\mathbf{q}}(\hat{\eta}_{t|t}^{wb,i}) \odot \hat{q}_{t|t-1}^{wb,i}, \quad (3-14b)$$

where  $\hat{\delta}_{t|t}^{w,i}$  and  $\hat{\eta}_{t|t}^{wb,i}$  are from  $\hat{\zeta}_{t|t}^i$  calculated in the measurement update.

- **Weight update**

Besides the time and measurement updates and the linearized point correction the EKF has, the GSF also has a weight update. As the weight update is using the same method as the PF, the update is based on Eq. (2-38) and can be written as

$$w_t^i = w_{t-1}^i \mathcal{N}(\hat{R}_{t|t}^{wb,i} y_t^b; \nabla \Phi(\hat{p}_{t|t}^{w,i}) \hat{m}, S_t^i), \quad (3-15)$$

where  $\hat{R}_{t|t}^{wb,i}$  is a rotation matrix converted from  $\hat{q}_{t|t}^{wb,i}$ .

After the updates of all Gaussian components are done for one timestep, the updated weights are then normalized. Furthermore, the position and orientation estimates are also calculated by summing up the weighted estimations from the Gaussian components.

The algorithm of the GSF applied to magnetic field localization is also written down in analytical form in Algorithm 2.

**Algorithm 2:** GSF for magnetic field localization

**Input:** Odometry measurements  $\{\Delta p_t^w, \Delta q_t^b\}_{t=1}^N$ , magnetic field measurements  $\{y_t^b\}_{t=1}^N$ , and a magnetic field weight vector  $m$ .

**Output:** Estimated positions  $\{\hat{p}_{t|t}^w\}_{t=1}^N$ , and estimated orientations  $\{\hat{q}_{t|t}^{wb}\}_{t=1}^N$ .

**Initialization:** Weights  $\{w_1^i = \frac{1}{M_{GSF}}\}_{i=1}^{M_{GSF}}$ , position means  $\{\hat{p}_{1|1}^{w,i}\}_{i=1}^{M_{GSF}}$ , orientation means  $\{\hat{q}_{1|1}^{wb,i}\}_{i=1}^{M_{GSF}}$ , and covariance matrices  $\{P_{1|1}^i\}_{i=1}^{M_{GSF}}$  of Gaussian components.

1 **for**  $t = 2, \dots, N$  **do**

2     **for**  $i = 1 : M_{GSF}$  **do**

3         Time update

$$\hat{p}_{t|t-1}^{w,i} = \hat{p}_{t-1|t-1}^{w,i} + \Delta p_t^w, \quad (3-16a)$$

$$\hat{q}_{t|t-1}^{wb,i} = \hat{q}_{t-1|t-1}^{wb,i} \odot \exp_q(\Delta q_t^b), \quad (3-16b)$$

$$P_{t|t-1}^i = P_{t-1|t-1}^i + Q_\zeta. \quad (3-16c)$$

4         Measurement update

$$\hat{\zeta}_{t|t}^i = K_t(\hat{R}_{t|t-1}^{wb,i} y_t^b - \nabla \Phi(\hat{p}_{t|t-1}^{w,i}) m), \quad (3-17a)$$

$$P_{t|t}^i = P_{t|t-1}^i - K_t^i S_t^i (K_t^i)^\top, \quad (3-17b)$$

$$S_t^i = H_t^i P_{t|t-1}^i (H_t^i)^\top + \sigma_m^2 \mathcal{I}_3, \quad (3-17c)$$

$$K_t^i = P_{t|t-1}^i (H_t^i)^\top (S_t^i)^{-1}. \quad (3-17d)$$

5         Linearized point correction

$$\hat{p}_{t|t}^{w,i} = \hat{p}_{t|t-1}^{w,i} + \hat{\delta}_{t|t}^{w,i}, \quad (3-18a)$$

$$\hat{q}_{t|t}^{wb,i} = \exp_q(\hat{\eta}_{t|t}^{wb,i}) \odot \hat{q}_{t|t-1}^{wb,i}. \quad (3-18b)$$

6         Weight update

$$w_t^i = w_{t-1}^i \mathcal{N}(\hat{R}_{t|t}^{wb,i} y_t^b; \nabla \Phi(\hat{p}_{t|t}^{w,i}), S_t^i). \quad (3-19)$$

7     **end**

8     Weight normalization

$$w_t^i = \frac{w_t^i}{\sum_{j=1}^{M_{GSF}} w_t^j}, \quad \forall i \in \{1, \dots, M_{GSF}\}, \quad (3-20)$$

9     Estimation

$$\hat{p}_{t|t} = \sum_{i=1}^{M_{GSF}} w_t^i \hat{p}_{t|t}^{w,i}, \quad (3-21a)$$

$$\hat{q}_{t|t} = \sum_{i=1}^{M_{GSF}} w_t^i \hat{q}_{t|t}^{wb,i}. \quad (3-21b)$$

10 **end**



# Simulation results of fully-simulated magnetic field localization with the Gaussian sum filter (GSF) applied as an estimator

To study if the GSF is an algorithm suitable for multimodal distribution and is more efficient compared with the Particle filter (PF) in magnetic field localization, the GSF was applied to the localization system with simulated magnetometer measurements and the results were compared to the ones of the Extended Kalman filter (EKF) and the PF. Since the uncertainty is taken into account, the simulations in this chapter were run as a Monte Carlo simulation with 100 experiments.

In this chapter, the settings kept constant through all simulations, including the simulated trajectory and the algorithms, will be first introduced. Then, the settings changed in different simulations and the simulation results will be discussed in Section 4-2. At the end, a brief conclusion based on the results of the simulations will be given.

## 4-1 Settings kept constant through all simulations

### 4-1-1 Trajectory

The trajectory of the simulation is shown in Figure 4-1. The magnetometer was simulated to move in this trajectory and the magnetic field in this range was known.

The initial position of the simulated trajectory was at  $p_1^w = [-0.95 \quad -1 \quad 0]^T$ . The trajectory is a counterclockwise square with each side 2 meters long. For each simulation, the target moved in this square counterclockwise 4 times and ended up at

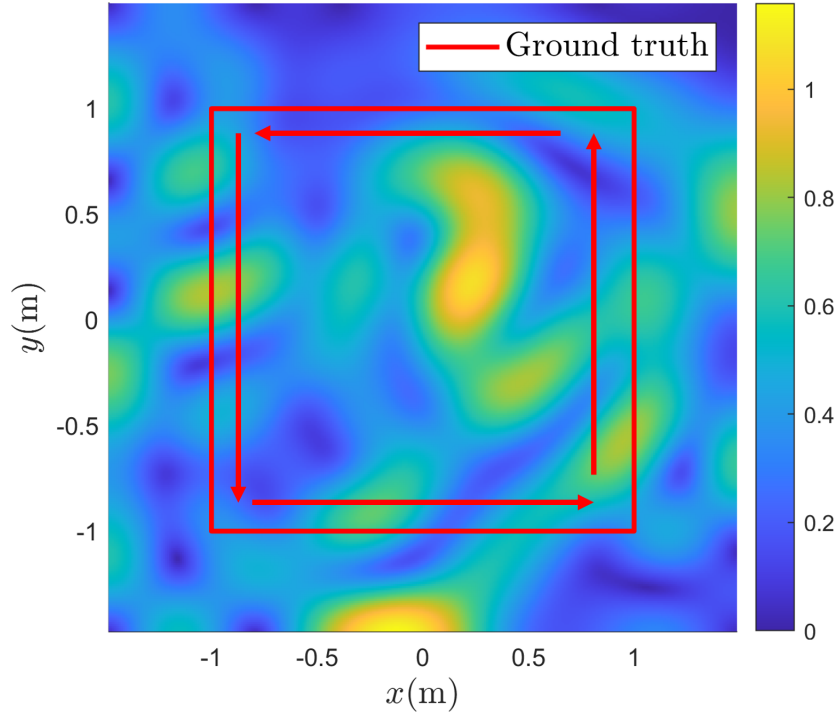


**Figure 4-1:** The 2-dimensional plot of the ground truth trajectory of the simulations of magnetic field localization (red arrow representing the direction of the trajectory)

$p_N^w = [-1 \quad -1 \quad 0]^T$ , where  $N$  is the end time of the trajectory and was set as 640 in this chapter. In the whole trajectory, the position on  $Z$  axis  $p_{z,t}^w$  was kept to 0.

The orientation  $q_t^{wb}$  was fixed to  $[1 \quad 0 \quad 0 \quad 0]^T$  for the entire trajectory.

#### 4-1-2 Models

The models applied in this chapter is from Eq. (2-8), (2-9), and (2-24). The magnetic field map, inputs, and noise settings implemented in the models will be introduced below.

##### Magnetic field map

The magnetic field map in this simulation is a fully simulated map with 50 basis functions. Therefore, the recursive process of estimating the weight vector  $m$  shown in Eq. (2-31) was not performed in the simulations in this chapter. As a result, the distribution of the weight vector  $m$  was the same as the initial guess given in Eq. (2-29).

The magnetometer measurements were then simulated with the simulated positions and orientations introduced in Section 4-1-1 as the inputs of the measurement model shown in Eq. (2-24). An example of how the norm of the simulated magnetometer measurements of the whole localizing area is shown in Figure 4-1.

### Inputs and noises

The inputs were the transition data obtained from the known ground truth positions and orientations with additional noises. The calculation can be written as

$$\Delta p_t^w = p_{t+1}^w - p_t^w + e_{dp,t}^w, \quad (4-1a)$$

$$\Delta q_t^b = f_{qa}(q_{t+1}^{wb} \odot q_t^c) + e_{dq,t}^b, \quad (4-1b)$$

where  $e_{dp,t}^w \sim \mathcal{N}(0, R_{dp})$ ,  $e_{dq,t}^w \sim \mathcal{N}(0, R_{dq})$ ,  $f_{qa}$  is a function that converts unit quaternions to axis-angle representation, and  $q_t^c$  is the quaternion conjugation of  $q_t$ . As a baseline for judging the estimation accuracy, the transition positions were used for odometry and the results were compared to the other algorithms in the simulation.

The covariance of the simulated transition position  $R_{dp}$  was set to  $10^{-4}\mathcal{I}_3$  and the covariance of the simulated transition orientation  $R_{dq}$  was set to  $10^{-5}\mathcal{I}_3$ .

### 4-1-3 Algorithms

In these simulations of the magnetic field localization, there are three algorithms applied for the estimation of the position and the orientation. The first two are the EKF and the PF, which are the ones that have been applied to the magnetic field localization in previous studies [38, 30, 18]. The last algorithm is the newly introduced GSF. In this section, the settings of these algorithms for magnetic field localization that were set constant through the simulations will be introduced.

Note that the code for the EKF and the PF are from [38].

- **Extended Kalman filter (EKF)**

In the simulations in this chapter, the initial mean and covariance of the EKF were set according to the assigned initial error  $\epsilon_0$ . The initial error was designed to represent the squared distance between the ground truth and the initial estimated position in  $X$  or  $Y$  axis. Therefore, the relationship between the initial error  $\epsilon_0$  and the initial estimated position can be written as

$$\hat{p}_{x,1|1}^w = p_{x,1}^w + \sqrt{\epsilon_0}, \quad (4-2a)$$

$$\hat{p}_{y,1|1}^w = p_{y,1}^w + \sqrt{\epsilon_0}, \quad (4-2b)$$

$$\hat{p}_{z,1|1}^w = p_{z,1}^w, \quad (4-2c)$$

where  $p_1^w = [p_{x,1}^w, p_{y,1}^w, p_{z,1}^w]^T$  is the initial ground truth of the 3-dimensional position. The initial covariance matrix of the EKF was also correlated with the initial error  $\epsilon_0$  as

$$P_{1|1} = \begin{bmatrix} 1.5\epsilon_0 & 0 & 0 & 0 & 0 & 0 \\ 0 & 1.5\epsilon_0 & 0 & 0 & 0 & 0 \\ 0 & 0 & 0.001 & 0 & 0 & 0 \\ 0 & 0 & 0 & 0.001 & 0 & 0 \\ 0 & 0 & 0 & 0 & 0.001 & 0 \\ 0 & 0 & 0 & 0 & 0 & 0.001 \end{bmatrix}, \quad (4-3)$$

where the value “1.5” multiplied before the initial error was set to ensure the ground truth is within the 68 % confidence interval. The value of the initial error would vary through different simulations, so it will be introduced when describing the settings changed in different simulations in Section 4-2. Note that the initialization of the estimated orientation  $\hat{q}_1^{\text{wb}}$  was fixed to  $[1, 0, 0, 0]^T$  in all simulations.

The process noise  $R_p$  and  $R_q$  of the dynamic models in Eq. (2-33e) were set to the same value as the measurement covariances of the transition data  $R_{dp}$  and  $R_{dq}$  in this system.

- **Particle filter**

The PF applied here to the simulations of magnetic field localization is the same as the one introduced in [30] and the code is based on the one used in [38].

The number of the particles  $M_{PF}$  was set to 100, 200, and 500 in all simulations. The purpose of setting three different values of  $M_{PF}$  is to show the different performance of the PF under different numbers of the particles  $M_{PF}$ . This is mainly used to imply the difficulty of the choice of  $M_{PF}$  when efficiency and accuracy are both concerned in localization.

The initial particles were sampled from the same initial distribution of the EKF. Therefore, the initial particles will vary through simulations with the initial distribution of the EKF.

- **Gaussian sum filter**

The initial weights  $w_1^i$  of the Gaussian components were set equally.

The Gaussian components were initially assigned in a diamond range to approximate the ellipsoid that was formed by the mean and the covariance of the EKF. To approximate the ellipsoid, the size of the diamond shape was based on the covariance values of the EKF. Therefore, the means of the Gaussian components were placed in the range

$$\begin{bmatrix} \hat{p}_{x,1|1}^{\text{w},i} \\ \hat{p}_{y,1|1}^{\text{w},i} \end{bmatrix} = R \begin{bmatrix} \delta \hat{p}_{x,1|1}^{\text{w},i} \\ \delta \hat{p}_{y,1|1}^{\text{w},i} \end{bmatrix} + \begin{bmatrix} \hat{p}_{x,1|1}^{\text{w}} \\ \hat{p}_{y,1|1}^{\text{w}} \end{bmatrix}, \quad (4-4a)$$

where

$$\delta \hat{p}_{x,1|1}^{\text{w},i} \in [-\sqrt{P_{1|1,(x,x)}}, \sqrt{P_{1|1,(x,x)}}], \quad (4-4b)$$

$$\delta \hat{p}_{y,1|1}^{\text{w},i} \in [-\sqrt{P_{1|1,(y,y)}}, \sqrt{P_{1|1,(y,y)}}], \quad (4-4c)$$

$$R = \begin{bmatrix} \cos(0.25\pi) & -\sin(0.25\pi) \\ \sin(0.25\pi) & \cos(0.25\pi) \end{bmatrix}. \quad (4-4d)$$

The resulting GSF is shown in Figure 4-2 This design is to avoid the means of the GSF set too close to the ground truth that could lead to doubts about the performance of the GSF. The detailed process of how this layout is developed is explained in Appendix F.

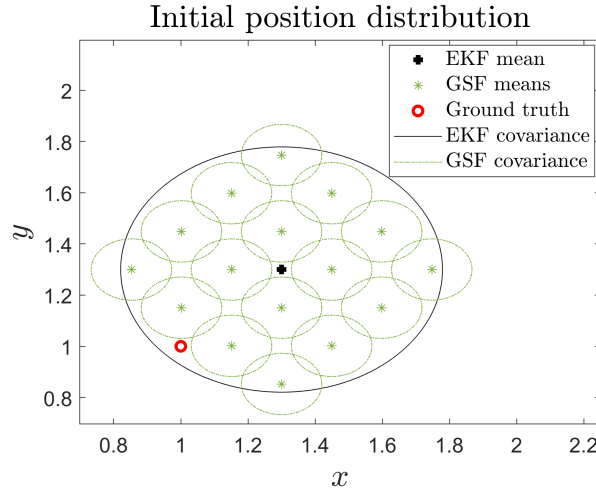


**Figure 4-2:** An example of how the GSF is designed to approximate the EKF

The ranges on the  $Z$  axis and the orientation were set to a single value because the measurements of the  $Z$  axis and the orientation were assumed to be precise. Furthermore, this setting also refers to the setting of the EKF for the simulation of magnetic field localization. The value for the initial estimation of the position in  $Z$  axis was thus set to  $\hat{p}_{z,1|1}^{w,i} = \hat{p}_{z,1|1}^w = p_{z,1}^w = 0$ . The orientation was also set to be equaled with the ground truth  $\hat{q}_{1|1}^{w,i} = \hat{q}_{1|1}^w = [1, 0, 0, 0]^T$ .

The initial covariance matrixes were set to the same diagonal matrices for all Gaussian components. The first diagonal value, which is the variance in the  $X$  axis, was calculated as

$$P_{1|1,(x,x)}^i = \left( \frac{\sqrt{P_{1|1,(x,x)}}}{M_{GSF,x}} \right)^2, \quad (4-5a)$$

where  $P_{1|1,(x,x)}$  is the first diagonal value of the initial covariance matrix of the EKF  $P_{1|1}$  and  $M_{GSF,x}$  is the number of the Gaussian components of the GSF on the  $X$  axis. This formula is set to make the range of the means of the Gaussian components approximating the 68% confidence covariance ellipsoid of the EKF with the covariances of the Gaussian components covering the range but not overlapping too much. The second diagonal value for the  $Y$  axis variance is calculated using

$$P_{1|1,(y,y)}^i = \left( \frac{\sqrt{P_{1|1,(y,y)}}}{M_{GSF,y}} \right)^2, \quad (4-5b)$$

where  $P_{1|1,(y,y)}$  is the second diagonal value of the initial covariance matrix of the EKF  $P_{1|1}$  and  $M_{GSF,y}$  is the number of the Gaussian components of the GSF on the  $Y$  axis. Other values on the diagonal are set to 0.001 because the corresponding measurements are assumed to be quite accurate.

The number of the Gaussian components  $M_{GSF}$  was set as a squared value of an integer. This is because the Gaussian components were designed to approximate the covariance ellipsoid of the EKF with a 2-dimensional diamond in the  $X - Y$

plane. Therefore, the relationship for the number of the Gaussian components  $M_{GSF}$  with the number of the Gaussian component of each state element will be

$$\begin{aligned} M_{GSF} &= M_{GSF,x} \cdot M_{GSF,y} \cdot M_{GSF,z} \cdot M_{GSF,q1} \cdot M_{GSF,q2} \cdot M_{GSF,q3} \cdot M_{GSF,q4} \\ &= \sqrt{M_{GSF}} \cdot \sqrt{M_{GSF}} \cdot 1 \cdot 1 \cdot 1 \cdot 1 \cdot 1, \end{aligned} \quad (4-6)$$

where  $M_{GSF,z}$  is the number of the Gaussian components on the  $Z$  axis and the  $M_{GSF,q1}$ ,  $M_{GSF,q2}$ ,  $M_{GSF,q3}$  and  $M_{GSF,q4}$  are the number of the Gaussian components of each element of the unit quaternion for the representation of the orientation.

The actual value of the number of the Gaussian components  $M_{GSF}$  would be different for different simulations, so it will be introduced later.

The simulation settings for the three algorithms are also listed in Table 4-1. Note that the values might be varied depending on the settings of each simulation.

## 4-2 Simulation results

To study the performance of the GSF applied to magnetic field localization, several simulations were run. In each simulation, three algorithms, the EKF, the PF, and the GSF, were employed for the estimation of the position and the orientation. The simulation results were evaluated using the root mean squared error (RMSE) of the whole trajectory.

The simulations that will be discussed in the following subsections are

- **Varied initial error  $\epsilon_0$ :**  
The simulation with varied initial uncertainty is also shown in the previous study of magnetic field localization [38]. As the initial uncertainty grows to the distance that includes the non-unique section of the magnetic field map, the multimodality will exist, which is also explained in Section 1-2. Therefore, when the initial error is large enough, the EKF is expected to be inaccurate. In this simulation, the uncertainty was introduced by an initial error  $\epsilon_0$  value that changed the value of the initial distribution of the EKF. This varied value in the simulation affected all algorithms as they all depended on the same initial distribution.
- **Varied numbers of Gaussian components of the Gaussian sum filter  $M_{GSF}$ :**  
There is a lack of a rule of thumb for the setting of the number of the Gaussian components of the GSF  $M_{GSF}$ . Therefore, in this simulation, different values for the number of the Gaussian components of the GSF  $M_{GSF}$  were tried in iterations of the simulation to see what value is the most suitable value for the simulation of the magnetic field localization. Furthermore, the time durations of the algorithms were recorded in this simulation to check if the GSF is more efficient than the PF while having equivalent or better accuracy. Note that the settings for the EKF

Algorithm	Variables	Values
EKF	Initial estimated position $\hat{p}_{1 1}^w$	$\begin{aligned} \hat{p}_{x,1 1}^w &= p_{x,1}^w + \sqrt{\epsilon_0}, \\ \hat{p}_{y,1 1}^w &= p_{y,1}^w + \sqrt{\epsilon_0}, \\ \hat{p}_{z,1 1}^w &= p_{z,1}^w, \\ j &\in \{1, \dots, 10\} \end{aligned}$
	Initial estimated covariance $P_{1 1}$	$\begin{bmatrix} P_{1 1,(x,x)} & 0 & 0 & 0 & 0 & 0 \\ 0 & P_{1 1,(y,y)} & 0 & 0 & 0 & 0 \\ 0 & 0 & 0.001 & 0 & 0 & 0 \\ 0 & 0 & 0 & 0.001 & 0 & 0 \\ 0 & 0 & 0 & 0 & 0.001 & 0 \\ 0 & 0 & 0 & 0 & 0 & 0.001 \end{bmatrix},$ <p>where</p> $\begin{aligned} P_{1 1,(x,x)} &= 1.5\epsilon_0, \\ P_{1 1,(y,y)} &= 1.5\epsilon_0, \\ j &\in \{1, \dots, 10\} \end{aligned}$
PF	Initial estimated position $\hat{p}_1^w$	$\begin{aligned} \hat{p}_{x,1}^w &= \hat{p}_{x,1 1}^w, \\ \hat{p}_{y,1}^w &= \hat{p}_{y,1 1}^w, \\ \hat{p}_{z,1}^w &= \hat{p}_{z,1 1}^w \end{aligned}$
	Initial estimated covariance $P_1$	$P_1 = P_{1 1}$
GSF	Number of Gaussian components $M_{GSF}$	$\sqrt{M_{GSF}} \cdot \sqrt{M_{GSF}} \cdot 1$
	Range of the initial mean $\hat{p}_{1 1}^{w,i}$	$\begin{aligned} \begin{bmatrix} \hat{p}_{x,1 1}^{w,i} \\ \hat{p}_{y,1 1}^{w,i} \end{bmatrix} &= R \begin{bmatrix} \delta \hat{p}_{x,1 1}^{w,i} \\ \delta \hat{p}_{y,1 1}^{w,i} \end{bmatrix} + \begin{bmatrix} \hat{p}_{x,1 1}^w \\ \hat{p}_{y,1 1}^w \end{bmatrix}, \\ \hat{p}_{z,1 1}^{w,i} &= \hat{p}_{z,1 1}^w, \\ \delta \hat{p}_{x,1 1}^{w,i} &\in [-\sqrt{P_{1 1,(x,x)}}, \sqrt{P_{1 1,(x,x)}}], \\ \delta \hat{p}_{y,1 1}^{w,i} &\in [-\sqrt{P_{1 1,(y,y)}}, \sqrt{P_{1 1,(y,y)}}], \\ R &= \begin{bmatrix} \cos(0.25\pi) & -\sin(0.25\pi) \\ \sin(0.25\pi) & \cos(0.25\pi) \end{bmatrix} \end{aligned}$
	Initial covariance of each Gaussian component $P_{1 1}^i$	$\begin{bmatrix} P_{1 1,(x,x)}^i & 0 & 0 & 0 & 0 & 0 \\ 0 & P_{1 1,(y,y)}^i & 0 & 0 & 0 & 0 \\ 0 & 0 & 0.001 & 0 & 0 & 0 \\ 0 & 0 & 0 & 0.001 & 0 & 0 \\ 0 & 0 & 0 & 0 & 0.001 & 0 \\ 0 & 0 & 0 & 0 & 0 & 0.001 \end{bmatrix},$ <p>where</p> $\begin{aligned} P_{1 1,(x,x)}^i &= \left(\frac{\sqrt{P_{1 1,(x,x)}}}{M_{GSF,x}}\right)^2, \\ P_{1 1,(y,y)}^i &= \left(\frac{\sqrt{P_{1 1,(y,y)}}}{M_{GSF,y}}\right)^2 \end{aligned}$

**Table 4-1:** Initialization of the algorithms for the simulations of the magnetic field localization

and the PF in this simulation were fixed through iterations as the main interest is in the GSF.

- **Varied initial covariance matrices of the Gaussian sum filter  $P_{1|1}^i$ :**  
As there is also no rule of thumb for the covariance values of the initial covariances of the GSF, a simulation with varied initial covariance values of the Gaussian components of the GSF was run as an experiment.

#### 4-2-1 Varied initial error $\epsilon_0$

As mentioned in Section 1-2, due to the non-uniqueness of the function in the measurement model of magnetic field localization, multimodal distributions might exist when the initial error  $\epsilon_0$  is large enough. Hence, the simulation in this section was designed to trigger the multimodality of magnetic field localization by varying the initial error  $\epsilon_0$ .

In this simulation, the initial error  $\epsilon_0$  was designed to vary from 0.05 to 0.25, with 10 values equally sampled from this interval. The initialization of all three algorithms was influenced by this initial error. Therefore, in the results of this simulation, the performances of each algorithm when facing different initial uncertainties can be observed.

Following are the introduction of the initialization settings for the algorithms and the discussion of the simulation results:

- **Initialization of the algorithms:**  
To equally sample 10 initial error values from the interval  $[0.05, 0.25]$ , the following equation was designed for the value of each iteration  $j$

$$\epsilon_0 = 0.05 + \frac{j-1}{9} \cdot 0.2, \quad \forall j \in \{1, \dots, 10\}. \quad (4-7)$$

- **EKF:**  
The initial error was introduced to the initial estimated position  $\hat{p}_{1|1}^w$  using Eq. (4-2) and the initial covariance using Eq. (4-3).
- **PF:**  
The distribution that the initial particles were sampled from was the same distribution as the initial distribution of the EKF.
- **GSF:**  
The number of the Gaussian components of the GSF was set to be fixed to 16 and was set in the way as in Section 4-1-3.  
The range of the initial means of the Gaussian components of the GSF was set in the same way as Eq. (4-4) with the initial estimated position  $\hat{p}_{1|1}^{w,i}$  and the initial estimated covariance  $P_{1|1}^i$  introduced in Eq. (4-5).

The initialization of the EKF and the GSF is plotted in Figure 4-3. As the initial error increases, the 68% confidence ellipsoid of the initial estimated EKF distribution grows larger and indicates larger initial uncertainty. Since the initial

means and covariances of the GSF depend on the initial distribution of the EKF, the means of the GSF  $\hat{p}_1^{w,i}$  are more separated and the size of the initial covariances of the GSF  $P_{1|1}^i$  is larger.

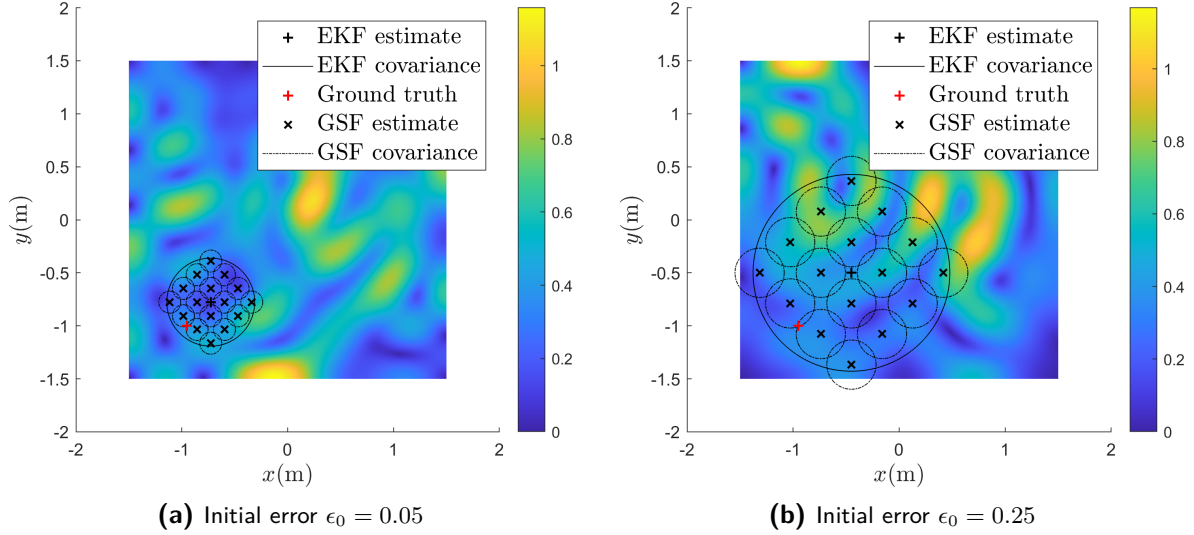


**Figure 4-3:** The visualization of the algorithm initializations for the magnetic field localization with varied initial error  $\epsilon_0$

- **Simulation results:**

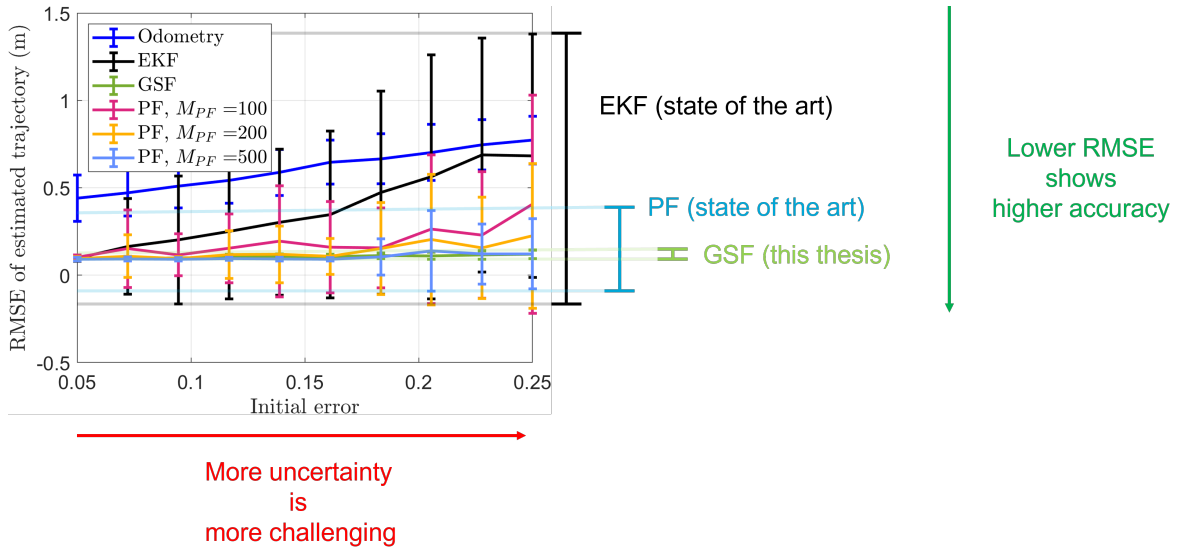
The simulation in this section was run as a Monte Carlo simulation with 100 iterations for each  $j$  value shown in Eq. (4-7). The simulation results are shown in Figure 4-4.

The EKF shows the worst capability of dealing with large initial errors as expected. As discussed previously in Section 1-2, a large initial error might lead to multimodal distributions, which is against the assumption the EKF is based on.

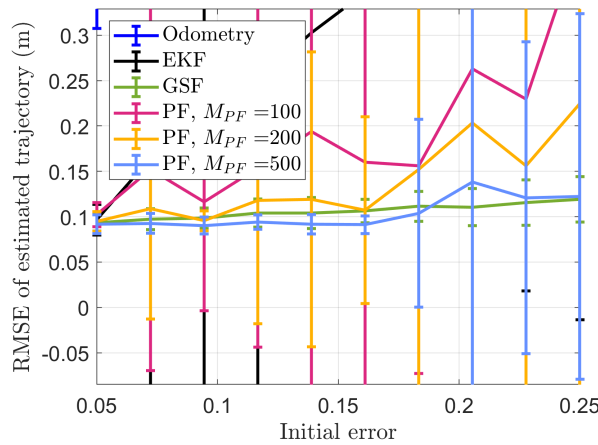
The PFs also show a growing trend of error. However, this error grows slower when the number of particles  $M_{PF}$  is larger.

The GSF also shows a growing trend in the RMSE as shown in the enlarged Figure 4-4b. However, compared with the other algorithms, the GSF is relatively more robust to the initial error. This is obvious when compared with the other algorithms using the unscaled figure in Figure 4-4a.

As the initial error grows, the distribution of the state will become multimodal. This is also seen from the estimations of the algorithms when the time step  $t$  is 2 in Figure 4-5. When the initial error is small in Figure 4-5a, the particles of the PF are quite close together and are near the estimation of the EKF. However, when the initial error is large, as shown in Figure 4-5c, the particles of the PF are scattered in the space and gathered into groups. As the particles can represent the distribution of the state, this phenomenon indicates that the distribution is now a multimodal distribution. This is a clear example that when the initial error is large, there exist multimodal distributions, which is a problematic condition for



(a) All data included



(b) Enlarged plot

**Figure 4-4:** The RMSE of the estimated trajectories of the algorithms under different values of initial errors  $\epsilon_0$  for the magnetic field localization

the EKF. As a result, when the GSF is having good performance with a large initial error value, it implies that the GSF is more suitable for multimodality than the EKF.

From this simulation, it is also found that the multimodality starts happening when the initial error reaches 0.1 (as shown in Figure 4-4 and 4-5b). As the main goal of this thesis project is to find an algorithm that is suitable for multimodality, the simulations were preferred to be set under the condition that there are multimodal distributions. As a result, the initial error in the other simulations was set to 0.1.

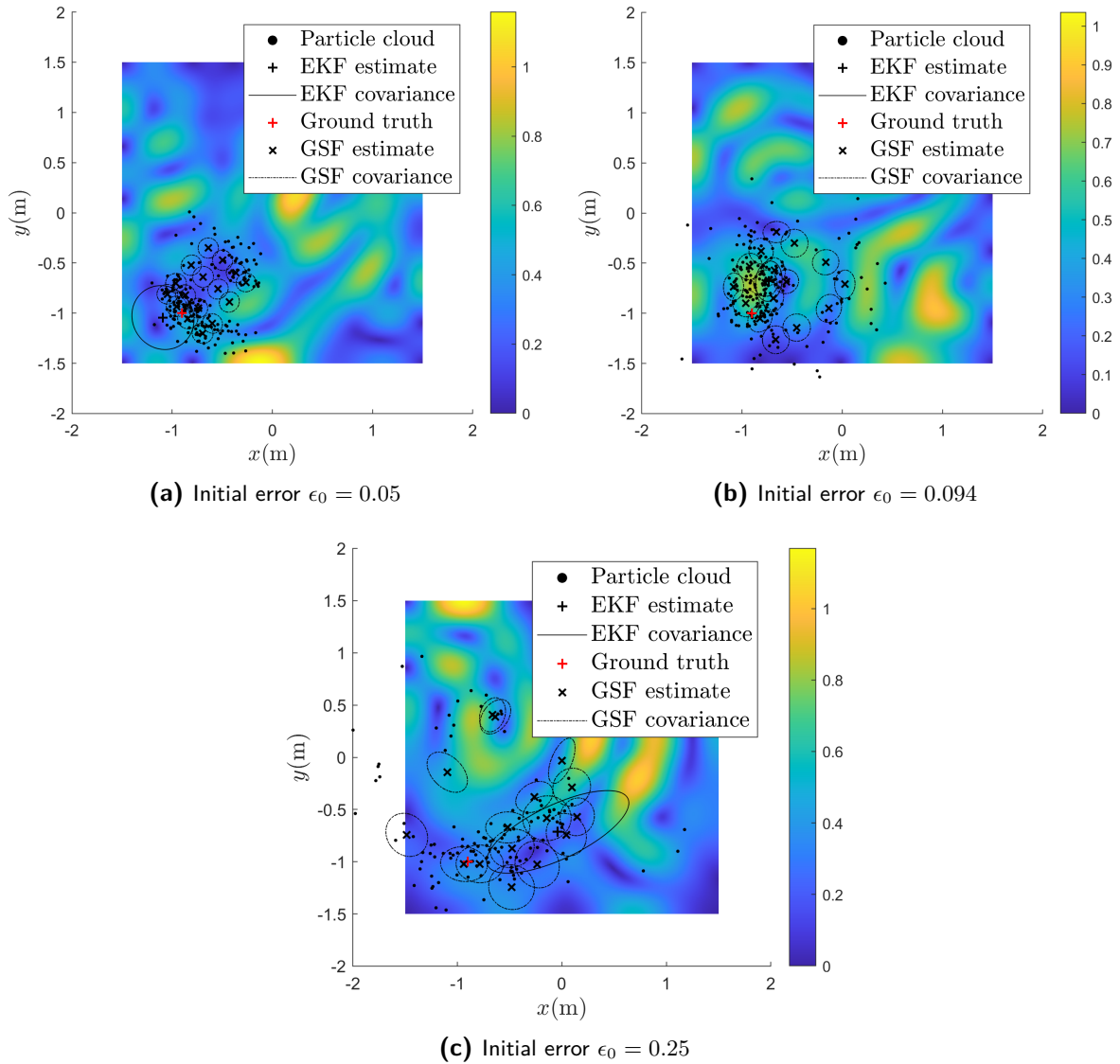


**Figure 4-5:** The estimations of the algorithms at  $t = 2$  with varied initial error  $\epsilon_0$

#### 4-2-2 Varied numbers of Gaussian components of the GSF $M_{GSF}$

The number of the Gaussian components of the GSF  $M_{GSF}$  might influence the estimation results of the GSF. It was expected that with more Gaussian components, the GSF would be more accurate, but would also be more computationally costly as shown in the illustration in Figure 4-6. However, there's no clear rule for the best value of  $M_{GSF}$  that can make the GSF accurate enough but also not too time-consuming. Hence, a simulation with varied values of  $M_{GSF}$  was run and the results will be shown in this section.

Moreover, by comparing the time duration of each algorithm recorded through the simulation, the GSF can be checked if it is more efficient than the PF while having comparable accuracy. This check is to make sure that the GSF is a solution to the

current research gap in magnetic field localization that there is a lack of an algorithm that is more efficient compared with the PF and more accurate than the EKF when multimodality exists.

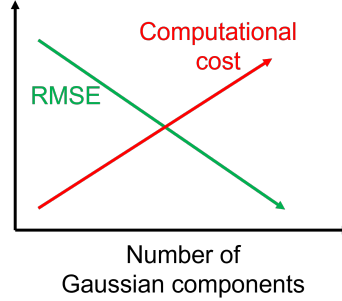


**Figure 4-6:** The possible trade-off when increasing the number of Gaussian components of the GSF

The bullet points below are the introduction of the algorithm initialization and the simulation results:

- **Initialization of the algorithms:** The initial error  $\epsilon_0$  in this simulation was set to 0.1 and was not varied.

- **GSF:**

The number of the Gaussian components of the GSF  $M_{GSF}$  was varied through the simulation. As introduced in Section 4-1-3,  $M_{GSF}$  was designed to have the initial means of the Gaussian components to form a diamond shape in the 2-dimensional  $X - Y$  plane to approximate the initial covariance ellipsoid of the EKF, so  $M_{GSF}$  was a value of squared integer. Following this design,  $M_{GSF}$  was set to be

$$M_{GSF} = M_{GSF,x} \cdot M_{GSF,y} \cdot M_{GSF,z} = j \cdot j \cdot 1 = j^2, \quad (4-8)$$

where  $j$  is an integer from the integer set  $\{2, \dots, 8\}$ . This setting is visualized in Figure 4-7. When  $M_{GSF} = 2 \cdot 2 = 4$ , the initial Gaussian components of the GSF were set relatively loosely placed in the space as shown in Figure 4-7a. When  $M_{GSF}$  is increased to  $8 \cdot 8 = 64$ , the Gaussian components, shown in Figure 4-7b, were set densely in the diamond range since the range size remained the same but  $M_{GSF}$  was increased.

The range of the initial means of the GSF was set using Eq. (4-4).

The initial covariance matrices of all Gaussian components were set as calculated following Eq. (4-5).

- **EKF and PF:**

Since the main purpose of the simulation in this section is to discuss the effect of the number of Gaussian components of the GSF on the performance of the GSF, the initialization setting for the EKF and the PF remained the same as the initial error was kept the same value throughout the simulation. The

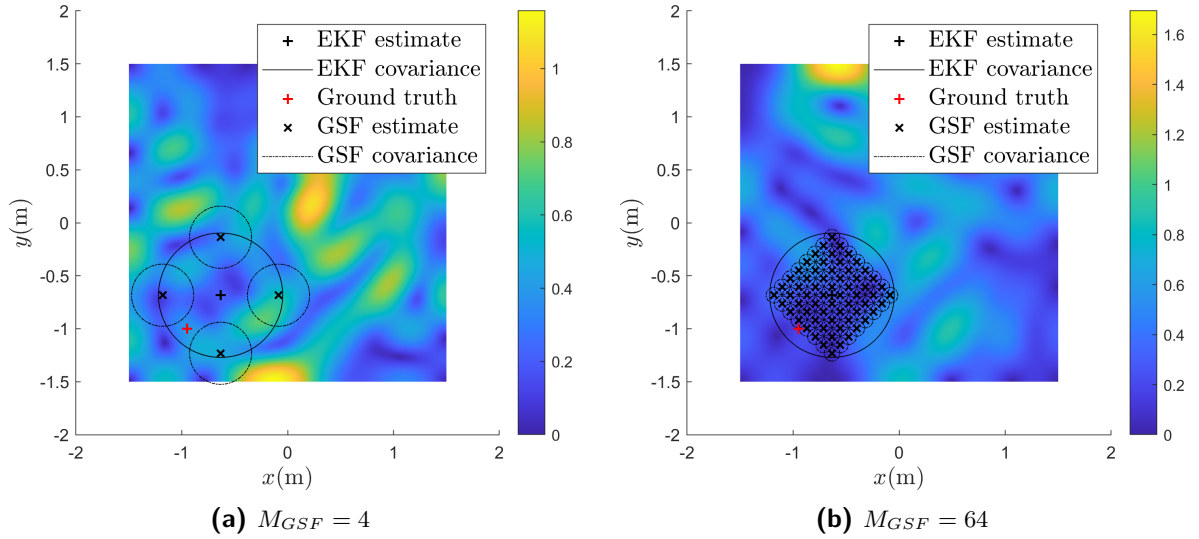


**Figure 4-7:** The visualization of the algorithm initializations for the magnetic field localization with varied numbers of Gaussian components of the GSF  $M_{GSF}$

initial estimated distribution of the EKF was fixed through the simulation and set with Eq. (4-2) and (4-3). The initial particles of the PF were sampled from the initial distribution of the EKF.

- **Simulation results:**

The simulation here was also run as a Monte Carlo simulation with 100 iterations for each value of the number of the Gaussian components of the GSF  $M_{GSF}$ . The RMSE of the simulation results is shown in Figure 4-8, and the mean of the time durations of each value of  $M_{GSF}$  are presented in Figure 4-9.

Since the EKF and the PF initialization settings were not changed through iterations, in Figure 4-8 and 4-9, the results of these algorithms are plotted with their means and the 95% confidence interval of all iterations.

The results of the EKF are as expected with large error since the initial error in this simulation was set in purpose to trigger the multimodality of the system. Moreover, the PF also has unsurprising results. The RMSE of the PF is lower as the number of the particles is larger.

The RMSE of the GSF does not vary a lot with the number of the Gaussian components. However, as seen in Figure 4-3a, the GSF is not approximating the EKF correctly as the covariances are not covering lots of the covariance ellipsoid of the EKF. Therefore, the number of the Gaussian components in the other simulations was not set to 4 despite it having the least computational cost. Moreover, when there are 9 Gaussian components, a mean of a Gaussian component might be too close to the ground truth since the initial estimation was designed to be placed in a diagonal direction from the ground truth. When the number of the Gaussian components is odd, several Gaussian components will be placed on the same diagonal line and thus will increase the chance the ground truth is overlapping with a Gaussian component when initializing. This setting might lead to some doubt of

the true reason for the good performance of the GSF. Thus, 9 was also not chosen as the number of the Gaussian component of the settings of the other simulations. As a result, the number of the Gaussian component of the other simulations was set to 16.

Besides checking the RMSE of the GSF, its time duration through the simulation was also recorded and compared with the PF. By comparing the time duration, the GSF can be checked if it is more efficient compared with the PF. As shown in Figure 4-9, the time duration of GSF is almost always lower than the PF when the number of the particles  $M_{PF}$  is 100, which is the PF that is often more inaccurate than GSF. As a result, the value 16 set for  $M_{GSF}$  in other simulations is proved to be more efficient than the PF while having equivalent or better accuracy.

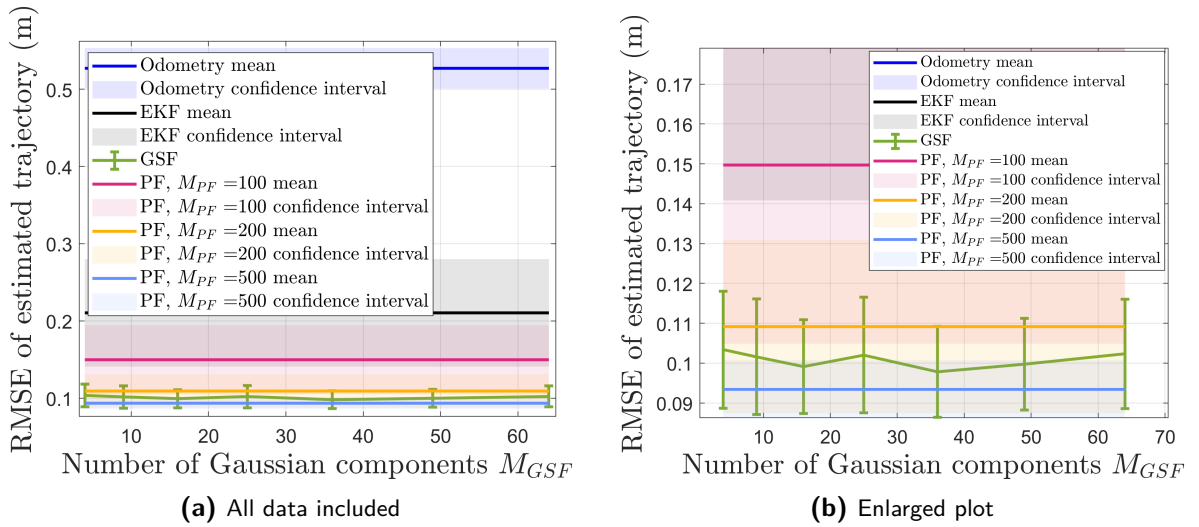


**Figure 4-8:** The RMSE of the estimated trajectories of the algorithms under different numbers of Gaussian components of the GSF for the magnetic field localization

### 4-2-3 Varied initial covariance matrices of the GSF $P_{11}^i$

To check what is the appropriate value to set for the initial covariances of the Gaussian components of the GSF, a simulation with varied initial covariance values was run and its settings and simulation results will be covered in this section.

- **Initialization of the algorithms:**

In this simulation, the initialization of the algorithms was set with an initial error  $\epsilon_0$  equal to 0.1.

- **GSF:**

The number of the Gaussian components  $M_{GSF}$  was set to the same value as did in Section 4-2-1.

The initial means of the GSF were set using the same equation as Eq. (4-4) and depended on the initial distribution of the EKF.

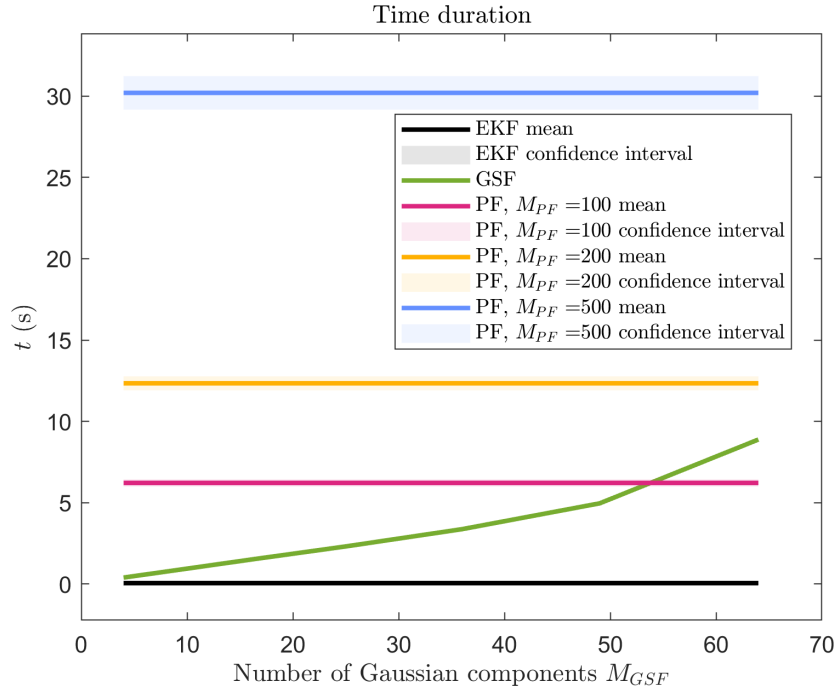


**Figure 4-9:** The time duration of each algorithm at each value of the number of Gaussian components  $M_{GSF}$

The initial covariances of the Gaussian components of the GSF were set as

$$\begin{bmatrix} P_{1|1,(x,x)}^i & 0 & 0 & 0 & 0 & 0 \\ 0 & P_{1|1,(y,y)}^i & 0 & 0 & 0 & 0 \\ 0 & 0 & 0.001 & 0 & 0 & 0 \\ 0 & 0 & 0 & 0.001 & 0 & 0 \\ 0 & 0 & 0 & 0 & 0.001 & 0 \\ 0 & 0 & 0 & 0 & 0 & 0.001 \end{bmatrix}, \quad (4-9a)$$

where

$$P_{1|1,(x,x)}^i = \left( \frac{\sqrt{P_{1|1,(x,x)}}}{M_{GSF,x}} \right)^2 \cdot \left( 0.1 + \frac{j-1}{9} \cdot \left( \frac{\sqrt{P_{1|1,(x,x)}}}{M_{GSF,x}} \right)^{-2} \right), \quad (4-9b)$$

$$P_{1|1,(y,y)}^i = \left( \frac{\sqrt{P_{1|1,(y,y)}}}{M_{GSF,y}} \right)^2 \cdot \left( 0.1 + \frac{j-1}{9} \cdot \left( \frac{\sqrt{P_{1|1,(y,y)}}}{M_{GSF,y}} \right)^{-2} \right), \quad (4-9c)$$

The value  $j$  was designed to be an integer of the set  $\{1, \dots, 10\}$ , so the  $X$  and  $Y$  covariance values of the GSF were set as 0.1 times the value in Eq. (4-5) to around 1 in this simulation.

The visualization of the initial Gaussian components of the GSF is shown in Figure 4-10. In Figure 4-10a, the covariances were set to small values. Through the simulation, the initial covariances grew to about 1 and are shown in Figure 4-10b.

– **EKF and PF:**

Similar to the simulation in Section 5-3-2, the initialization of the EKF and

the PF was kept constant throughout the simulation. The initial estimated position  $\hat{p}_{1|1}^w$  and covariance of the EKF were set using Eq. (4-2) and (4-3). The initial particles of the PF were sampled from the initial distribution of the EKF.

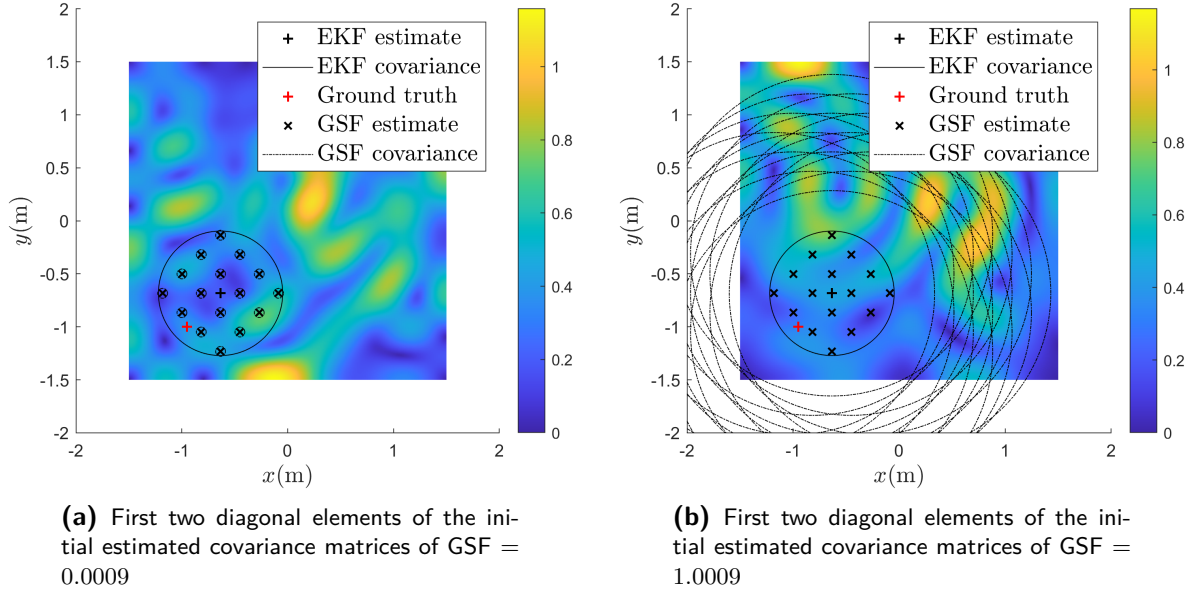


**Figure 4-10:** The visualization of the algorithm initializations for the magnetic field localization with varied initial covariance matrices of the GSF (Initial error = 0.1)

- **Simulation results:**

In this simulation, a Monte Carlo simulation was run with 100 iterations for different values of the initial covariances of the GSF. The simulation results are shown in Figure 4-11. Since only the initialization of the GSF is the one that varied through iteration, the results of the other algorithms are plotted with their means and 95% confidence interval through these 1000 iterations.

The error of the EKF is unsurprisingly higher than the PFs. The PFs also show an expected result that the larger the number of the particles  $M_{PF}$  is, the lower the RMSE of the trajectory is.

The RMSE of the GSF is stable even when the first two diagonal values of the initial covariances reach 1. An analysis of the possible reason was carried out and the possible reason for this phenomenon is the small measurement noise that limits the covariance values when performing measurement updates. A more detailed discussion of this analysis of the components of the GSF is shown in Appendix G-1.

One might argue the stable performance of the GSF is due to the initial setting that makes the initial covariances of the GSF mostly overlapped when the initial covariances were large, as shown in Figure 4-10b. However, this was proven not to be the reason for such stable error by a test with a larger initial error. The test was designed with an initial error equal to 0.2. The initial EKF distributions and the

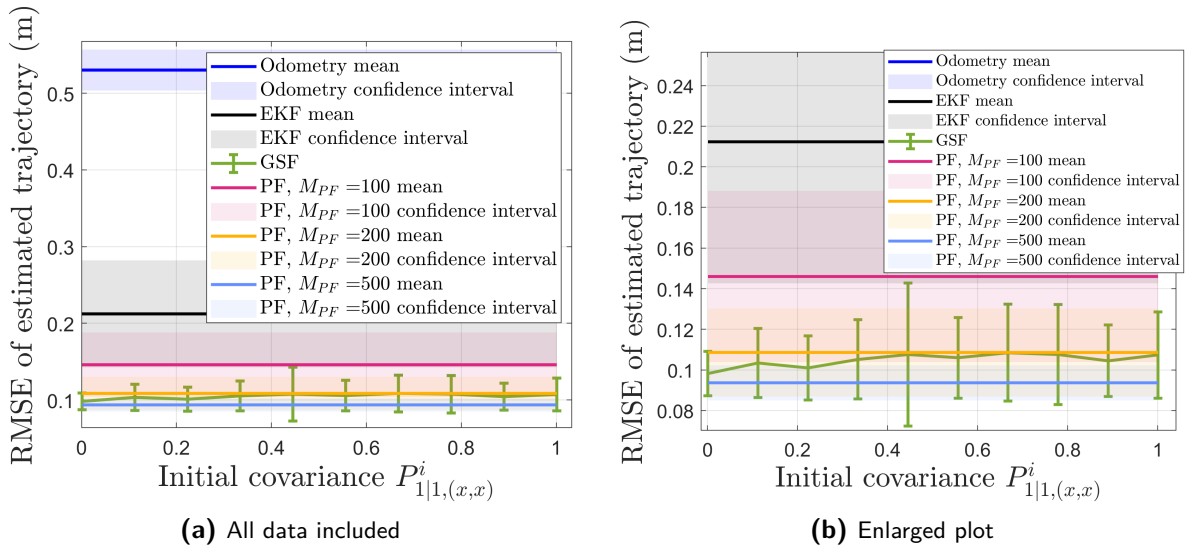


**Figure 4-11:** The RMSE of the estimated trajectories of the algorithms under different values of initial GSF covariance matrices for the magnetic field localization (Initial error = 0.1)

initial Gaussian components are plotted in Figure 4-12. As shown in Figure 4-12b, the covariances of the GSF are now less overlapping with each other. Nevertheless, the simulation results shown in Figure 4-13, the RMSE of the GSF is still robust to the initial covariance values.

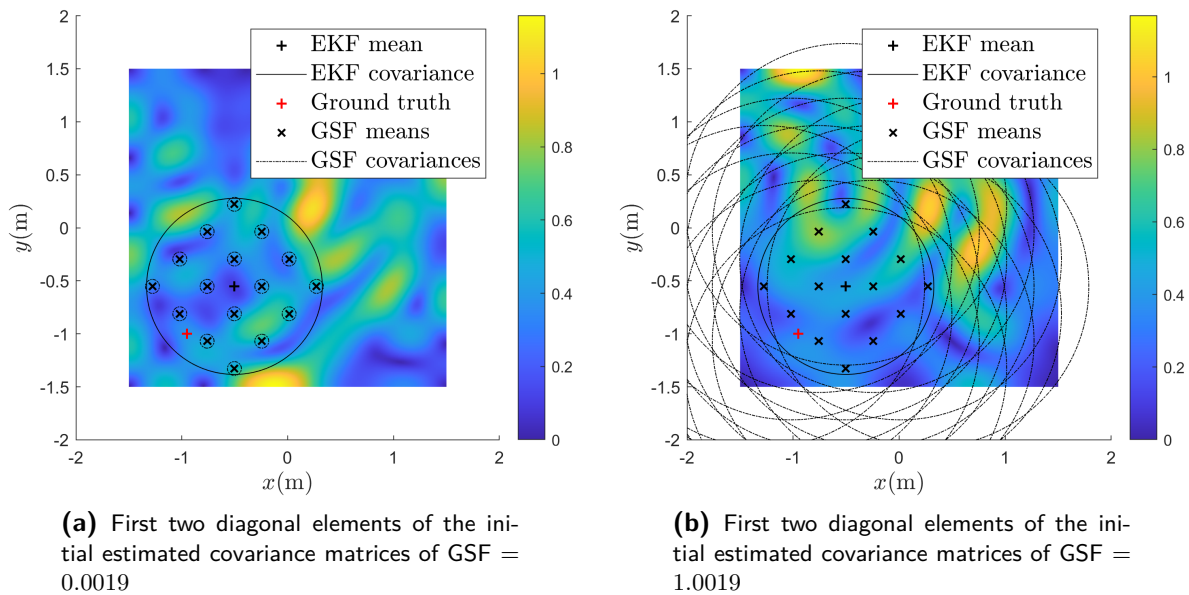


**Figure 4-12:** The visualization of the algorithm initializations for the magnetic field localization with varied initial covariance matrices of the GSF (Initial error = 0.2)

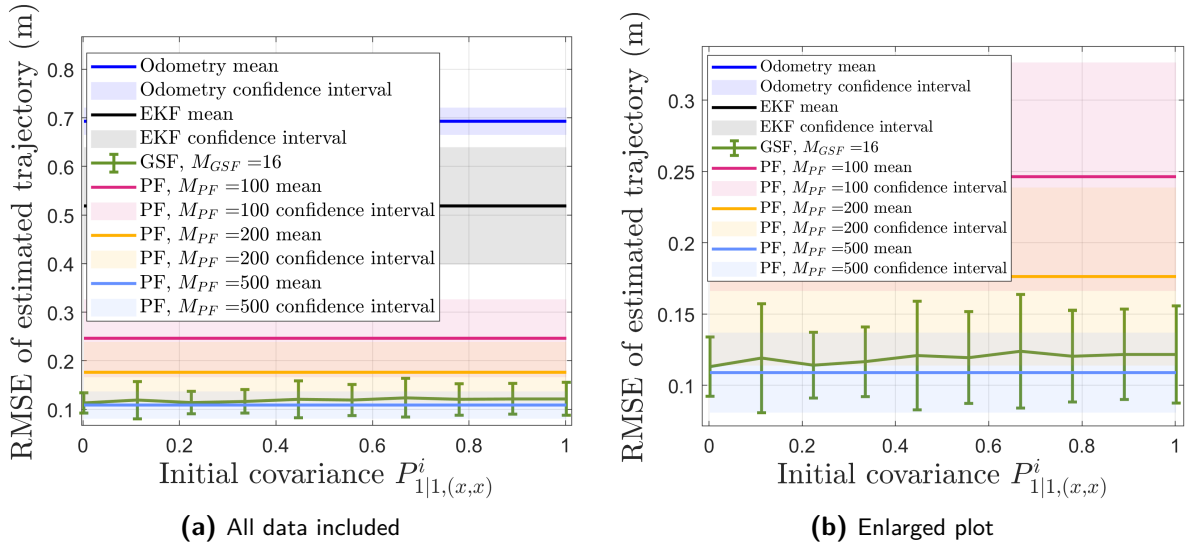


**Figure 4-13:** The RMSE of the estimated trajectories of the algorithms under different values of initial GSF covariance matrices for the magnetic field localization (Initial error = 0.2)

### 4-3 Conclusion

The simulations here were designed for the study of the possibility of the GSF to apply to magnetic field localization as the solution to the research gap. Therefore, the GSF was applied to the magnetic field simulation discussed in [38]. The simulation results of the GSF are compared with the results of the EKF and the PF that were built in [38].

With the simulation results, the GSF is proved to be more robust than the other algorithms when there exists a large initial uncertainty. As a large initial error will lead to multimodal distributions, this indicates the GSF is more applicable than the EKF when there exists multimodality.

Besides, two GSF properties were checked using the simulation of magnetic field localization. The number of the Gaussian components of the GSF  $M_{GSF}$  applied in this chapter was checked to be an appropriate choice by the test of varying  $M_{GSF}$ . During this test, the GSF is also shown quite efficient compared to the PF while keeping comparable accuracy. Moreover, the initial covariances of the GSF were varied to check what value is appropriate when initializing. The RMSE of the GSF did not vary much with the initial covariances, so the setting of the initial covariances was decided to be kept the same as the other simulations had.

# **Simulation results of magnetic field localization with real-world magnetometer measurements and the Gaussian sum filter (GSF) applied as an estimator**

In the previous chapter, the GSF was applied to a magnetic field localization system where all measurements and noises were simulated. From the simulated results, the GSF is proved to be suitable for multimodal distributions and is more efficient compared with the Particle filter (PF). To further strengthen the claim that the GSF is a solution to the research gap, the GSF implementation was also studied with a localization system with real-world magnetometer measurements.

The real-world magnetometer measurements were collected by Frida Viset, Gustaf Hendebý, and Ola Johansson at the motion capture lab at Linköping University via a magnetometer, Xsens MTi-300. They were calibrated by making the measurements of all orientations fitting a unit sphere, similar to what is done in [17]. The measurements for calibration were collected in the same space where the measurements for localization were collected. Note that no direct physical meaning is connected to the calibrated values. The norms of the calibrated measurements for magnetic field localization are shown in Figure 5-1. The position and orientation corresponding to the magnetometer measurements were collected via motion capture cameras at Linköping University with accuracy in millimeters.

In this chapter, the selection of the parameters for building the magnetic field map using the reduced-rank Gaussian process (GP) will be first introduced in Section 5-1. In Chapter 4, there are three Monte Carlo simulations for the study of the performance

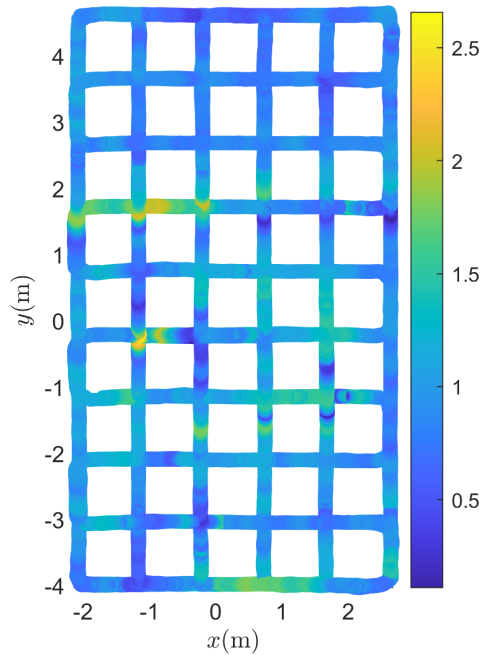


**Figure 5-1:** The norm of the measurements from the real-world magnetometer

of the GSF. These Monte Carlo simulations were also run in this chapter. Therefore, similar to Chapter 4, there will be an introduction to the settings that were kept constant through all simulations. Besides, the settings changed in different simulations and the discussion of the corresponding simulation results will be presented. At the end of this chapter, a brief conclusion based on this system with real-world measurements implemented will be given in Section 5-4. Since this chapter has a similar structure to Chapter 4, a structure plot is shown in Figure 5-2 to list the similar sections.

## 5-1 Choices of the parameters for building the magnetic field map

The map for the system in this chapter was built using a reduced-rank GP following the recursive progress shown in Eq. (2-31). There are several parameters that can be tuned when building the magnetic field map using Gaussian processes:

- **Range:**  
The range in  $Y$  direction of the area to localize was tested with two different values, 0.5 meters and 1.5 meters.
- **Length scale  $l_{SE}$**   
The length scale  $l_{SE}$  that is applied in Eq. (2-22) and (2-30).
- **$\sigma_{SE}$**   
The hyperparameter  $\sigma_{SE}$  that is applied in Eq. (2-22) and (2-30).

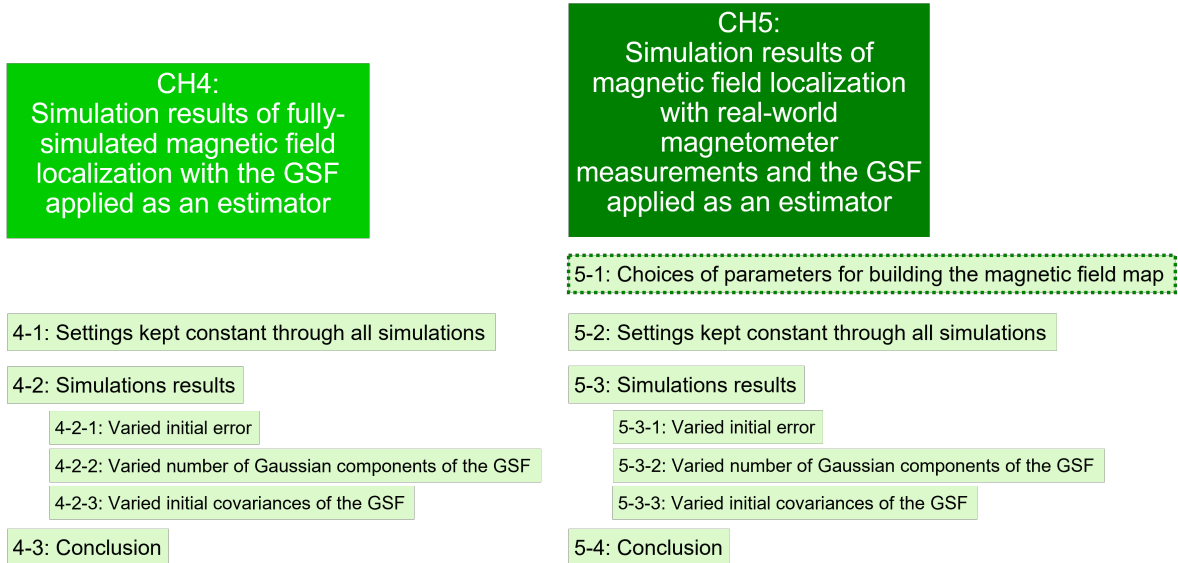


**Figure 5-2:** The structure of Chapter 4 and Chapter 5 (Similar sections are without dashed outline)

- **Data size**

The size of the data used for the training of the magnetic field maps using the reduce-rank GP.

- **Measurement noise  $\sigma_m$**

The guessed measurement noise  $\sigma_m$  used in Eq. (B-9c) and (2-31).

To decide what preferred values of the parameters for learning the map using the reduced-rank GP are, the map built using the reduced-rank GP was compared with the one built with the full-rank GP. The process of these comparisons and how the parameters were selected is shown in Appendix B. The final results of the selected parameter values are shown in Table 5-1.

Range (m)	$l_{SE}$	$\sigma_{SE}$	Data size	$\sigma_m$
1.5	0.3	0.1	$\approx 5000$	0.1

**Table 5-1:** Final decision of the parameters for establishing the magnetic field map using the reduce-rank GP

## 5-2 Settings kept constant through all simulations

In this section, the settings that were kept constant through the three simulations that will be discussed in the next section will be introduced. These settings are the trajectory, models, and algorithms.

### 5-2-1 Trajectory

The trajectory that will be the localization target is a part of the trajectory subtracted from the real-world measurement data set presented in Figure 5-1. The  $X - Y$  position of this trajectory is plotted in Figure 5-3. To reduce the computational effort for

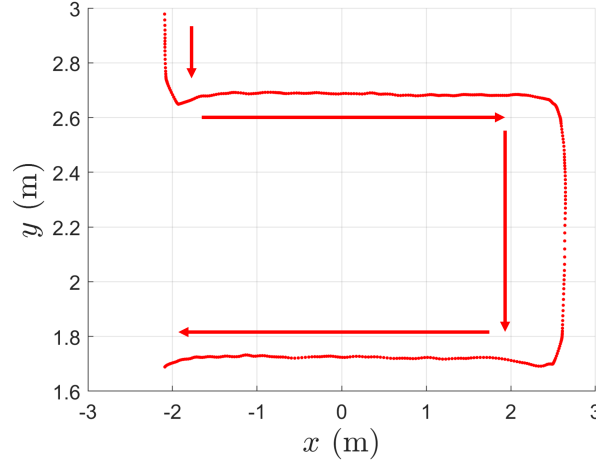


**Figure 5-3:** The true trajectory to estimate (arrow represents the direction of the trajectory)

simulation, the size of the data set for localizing is downsampled to 500 time steps. Note this data set is different from the one used for training the magnetic field map, and the sizes of the data sets were decided separately.

### 5-2-2 Models

The models applied in this system are the same as the ones introduced in Eq. (2-8), (2-9), and (2-24). In the following content, the magnetic field map, inputs, bias, and the noises in these models will be introduced.

#### Magnetic field map

The magnetic field map was built following Eq. (2-29) to (2-31) [18] as the measurements were from a real-world magnetometer with the parameters decided in Section 5-1, not the simply simulated data as set in the simulations in Chapter 4.

#### Inputs, bias, and noises

The input, transition position  $\Delta p_t^w$  and the transition  $\Delta q_t^b$ , were calculated from the known true position and orientation to mimic the uncertain transition data measurements. The process of how the extraction was done is similar to Eq. (4-1).

The measurement covariance of the transition position is set as

$$R_{dp} = \begin{bmatrix} 10^{-6} & 0 & 0 \\ 0 & 10^{-6} & 0 \\ 0 & 0 & 10^{-8} \end{bmatrix}. \quad (5-1)$$

The first two diagonal values were set to a larger value than the third one as the measurement in  $Z$  direction was assumed to be less uncertain. The measurement noise of the gyroscope was set as

$$R_{dq} = 10^{-6} \cdot \mathcal{I}_{3 \times 3}. \quad (5-2)$$

Besides, to demonstrate the advantages of using the algorithms and the magnetometer measurements for estimation calibration, a bias was introduced to the transition position subtracted from the already-known true position.

The bias is designed to create a drift that will make the endpoint 0.3 meters far away from the ground truth in both  $X$  and  $Y$  axes.

The resulting trajectory estimated with dead reckoning including this bias and the measurement noises without any initial error is shown in Figure 5-4 with the drift shown.

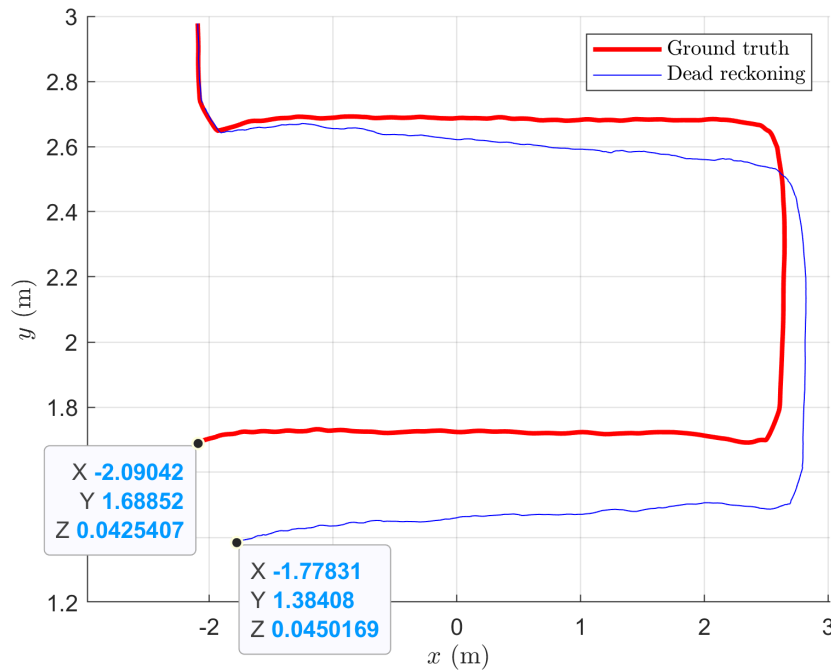


Figure 5-4: The estimated trajectory through dead reckoning

### 5-2-3 Algorithms

Similar to the simulations introduced in Chapter 4, the simulations with real-world measurements were also run with the Extended Kalman filter (EKF), the PF, and the

GSF. Here, the settings of these algorithms that were not varied through different simulations are introduced.

- **Extended Kalman filter (EKF)**

The settings of the EKF are similar to what is introduced in Section 4-1-3. The initial mean of the position  $\hat{p}_{1|1}^w$  was set using Eq. (4-2). The initial mean of the orientation was set to the same value as the initial ground truth of the orientation because the orientation was assumed to have less uncertainty than the position.

The initial covariance for Eq. (2-33f) was set as

$$P_{1|1} = \begin{bmatrix} 1.5\epsilon_0 & 0 & 0 & 0 & 0 & 0 \\ 0 & 1.5\epsilon_0 & 0 & 0 & 0 & 0 \\ 0 & 0 & 10^{-8} & 0 & 0 & 0 \\ 0 & 0 & 0 & 10^{-8} & 0 & 0 \\ 0 & 0 & 0 & 0 & 10^{-8} & 0 \\ 0 & 0 & 0 & 0 & 0 & 10^{-8} \end{bmatrix}, \quad (5-3)$$

where  $\epsilon_0$  is the initial error and the value “1.5” multiplied by the initial error was designed in order to make the ground truth within the 68% confidence interval. Compared with the setting in Eq. (4-3), the values for components that were not related to  $X$  and  $Y$  positions were set to smaller values,  $10^{-8}$ .

- **Particle filter (PF)**

The number of the particles was set to values equal to 100, 200, and 500 to observe if the accuracy of the PF would increase with the number of the particles.

The initial distribution that the sampling of the particles depended on was set to the same initial distribution of the EKF.

- **Gaussian sum filter (GSF)**

The GSF in this chapter was also set similarly as in Section 4-1-3. The diamond region depended on the initial means and covariances of the EKF, so the values would also vary through simulations as the initial error was designed differently in the simulations. The only difference existed in the last four diagonal values of initial covariances of the Gaussian components. Here, the values were set to  $10^{-8}$ .

Note that the code for the EKF and the PF are based on [38].

The algorithm settings of the three algorithms are similar to what is introduced in Chapter 4. Therefore, the reader can refer to Table 4-1 for clearer settings of the algorithms. Note that the initial covariances are slightly different in value as shown in Eq. (5-3) and the values of other settings might be varied due to the different purposes of the simulations.

## 5-3 Simulation settings and results

Similar to the simulations discussed in Chapter 4, there were 3 simulations each with different variables changed through the simulation to observe the performance of the 3

algorithms introduced in 5-2-3. The variables that varied in the three simulations are

- Initial error of the estimated position  $\epsilon_0$
- Number of Gaussian components of the GSF  $M_{GSF}$
- Initial covariance matrices of the GSF  $P_{1|1}^i$

and the purpose of varying these variables was also introduced in Section 4-2.

Different from the simulation results shown in Chapter 4, the results in this chapter will be discussed with different percentages of the whole trajectory. In Chapter 4, the results of the simulations were presented with the root mean squared error (RMSE) of the entire trajectory. However, in this chapter, the results will sometimes be shown with part of the trajectory. This is because the estimators might act inaccurately at the beginning of the localization and these initial inaccuracies could be misleading when looking at the RMSE of the whole trajectory. To avoid this condition, the RMSE will be discussed when looking at the whole trajectory, the last 80% of the trajectory, and the last 67% of the trajectory. An illustration demonstrating what these percentages mean is shown in Figure 5-5.

The following subsections are the introduction of the customized settings of the algorithms for each simulation and the corresponding simulation results.

### 5-3-1 Varied initial error $\epsilon_0$

As discussed previously in Section 1-2, when the initial uncertainty is large, it is more possible for the multimodal distribution to happen. As a result, the initial error  $\epsilon_0$  in this simulation was set with different values to observe the robustness of the GSF to multimodality compared with the other algorithms.

The initial error in this simulation is designed to be varied from 0.0025 to 0.2. This can also be written as

$$\epsilon_0 = 0.0025 + \frac{j-1}{9} \cdot 0.1975, \quad (5-4)$$

where  $j \in \{1, \dots, 10\}$ . A visualization of how the initialization of the EKF and the GSF changed with different initial errors is shown in Figure 5-6, where the initial uncertainty grows as the initial error is set to larger values.

- **Initialization of the algorithms**

The initialization of the algorithms was similar to the one applied in Section 4-2-1.

- **EKF**

As the initial error varied through the simulation, the initial mean and covariance of the EKF also varied through simulation. The initial distribution was calculated by implementing the initial error value in Eq. (5-4) to the mean and the covariance in Eq. (4-2) and (5-3).

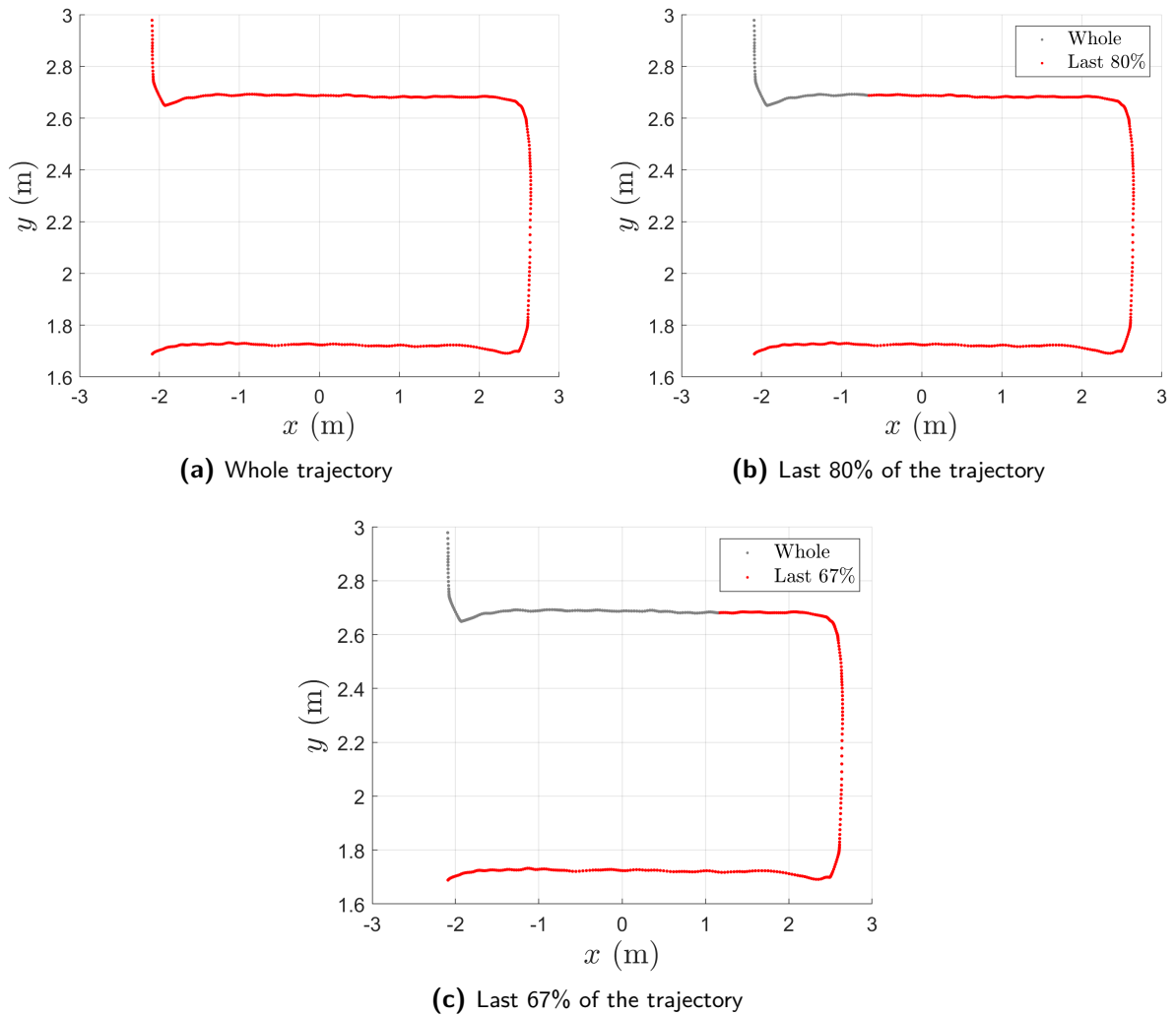


**Figure 5-5:** The illustration showing how the trajectories are analyzed partially

– **PF**

The initial particles of the PF were sampled from the initial distribution of the EKF.

– **GSF**

The number of the Gaussian components was set to 4, 16, and 64 with the Gaussian components approximating the covariance ellipsoid of the EKF with a diamond shape.

The initial means and the covariances were set in the way introduced in 5-2-3.

• **Simulation results**

The simulation was run as a Monte Carlo simulation with 100 experiments for each initial error value. The results of the three algorithms are shown with the RMSE of different parts of the trajectories.

From the difference between the plots shown in Figure 5-7, the GSFs with 16 and 64 Gaussian components has a decreasing trend as the trajectory taken into

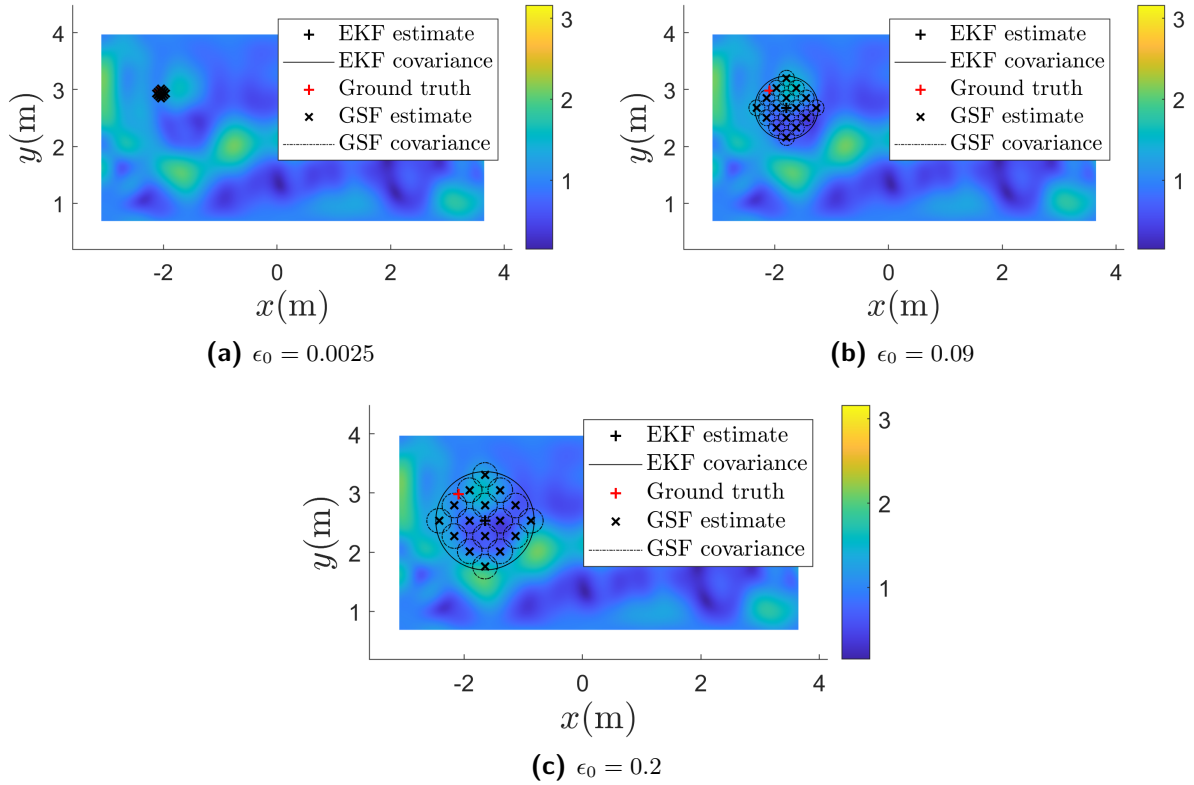


**Figure 5-6:** The initialization of the EKF and the GSF with varied values of initial error  $\epsilon_0$

account contains fewer starting parts. When only the last 80% of the trajectory is analyzed, the GSFs with a large enough number of Gaussian components (larger or equal to 16) outperforms the other algorithms with low and stable error.

As the initial error grows, the range of uncertainty reaches the area where the distribution becomes multimodal. This can also be observed from the distribution that the algorithms estimated at time step  $t = 2$  in Figure 5-8. As the initial error is large enough to trigger the multimodality, the EKF shows a large error while the GSF is still keeping low RMSE. Therefore, the GSF shows the capability of estimating the position accurately even when there exists the multimodal distribution with simulations including the real-world magnetometer measurements.

### 5-3-2 Varied numbers of Gaussian components of the GSF $M_{GSF}$

In this simulation, the number of the Gaussian components of the GSF was varied. Besides observing the relationship between the accuracy and the number of the Gaussian components, the time durations of the GSF and the PF had for each value of the number of the Gaussian components will be compared to check if the GSF is more efficient than the PF while the accuracy is still kept at a similar or even better level.

The number of the Gaussian components of the GSF was set from 4 to 64. The

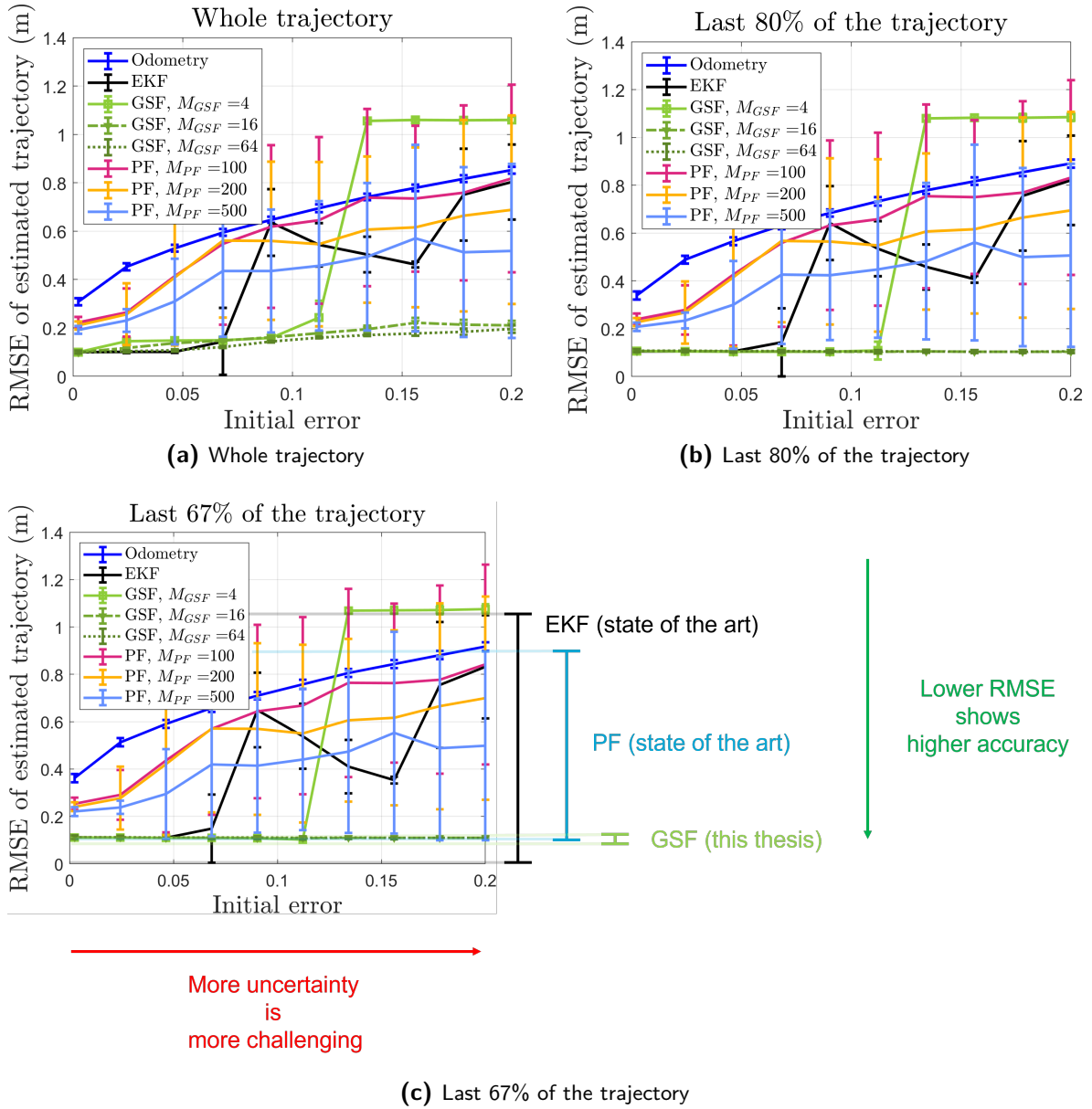


**Figure 5-7:** The RMSE of the estimated trajectories from different algorithms under varied values of initial error  $\epsilon_0$

illustrations of the GSF initialization with different values of the number of the Gaussian components are shown in Figure 5-9.

As observed in Section 5-3-1, there existed multimodal distributions when the initial error was larger than 0.07. As a result, to discuss the accuracy of the algorithms when multimodality appears, the initial error  $\epsilon_0$  in this simulation was set to 0.07.

- Initialization of the algorithms

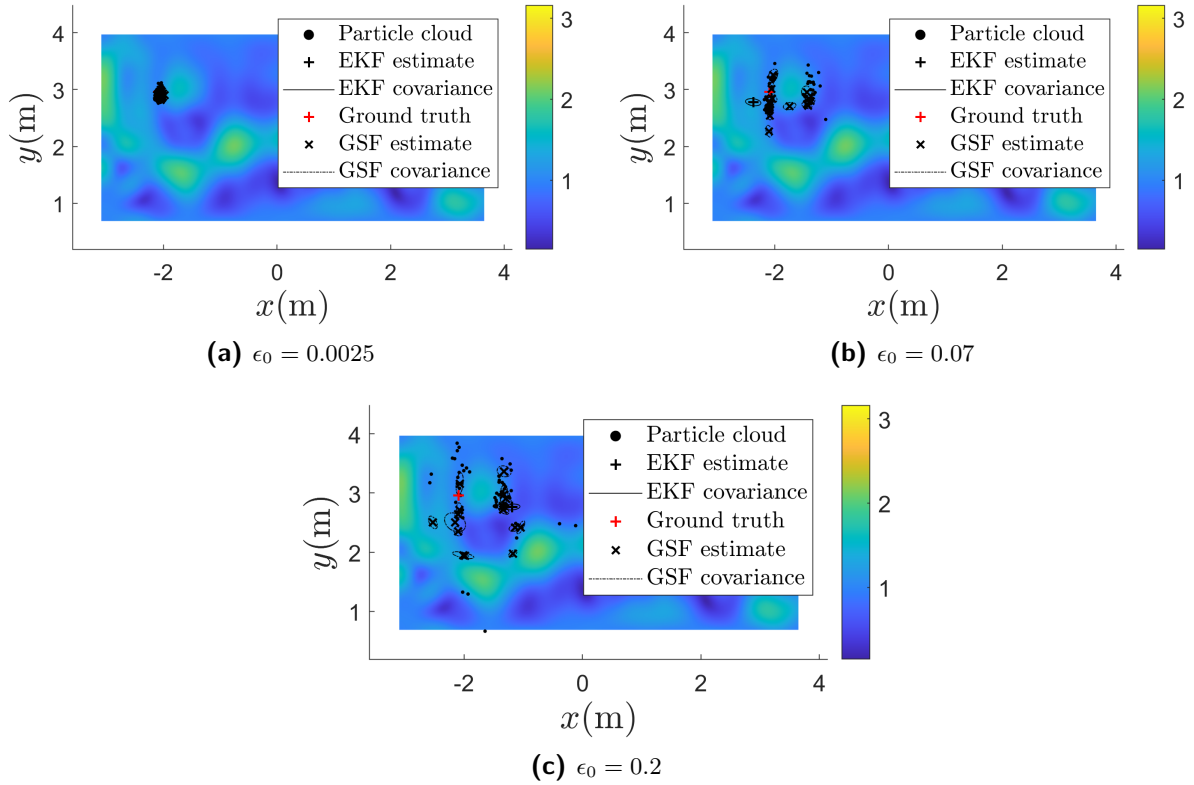


**Figure 5-8:** The distribution estimated by the algorithms when  $t = 2$  under varied values of initial error  $\epsilon_0$

– **GSF**

The number of the Gaussian components of the GSF was set to 7 values: 4, 9, 16, 25, 36, 49, and 64. As the Gaussian components were designed to approximate the initial covariance ellipsoid of the EKF with a 2-dimensional diamond on the  $X - Y$  plane, the number of the Gaussian components on each side of the diamond was then 2, 3, 4, 5, 6, 7, and 8.

The initial means of the Gaussian components were scattered equally in the range defined using Eq. (4-4), and the initial covariances were assigned following Eq. (4-5) based on the initial distribution of the EKF.

– **EKF and PF**

As the initial error  $\epsilon_0$  for this simulation was set to 0.07, the initialization of the EKF and the PF were kept the same throughout the simulation. The initial position and covariance of the EKF were set as shown in Eq. (4-2) and Eq. (5-3). The initial particles of the PF were sampled from the initial distribution of the EKF.

• **Simulation results**

The simulation was again run as a Monte Carlo simulation with 100 experiments for each value of the number of Gaussian components of the GSF. Since this simulation was designed to observe the change in the performance of the GSF, the results of the EKF and the PF are shown with the mean and the 95% confidence

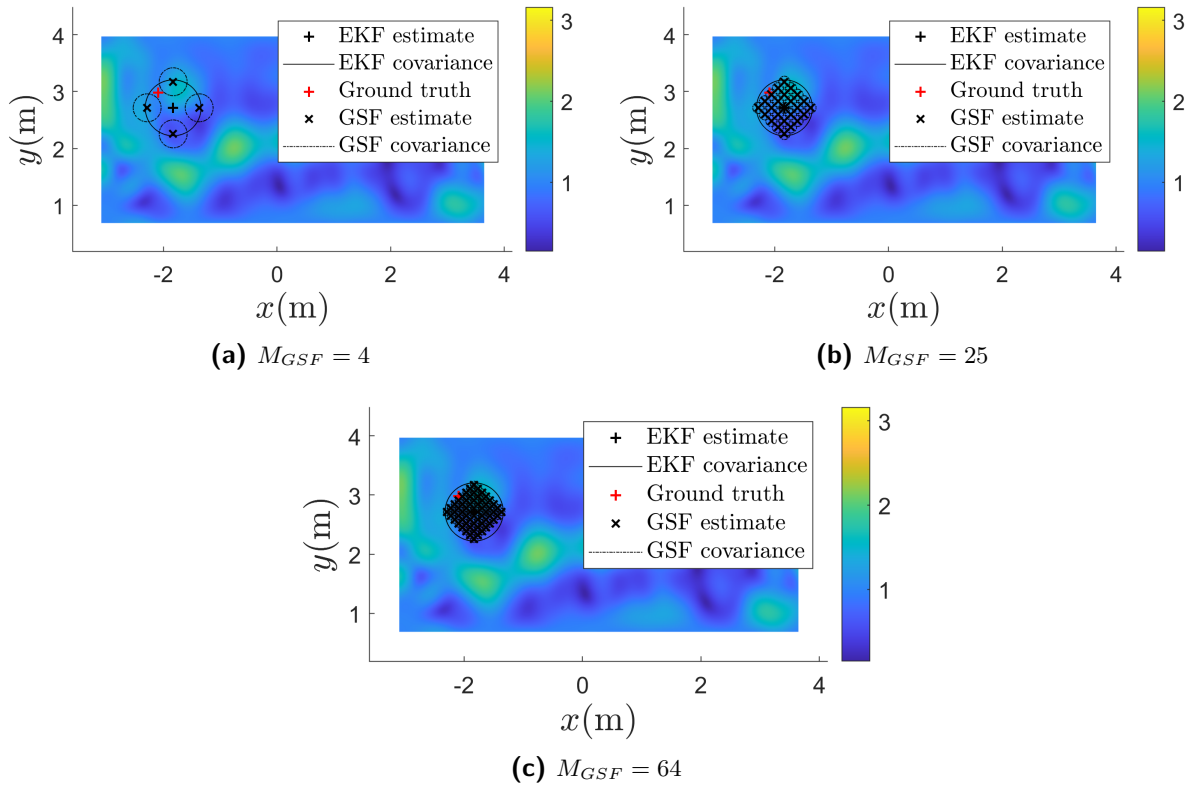


**Figure 5-9:** The initialization of the EKF and the GSF with different values for the number of the Gaussian components of the GSF  $M_{GSF}$

interval.

As mentioned previously, the time duration recorded in this simulation could be used as a check to see if the GSF is more efficient than the PF while having better accuracy compared with the EKF when there is multimodality. As seen in Figure 5-10, the GSF is more efficient compared with the PF when the number of the Gaussian components of the GSF is lower than 50.

Furthermore, from the RMSE of the trajectories shown in Figure 5-11, the GSF shows a low error compared to the other algorithms. This implies that with the number of Gaussian components lower than 50, the GSF is indeed more efficient than the PF and also more accurate than the EKF when there is multimodality. Moreover, as seen from Figure 5-11, the PF with 500 particles is still having higher error compared with the GSF. Therefore, even with the GSF with 64 Gaussian components, it will be more efficient compared with the PF if the number of the particles is added to the amount to have equally accurate results to the GSF.

### 5-3-3 Varied initial covariance matrices of the GSF $P_{1|1}^i$

This simulation is designed to discuss the suitable values for the initial covariances of the Gaussian components of the GSF. The settings were similar to the one introduced in Section 4-2-3.

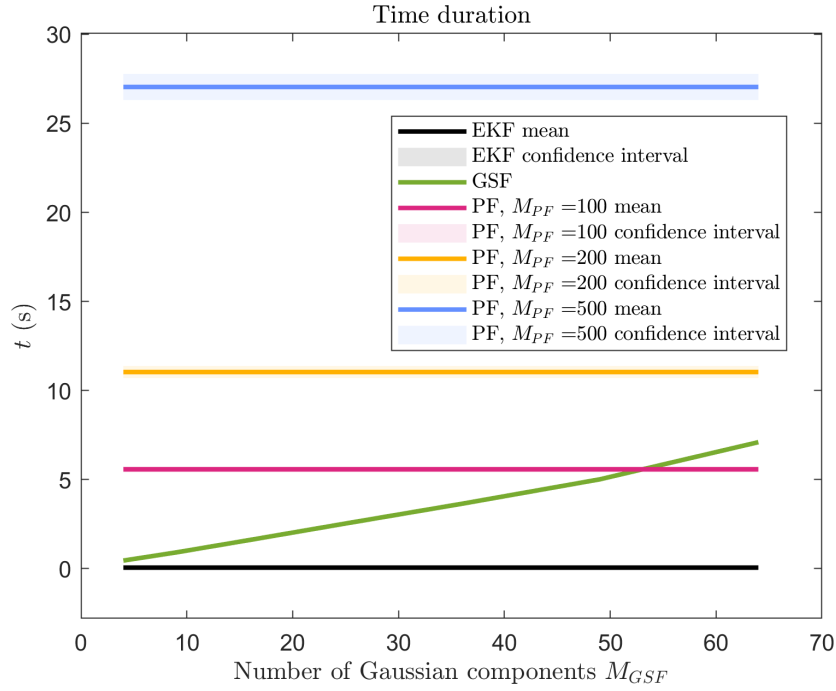


**Figure 5-10:** Time duration of the algorithms under different values of the number of Gaussian components of the GSF  $M_{GSF}$

- **Initialization of the algorithms**

The initial error  $\epsilon_0$  set in this simulation is equal to the one mentioned in Section 5-3-2, with  $\epsilon_0 = 0.07$ .

- **GSF**

The number of the Gaussian components of the GSF was set in the same way as introduced in 5-3-1.

The initial means were designed to approximate the initial 68% confidence covariance ellipsoid of the EKF in a diamond shape in the range defined using Eq. (4-4).

The initial covariance values corresponding to the position in  $X$  and  $Y$  axes of the Gaussian components were designed to vary from 0.1 times the normal settings (settings based on Eq. (4-5)) to about value 1. Therefore, the values of the initial covariance related to the position in  $X$  and  $Y$  axes can be written as

$$P_{1|1,(x,x)}^i = \left( \frac{\sqrt{P_{1|1,(x,x)}}}{M_{GSF,x}} \right)^2 \cdot \left( 0.1 + \frac{j-1}{9} \cdot \left( \frac{\sqrt{P_{1|1,(x,x)}}}{M_{GSF,x}} \right)^{-2} \right), \quad (5-5)$$

$$P_{1|1,(y,y)}^i = \left( \frac{\sqrt{P_{1|1,(y,y)}}}{M_{GSF,y}} \right)^2 \cdot \left( 0.1 + \frac{j-1}{9} \cdot \left( \frac{\sqrt{P_{1|1,(y,y)}}}{M_{GSF,y}} \right)^{-2} \right), \quad (5-6)$$

where  $j \in \{1, \dots, 10\}$ . The values of the other diagonal elements were set the same as mentioned in 5-2-3. An illustration of how the GSF looks like with the smallest and largest initial covariance values is shown in Figure 5-12.

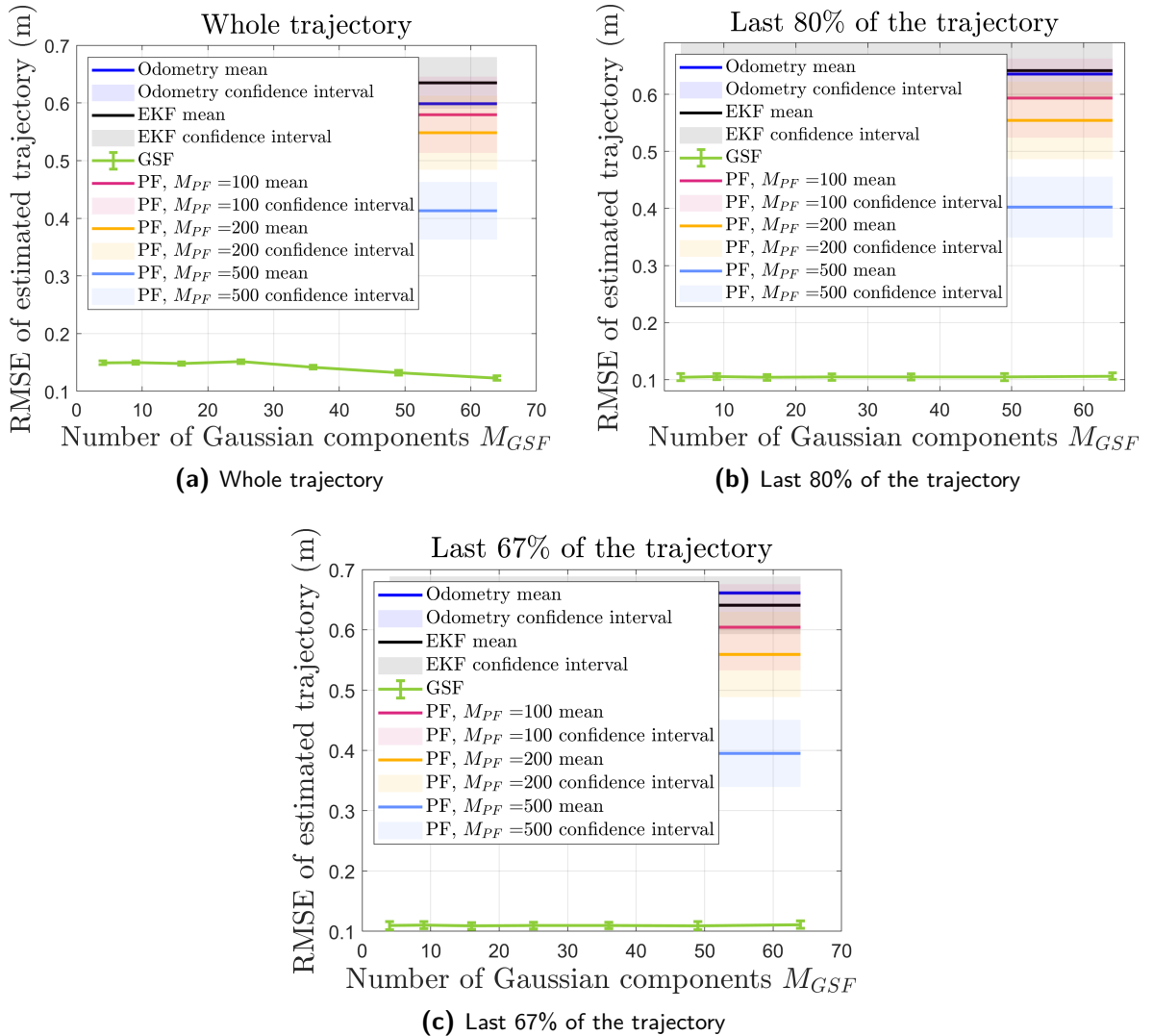


**Figure 5-11:** The RMSE of the estimated trajectories of different algorithms under varied values of the number of the Gaussian components of the GSF  $M_{GSF}$

– **EKF and PF**

The settings for the initialization of the EKF and the PF were identical to the ones in Section 5-3-2.

• **Simulation results**

The simulation in this section was run as a Monte Carlo simulation with 100 experiments. Because the settings of the EKF and the PF were kept the same through the simulation, the results of these two algorithms will be shown with the mean and the 95% confidence interval.

The simulation results here are also presented with the RMSE of different parts of the trajectories. Furthermore, in this simulation, the results will also be discussed with the last 50% of the trajectory. The visualization of the last 50% of the trajectory compared with the entire trajectory is shown in Figure 5-13.

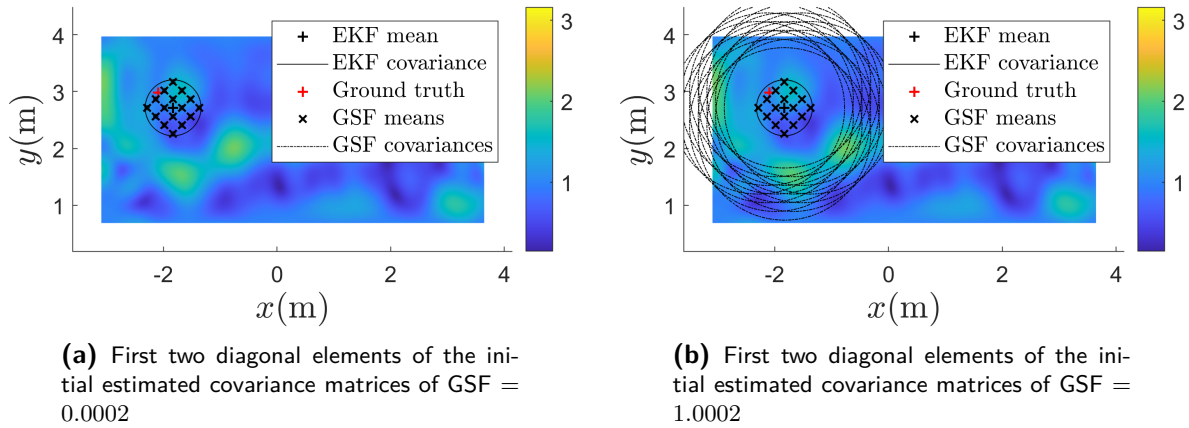


**Figure 5-12:** The visualization of the algorithm initializations for the magnetic field localization with the smallest and largest initial covariances the GSF (Initial error = 0.07)

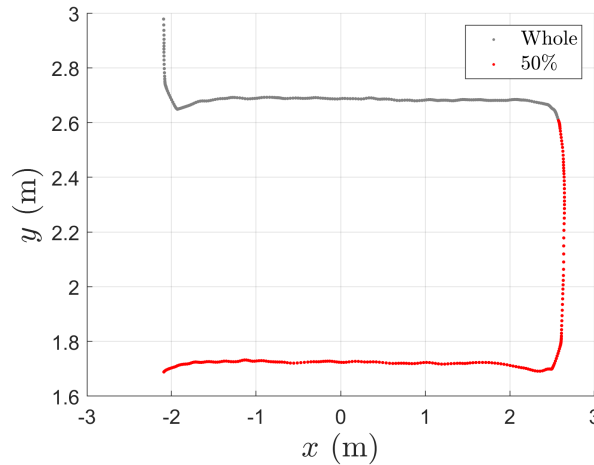


**Figure 5-13:** The illustration showing the last 50% of the trajectory compared with the whole trajectory

As shown in Figure 5-14, the error of the GSFs is high if the whole trajectory is taken into account when calculating the RMSE. However, if the region is narrowed down to the part of the trajectory that is a certain distance away from the starting point, the results are then as stable as what is also seen in the purely simulated case in Section 4-2-3. An analysis of this stable performance of the GSF was also carried out and the possible reason for this phenomenon was found to be the small value set for the measurement noise. For a more detailed discussion of the analysis, the reader can see Appendix G-2.

## 5-4 Conclusion

In this chapter, the GSF was applied to the magnetic field localization system with real-world magnetometer measurements. Since the measurement data was from real-world

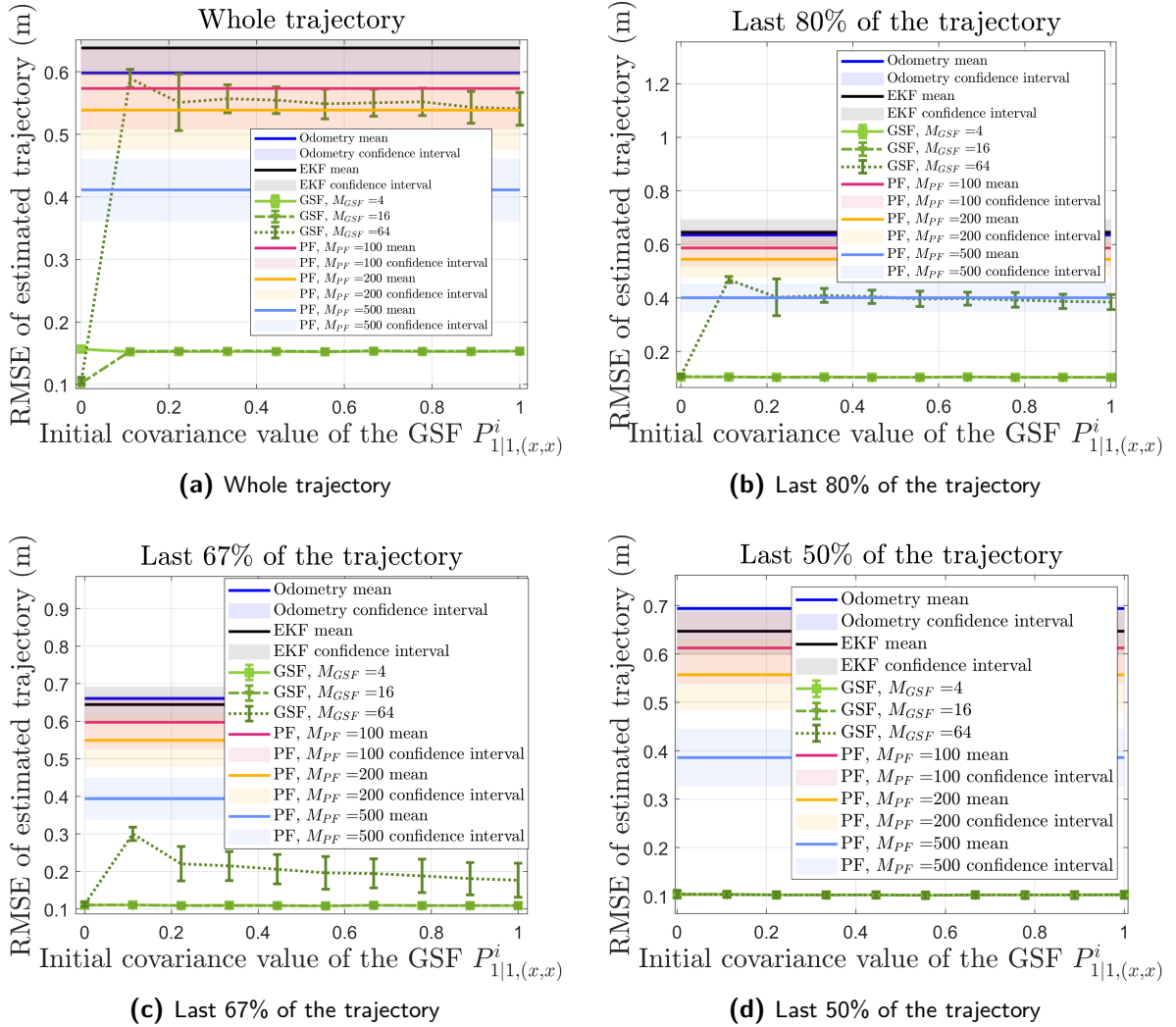


**Figure 5-14:** The RMSE of the estimated trajectories of different algorithms under varied values of the initial covariances of the GSF  $P_{1|1}^i$

magnetometers, more uncertainties were introduced.

Three simulations that were done in Chapter 4 were again run with this real-world measurement system. The GSF is again proved to be more suitable for multimodal distribution than the EKF by the simulation results with varied initial errors. The GSF is also shown to be more efficient than the PF in the simulation varying the number of the Gaussian components. In the simulation varying the initial covariances of the GSF, the GSF is again found not sensitive to large initial covariance values.

---

## Chapter 6

---

# Conclusion

Magnetometers are widely equipped in smartphones today, and this makes them easily accessible sensors. Furthermore, the measurement of the magnetic field is not a transition measurement like what accelerometers and gyroscopes have, so there is no drift when estimating position and orientation using magnetometers. Moreover, magnetometers require no additional signal senders or receivers in the indoor environment for localization. With these advantages, the study of magnetometers as sensors for indoor localization is valuable.

However, in the current studies in localization using magnetometers, there exists a research gap in the algorithms applied to magnetic field localization for position and orientation estimation. The Extended Kalman filter (EKF) has been applied as an estimator in a previous study [38]. It is efficient since it relies on linear algebra for the approximation of the state in each time step. Nevertheless, as it is based on the assumption that the distributions are unimodal Gaussian distributions, it is not an ideal algorithm when initial uncertainty is large. The reason for this disadvantage is that the measurement model for magnetic field localization is a combination of sinusoidal functions and these periodic functions could introduce multimodality to the system. When the initial uncertainty is large, the linearization in the EKF might be invalid and multimodality can lead to a completely wrong estimation as the starting position is already at the area where the distribution of the state cannot be simply assumed as an unimodal Gaussian distribution.

Besides the EKF, a Particle filter (PF) has also been applied to magnetic field localization in previous research [30]. Since the PF does not rely on the assumption that the distributions are unimodal Gaussian distributions, it is possible to perform better in accuracy compared to the EKF when the initial uncertainty is large. Nonetheless, the payoff of this benefit is the computational cost.

As a result, in the studies of magnetic field localization so far, there is a research gap for the algorithms applied for position and orientation estimation. The gap is made by

the lack of an algorithm that is more efficient than the PF, but also more robust to multimodality compared to the EKF.

The Gaussian sum filter (GSF) is found to be a possible solution to this research gap. It can approximate multimodal distributions with Gaussian mixtures, so it is expected to be more suitable for multimodality than the EKF. Furthermore, the amount of Gaussian components of a GSF is often much less than the particles of a PF, so the GSF could be an algorithm that is more efficient than the PF. To find out if the GSF is a solution to the research gap, several simulations were run with the GSF as the estimator of the position and orientation.

The GSF was applied to two sets of simulations. The measurements of the first set of simulations were all simulated. Therefore, the magnetic field map was built based directly on the given distribution of the weight vector  $m$ . On the other hand, the magnetometer measurements of the second set of simulations were from a real-world magnetometer. Hence, the magnetic field map in this set was built following the recursive process shown in Eq. (2-31). With the first set of simulations, the results were checked under less uncertain conditions. After the check using the pure simulations of the first set, the GSF was implemented in the second set of simulations, where more uncertainty was introduced because of the real-world magnetometer measurements. There were three simulations in each set and the settings were mostly the same for the sets.

In the first simulation, the initial error was varied to trigger the multimodality of the magnetic field localization system. By increasing the initial error, it is more likely the distribution is multimodal. This is also a simulation run in the previous study [38]. From the simulation results analyzed using the root mean squared error (RMSE)s of both sets, the GSF is found to be more suitable for multimodal distributions compared with the EKF with lower estimation error when the initial error is large.

The second simulation was set with various numbers of the Gaussian components of the GSF. From the RMSEs of both sets, there is no obvious threshold found as the appropriate number of Gaussian components for the GSF to achieve enough accuracy. Furthermore, it is found that the GSF is more efficient compared with the PF when the GSF is equally or more accurate than the PF.

In the last simulation, the initial covariances of the GSF were varied to check what is the appropriate value to set as the initial covariance values of the Gaussian components of the GSF. The results of both sets show that the accuracy of the GSF does not change significantly with the initial covariance values. As a result, the initial covariance values of the GSF set in the other simulations were kept as they were originally set.

From the results of the simulations of magnetic field localization, the possibility of the GSF as the solution to the research gap in magnetic field localization is proven to be quite positive. The GSF is shown to be more efficient compared to the PF while more suitable to the multimodal distributions than the EKF.

## Possible future works

As found in the analysis of the simulation results varying the initial covariances of the GSF shown in Appendix G, the covariances might grow too large if the localization duration is long enough. Thus, the design of a strategy to decompose Gaussian components with too large covariances might be necessary. Therefore, this decomposing strategy is a possible future work as the extension of this thesis project. Furthermore, since decomposing Gaussian components implies an increase in computational time as the number of Gaussian components increases, a strategy to merge repetitive or useless Gaussian components will also be needed.

In addition, the measurements of the transition position and orientation were only simulated in this thesis project. Thus, a potential future work is to implement real-world measurements from accelerometers and gyroscopes to further study the performance of the GSF under more uncertain and realistic situations.



---

# Appendix A

---

## Measurement model

In this chapter, the close form of the measurement model after applying the reduced-rank Gaussian process will be presented analytically based on the explanation shown in [38].

As shown in Section 2-2-3, the measurement model with the reduced-rank Gaussian process (GP) is

$$y_t^b = R_t^{bw} \nabla_p \Phi(p_t^w) m + e_{m,t}^b, \quad (\text{A-1})$$

where the basis function matrix  $\Phi(p_t^w)$  and the basis functions  $\phi_i(p_t^w)$  are given in 2-26 and 2-27a. For simpler notation, the following derivation will simplify the notation of position  $p_t^w$  as

$$p_t^w = p = \begin{bmatrix} p_x & p_y & p_z \end{bmatrix}^\top = \begin{bmatrix} p_1 & p_2 & p_3 \end{bmatrix}^\top. \quad (\text{A-2})$$

The matrix  $\nabla_p \Phi(p)$  can be separated into two parts as

$$\nabla_p \Phi(p) = \begin{bmatrix} (\nabla_p \Phi(p))_{1:3} & (\nabla_p \Phi(p))_{4:N_m+3} \end{bmatrix} \in \mathbb{R}_{3 \times (3+N_m)}. \quad (\text{A-3})$$

For the first part,

$$(\nabla_p \Phi(p))_{1:3} = \mathcal{I}_3. \quad (\text{A-4})$$

For the second part,

$$(\nabla_p \Phi(p))_{4:N_m+3} = \begin{bmatrix} \nabla_p \phi_4(p) & \dots & \nabla_p \phi_{N_m+3}(p) \end{bmatrix}, \quad (\text{A-5})$$

where

$$\nabla_p \phi_i(p) = \begin{bmatrix} \frac{\partial \phi_i(p)}{\partial p_1} \\ \frac{\partial \phi_i(p)}{\partial p_2} \\ \frac{\partial \phi_i(p)}{\partial p_3} \end{bmatrix} = \begin{bmatrix} \frac{\pi n_{i,1}}{L_{u,1}-L_{l,1}} C_1 S_2 S_3 \\ \frac{\pi n_{i,2}}{L_{u,2}-L_{l,2}} S_1 C_2 S_3 \\ \frac{\pi n_{i,3}}{L_{u,3}-L_{l,3}} S_1 S_2 C_3 \end{bmatrix}, \quad \text{for } i \in \{4, \dots, N_m + 3\}, \quad (\text{A-6})$$

$$s_d = \frac{\sqrt{2}}{\sqrt{L_{u,d} - L_{l,d}}} \sin \left( \frac{\pi n_{i,d}}{L_{u,d} - L_{l,d}} (p_d - L_{l,d}) \right), \quad (\text{A-7a})$$

$$c_d = \frac{\sqrt{2}}{\sqrt{L_{u,d} - L_{l,d}}} \cos \left( \frac{\pi n_{i,d}}{L_{u,d} - L_{l,d}} (p_d - L_{l,d}) \right). \quad (\text{A-7b})$$

As a result, the measurement model will end up as a function of the multiplication of sinusoidal functions of  $p_t^w$ .

---

## Appendix B

---

# Magnetic field map selection process

In this appendix, the process of the decision of the parameters for building the magnetic field map using reduced-rank Gaussian process (GP) will be introduced.

To build the maps and evaluate the results, the data was divided into the training data set and the test data set. Following is the introduction of the notation for these data sets.

- **Training data set**

The magnetometer measurements of the training data set are expressed in the following form

$$Y_{train}^b = [y_{train,1}^b \quad y_{train,2}^b \quad y_{train,3}^b \quad \cdots \quad y_{train,N_{train}}^b] \in \mathbb{R}^{3 \times N_{train}}, \quad (\text{B-1a})$$

where  $y_{train,i}^b = [y_{train,i}^{b,x} \quad y_{train,i}^{b,y} \quad y_{train,i}^{b,z}]^T \in \mathbb{R}^3$ .

The positions of the training data set are also noted with *train* as listed below:

$$P_{train}^w = [p_{train,1}^w \quad p_{train,2}^w \quad p_{train,3}^w \quad \cdots \quad p_{train,N_{train}}^w] \in \mathbb{R}^{3 \times N_{train}}, \quad (\text{B-2a})$$

where  $p_{train,i}^w = [p_{train,i}^{w,x} \quad p_{train,i}^{w,y} \quad p_{train,i}^{w,z}]^T \in \mathbb{R}^3$ .

The orientations are also noted with *train* to be differed from the test data in the following notation:

$$Q_{train}^{wb} = [q_{train,1}^{wb} \quad q_{train,2}^{wb} \quad q_{train,3}^{wb} \quad \cdots \quad q_{train,N_{train}}^{wb}] \in \mathbb{R}^{4 \times N_{train}}, \quad (\text{B-3a})$$

where  $q_{train,i}^{wb} = [q_{train,i}^{wb,I} \quad q_{train,i}^{wb,II} \quad q_{train,i}^{wb,III} \quad q_{train,i}^{wb,I}]^T \in \mathbb{R}^4$ .

- **Test data set**

The test data is noted with *test* in a similar way shown when introducing the

training data set. The magnetometer measurements of the test data are written as

$$Y_{test}^b = \begin{bmatrix} y_{test,1}^b & y_{test,2}^b & y_{test,3}^b & \cdots & y_{test,N_{test}}^b \end{bmatrix} \in \mathbb{R}^{3 \times N_{test}}, \quad (\text{B-4a})$$

where  $y_{test,i}^b = \begin{bmatrix} y_{test,i}^{b,x} & y_{test,i}^{b,y} & y_{test,i}^{b,z} \end{bmatrix}^\top \in \mathbb{R}^3$ .

The positions of the test data are written as

$$P_{test}^w = \begin{bmatrix} p_{test,1}^w & p_{test,2}^w & p_{test,3}^w & \cdots & p_{test,N_{test}}^w \end{bmatrix} \in \mathbb{R}^{3 \times N_{test}}, \quad (\text{B-5a})$$

where  $p_{test,i}^w = \begin{bmatrix} p_{test,i}^{w,x} & p_{test,i}^{w,y} & p_{test,i}^{w,z} \end{bmatrix}^\top \in \mathbb{R}^3$ .

The orientations of the test data are written as

$$Q_{test}^{wb} = \begin{bmatrix} q_{test,1}^{wb} & q_{test,2}^{wb} & q_{test,3}^{wb} & \cdots & q_{test,N_{test}}^{wb} \end{bmatrix}^\top \in \mathbb{R}^{4 \times N_{test}}, \quad (\text{B-6a})$$

where

$$q_{test,i}^{wb} = \begin{bmatrix} q_{test,1,i}^{wb} & q_{test,2,i}^{wb} & q_{test,3,i}^{wb} & q_{test,4,i}^{wb} \end{bmatrix}^\top \in \mathbb{R}^4. \quad (\text{B-6b})$$

In this appendix, the conditional distribution of the trained magnetic field map using a full-rank GP and a reduced-rank GP will be introduced. Moreover, the methods for the result evaluation will be shown in Section B-2. Furthermore, the results from these two methods will be compared to evaluate the parameters chosen when performing the reduced-rank GP for localization.

## B-1 Conditional distribution for evaluation

In this section, the calculation of the conditional distribution that was used when evaluating the maps trained from the full-rank and reduced-rank GP will be introduced.

### B-1-1 Full-rank GP

The measurement model with the map learned through the full-rank GP is shown in Eq. (2-19). The measurement of the orientation  $q_t^{wb}$  was assumed to be accurate. Therefore, it was not included as the test data when training the model. Instead, it was used for rotating the magnetometer measurement  $y_t^b$  for easier calculation of the gradient of the conditional Gaussian process prior. The measurement model in Eq. (2-19) rotated using the orientation can be written as

$$\begin{aligned} R_t^{wb} y_t^b &= R_t^{wb} R_t^{bw} \nabla_p \varphi(p_t^w) + R_t^{wb} e_{m,t}^b \\ &= \nabla_p \varphi(p_t^w) + e_{m,t}^w, \quad e_{m,t}^w \sim \mathcal{N}(0, R_t^{wb} (\sigma_m^2 \mathcal{I}_3) (R_t^{wb})^\top), \end{aligned} \quad (\text{B-7a})$$

where  $R_t^{wb}$  is the rotation matrix translated from the unit quaternion form of the orientation  $q_t^{wb}$ .

To evaluate the magnetic field map built using the full-rank Gaussian process, the distribution of the gradient of the scalar potential  $\nabla_p \varphi(p_t^w)$  given the training data set and the test position was calculated. That is, the conditional distribution

$$p(\nabla_p \varphi(P_{test}) | R_{train}^{wb} Y_{train}^b, P_{train}^w, P_{test}^w) = \mathcal{N}(\mu_{test}, \Sigma_{test}) \quad (\text{B-8})$$

was calculated. The means of the distribution can be obtained by calculating

$$\mu_{test} = \kappa_{FR,*}^T \kappa_{FR,y}^{-1} R_{train}^{wb} Y_{train}^b \in \mathbb{R}^{3 \times N_{test}}, \quad (\text{B-9a})$$

and the corresponding covariance matrices are

$$\Sigma_{test} = \kappa_{FR,**} - \kappa_{FR,*}^T \kappa_{FR,y}^{-1} \kappa_{FR,*} \in \mathbb{R}^{3N_{test} \times 3N_{test}}, \quad (\text{B-9b})$$

where

$$\kappa_{FR}(P_{test}^w, P_{train}^w) = \sigma_{lin}^2 \mathcal{I}_3 + \nabla_{p_{train}} \nabla_{p_{test}} \kappa_{SE}(P_{test}^w, P_{train}^w) \quad (\text{B-9c})$$

is from Eq. (2-23),  $\kappa_{FR,*} = \kappa_{FR}(P_{train}^w, P_{test}^w)$ ,  $\kappa_{FR,**} = \kappa_{FR}(P_{test}^w, P_{test}^w)$ , and  $\kappa_{FR,y} = \kappa_{FR}(P_{train}^w, P_{train}^w) + \sigma_m^2 \mathcal{I}_{N_{train}}$ , and  $R_{train}^{wb}$  are the rotation matrices translated from  $Q_{train}^{wb}$  [39].

## B-1-2 Reduced-rank Gaussian process

Similar to the full-rank GP, the measurement model shown in Eq. (2-24) is rotated to the world frame as the measurement of the orientation is assumed to be accurate and for easier calculation of the conditional Gaussian process prior. The rotated measurement model can then be written as

$$\begin{aligned} R_t^{wb} y_t^b &= R_t^{wb} R_t^{bw} \nabla_p \Phi(p_t^w) m + R_t^{wb} e_{m,t}^b \\ &= \nabla_p \Phi(p_t^w) m + e_{m,t}^w, \quad e_{m,t}^w \sim \mathcal{N}(0, R_t^{wb} (\sigma_m^2 \mathcal{I}_3) (R_t^{wb})^T). \end{aligned} \quad (\text{B-10a})$$

From Eq. (B-10a), the measurement model can be simply seen as a linear equation

$$R_t^{wb} y_t^b = \underbrace{\nabla_p \Phi(p_t^w)}_{\text{deterministic matrix}} m + e_{m,t}^w, \quad (\text{B-11})$$

where the vector  $m$  is stochastic and  $\nabla_p \Phi(p_t^w)$  is a deterministic matrix if given  $p_t^w$ . As a result, the distribution of the approximated gradient of the scalar potential  $\nabla_p \Phi(P_{test}^w) m$  can be obtained from the distribution of  $m$ .

The distribution of  $m$  is calculated from a recursive update of its mean  $\hat{m}_t$  and the covariance matrix  $\Lambda_t$  following Eq. (2-29) to (2-31) [18]. At the end of the recursive update, the distribution of  $m$  is then

$$p(m | R_{train}^{wb} Y_{train}^b, P_{train}^w) = \mathcal{N}(\hat{m}_{N_{train}}, \Lambda_{N_{train}}). \quad (\text{B-12})$$

Considering the gradient of the basis function matrix  $\nabla_p \Phi(P_{test}^w)$  is deterministic, by applying the property of joint distribution in Eq. (C-5b) [32], the conditional distribution of the gradient of the approximated potential scalar can be written as

$$\begin{aligned} & p(\nabla_p \Phi(P_{test}^w) | m | R_{train}^{wb}, Y_{train}^b, P_{train}^w, P_{test}^w) \\ &= \mathcal{N}(\mu_{test}, \Sigma_{test}) \\ &= \mathcal{N}(\nabla_p \Phi(P_{test}^w) \hat{m}_{N_{train}}, (\nabla_p \Phi(P_{test}^w)) \Lambda_{N_{train}} (\nabla_p \Phi(P_{test}^w))^T). \end{aligned} \quad (\text{B-13a})$$

## B-2 Evaluation methods

To check if the chosen parameters are appropriate, the magnetic field map built using the reduced-rank GP will be compared with the map built with the full-rank GP and the true measurement.

The data selected from the real-world measurements for the estimation of the magnetic field maps was formed with three parts of the measurements. The first two parts were the measurements gathered when walking vertically in the indoor environment. These two parts are shown in Figure B-1a and B-1b. These two measurements were gathered under a similar trajectory, but not completely the same. The last part of the measurements is a zigzag trajectory that goes from top to bottom of the plot shown in Figure B-1c.

The true magnetometer measurements were rotated to the world frame “w” before comparing with the results of the learned measurements using the reduced-rank and full-rank GP. The rotated true measurement is denoted as

$$y_{test,i}^w = R_{test,i}^{wb} y_{test,i}^b, \quad (\text{B-14})$$

where  $R_{test,i}^{wb}$  is the rotation matrix calculated from the orientation  $q_{test,i}^{wb}$  shown in Eq. (B-6b). This is done because the learned maps following the process discussed in Appendix B-1 are in the world frame “w”.

The training and test data sets applied in these evaluation methods were divided from the rotated true magnetometer measurements in a chessboard method. As shown in Figure B-2, the data points with the positions in the grey areas were selected as the training data, and the data points in the white areas were then selected as the testing data. The width of the grey blocks was set as  $0.5l_{SE}$ .

The methods for evaluating the built magnetic field maps are:

- **Standardized mean squared error (SMSE)**

The maps from the reduced-rank and full-rank GPs were evaluated using the SMSE defined in [29].

The learned measurements were evaluated in two forms of the SMSE. The first form is the norm of the rotated measurements. The SMSE of the norm of the

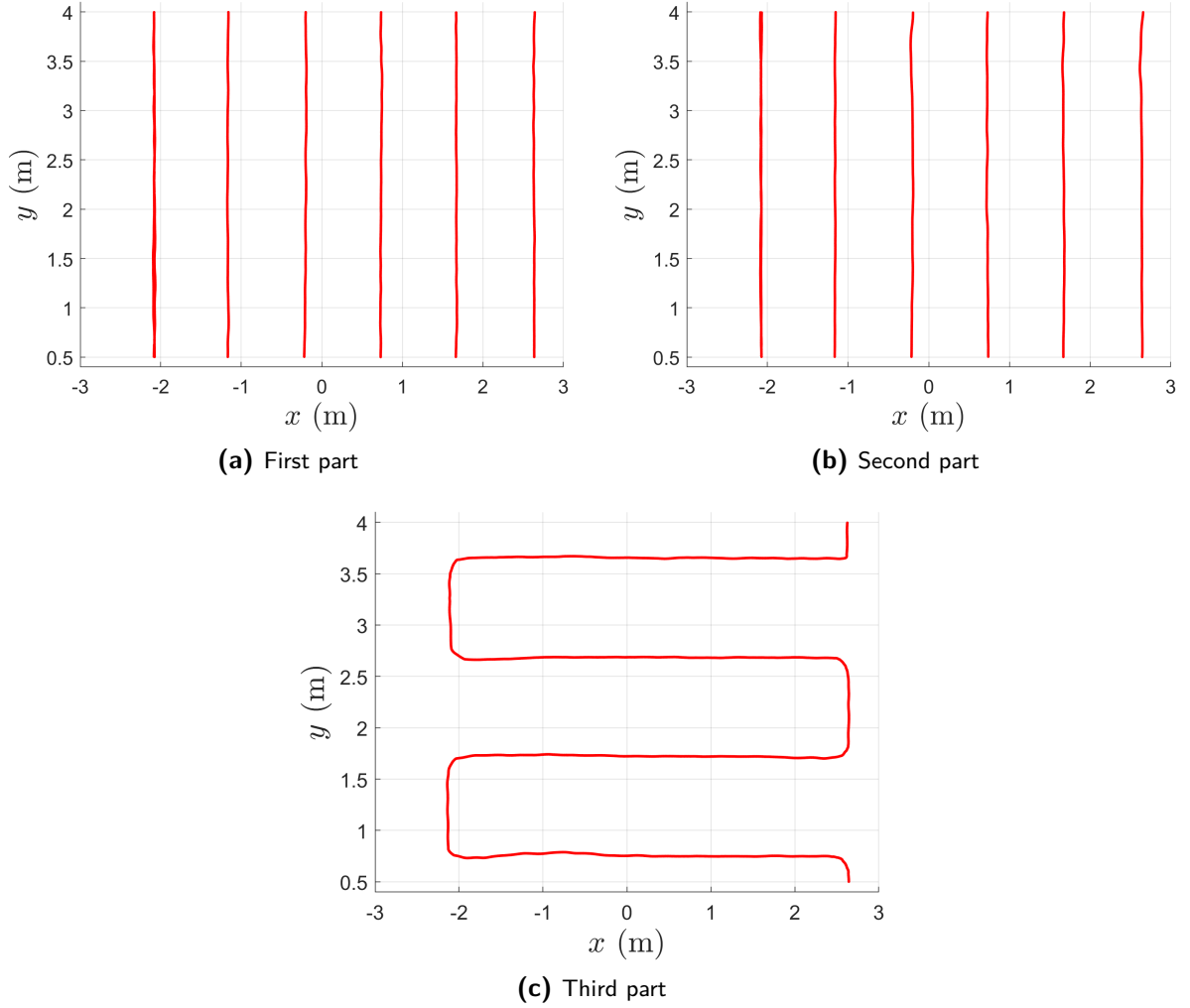


**Figure B-1:** The parts of the data from the data gathered through real-world measurement

measurements was calculated as

$$\mathbf{SMSE}_{norm} = \frac{1}{N_{test}} \sum_{i=1}^{N_{test}} \frac{(\|y_{test,i}^w\|_2 - \|\mu_{test,i}\|_2)^2}{\mathbf{Var} \left[ \begin{matrix} \|y_{train,1}^w\|_2 & \|y_{train,2}^w\|_2 & \|y_{train,3}^w\|_2 & \cdots & \|y_{train,N_{train}}^w\|_2 \end{matrix} \right]}, \quad (\text{B-15})$$

where  $\mathbf{Var}[\dots]$  is the variance of the norm of all measurements from the training data set, and  $\mu_{test,i}$  are the estimates subtracted from  $\mu_{test}$  from the reduced-rank or full-rank Gaussian process.

The second form is the vector form of the rotated measurements. The analytical

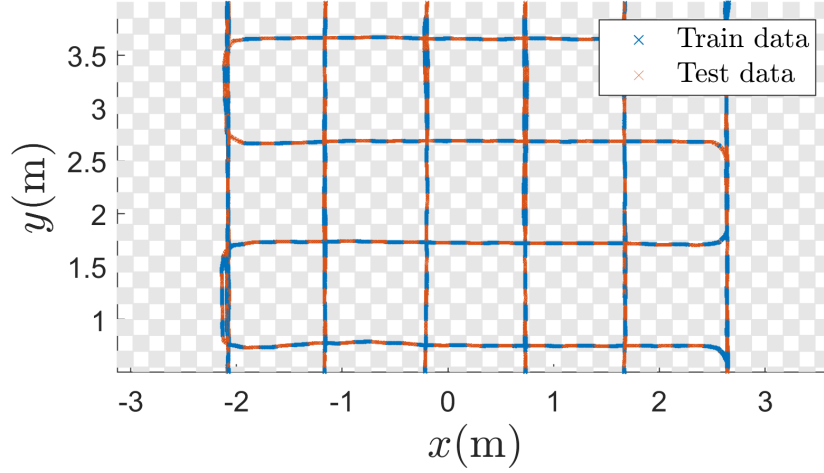


**Figure B-2:** An illustration showing how the data set is divided into a training data set and a test data set

expression of the SMSE of the measurements in the vector form can be written as

$$\text{SMSE} = \begin{bmatrix} \frac{1}{N_{test}} \sum_{i=1}^{N_{test}} \frac{(y_{test,i}^{w,x} - \mu_{test,i}^x)^2}{\text{Var} \begin{bmatrix} y_{train,1}^{w,x} & y_{train,2}^{w,x} & y_{train,3}^{w,x} & \cdots & y_{train,N_{train}}^{w,x} \end{bmatrix}} \\ \frac{1}{N_{test}} \sum_{i=1}^{N_{test}} \frac{(R_{test,i}^{wb} y_{test,i}^{w,y} - \mu_{test,i}^y)^2}{\text{Var} \begin{bmatrix} y_{train,1}^{w,y} & y_{train,2}^{w,y} & y_{train,3}^{w,y} & \cdots & y_{train,N_{train}}^{w,y} \end{bmatrix}} \\ \frac{1}{N_{test}} \sum_{i=1}^{N_{test}} \frac{(R_{test,i}^{wb} y_{test,i}^{w,z} - \mu_{test,i}^z)^2}{\text{Var} \begin{bmatrix} y_{train,1}^{w,z} & y_{train,2}^{w,z} & y_{train,3}^{w,z} & \cdots & y_{train,N_{train}}^{w,z} \end{bmatrix}} \end{bmatrix}, \quad (\text{B-16})$$

where the measurements of each axis are standardized individually.

- **Negative log predictive density (NLPD)**

The other method applied in this section for the evaluation of the learned maps is NLPD [12], and the formula for calculating the NLPD value is

$$\text{NLPD} = \frac{1}{N_{test}} \sum_{i=1}^{N_{test}} -\log(p(y_{test,i}^w; \mu_{test,i}, \Sigma_{test,i})), \quad (\text{B-17})$$

where  $\Sigma_{test,i}$  is a  $3 \times 3$  matrix subtracted from the covariance matrices  $\Sigma_{test}$  on the diagonal direction.

### B-3 Evaluation results

To find a preferred set of parameters for building the magnetic field maps using the reduced-rank GP, estimated magnetic field maps trained using the reduced-rank GP and the full-rank GP with different parameter values were compared. The parameters that were changed through this evaluation process are:

- **Range:**  
The range in  $Y$  direction of the area to localize was tested with two different values, 0.5 meters and 1.5 meters.
- **Length scale  $l_{SE}$**   
The length scale  $l_{SE}$  that is applied in Eq. (2-22) and (2-30).
- **$\sigma_{SE}$**   
The hyperparameter  $\sigma_{SE}$  that is applied in Eq. (2-22) and (2-30).
- **Data size**  
The size of the data used for the training of the magnetic field maps using the reduce-rank GP.
- **Measurement noise  $\sigma_m$**   
The guessed measurement noise  $\sigma_m$  used in Eq. (B-9c) and (2-31).

The detailed purpose of testing these parameters and the results of changing their values will be shown in the following discussion.

### Range

Increasing the number of basis functions will increase the level of the approximation of the reduced-rank GP to the full-rank GP [29], but the larger the number of basis functions is, the more computational cost is generated. Therefore, the number of the basis functions was limited to 200 in this chapter as the localization is aimed to be performed online and will be impractical if it takes too much computational effort.

Since the number of basis functions is fixed, another method to increase the level of approximation of the reduced-rank GP to the full-rank GP is to decrease the localization range. In theory, the smaller the region is, the less basis function is needed to remain at the same level of approximation as there is less complexity. Therefore, in this section, the estimated maps of different sizes of range in  $Y$  direction will be compared to see what is an appropriate range for localization. The two ranges selected to localize were 0.5 meters and 1.5 meters in  $Y$  direction. As there is a margin value set for the trajectory and the magnetic field map, the actual range selected to build the maps is 2.5 meters and 3.5 meters as shown in Figure B-3.

The SMSEs and the NLPD results are shown in Table B-1. When the range for localization is set to 0.5 meters, the reduced-rank GP is closer to the full-rank GP when looking at the SMSE values for both the norm and vector forms. However, the norm form SMSE of the full-rank GP is much higher when the range is small. The possible reason for this situation is that the range is not large enough for the GP to have enough varied information to learn the map. One might notice that the NLPD value of the reduced-rank GP is abnormal. This is now a solved issue of the reduced-rank GP and a solution will be applied in a later discussion.

Besides looking at the values of the SMSE, these range settings were also applied to the simulation of magnetic field localization. The simulation was run with 100 experiments

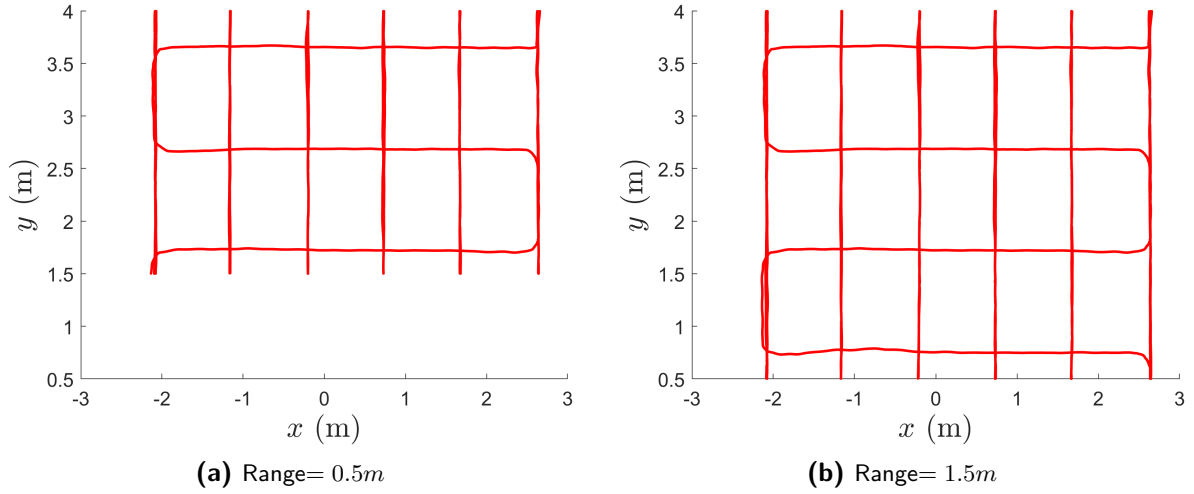


**Figure B-3:** The measurement data used for map training

<u>Range</u> (m)	$l_{SE}$	$\sigma_{SE}$	Data size	$\sigma_m$	SMSE (norm)		SMSE (vector)		NLPD	
					Reduced-rank	Full-rank	Reduced-rank	Full-rank	Reduced-rank	Full-rank
0.5	0.3	0.1	7680	0.1	0.4723	0.4052	$\begin{bmatrix} 0.5874 \\ 0.5815 \\ 0.5225 \end{bmatrix}$	$\begin{bmatrix} 0.4094 \\ 0.7044 \\ 0.1831 \end{bmatrix}$	$\infty$	14.8567
1.5	0.3	0.1	10376	0.1	0.3694	0.1371	$\begin{bmatrix} 0.6780 \\ 0.6398 \\ 0.4055 \end{bmatrix}$	$\begin{bmatrix} 0.4080 \\ 0.37612 \\ 0.1322 \end{bmatrix}$	$\infty$	13.9902

**Table B-1:** Magnetic field map evaluation results with varied ranges

for each value of the initial error and the measurement data were from the real-world magnetometer measurements with the map built using the reduced-rank GP. The detailed settings for this simulation is introduced in Section 5-3-1. From the root mean squared error (RMSE) results shown in Figure B-4, the Extended Kalman filter (EKF) is more accurate in the case when the range is smaller. The Gaussian sum filter (GSF) showed a similar level of accuracy when the number of the Gaussian components is 16 or 64 for both ranges. This can be caused by the level of the complexity of the map built through the reduced-rank GP. The maps built in the simulation can be seen in Figure B-5. It is obvious that as there are more regions included when localizing, the map is more varied, and thus the chance of multimodality will be higher. Therefore, the EKF will be less applicable to the case when the range is larger.

From the results of the norm form SMSE, it can be concluded that a larger range is better. Even though with a larger range setting the reduced-rank GP is less close to the results of the full-rank GP, the value of the SMSE of the reduced-rank GP in the norm form is smaller than the larger range case. Furthermore, the GSF is proposed as a solution when there is a multimodal distribution. Therefore, the settings for the localization range are preferred to have a larger value since a smaller range setting

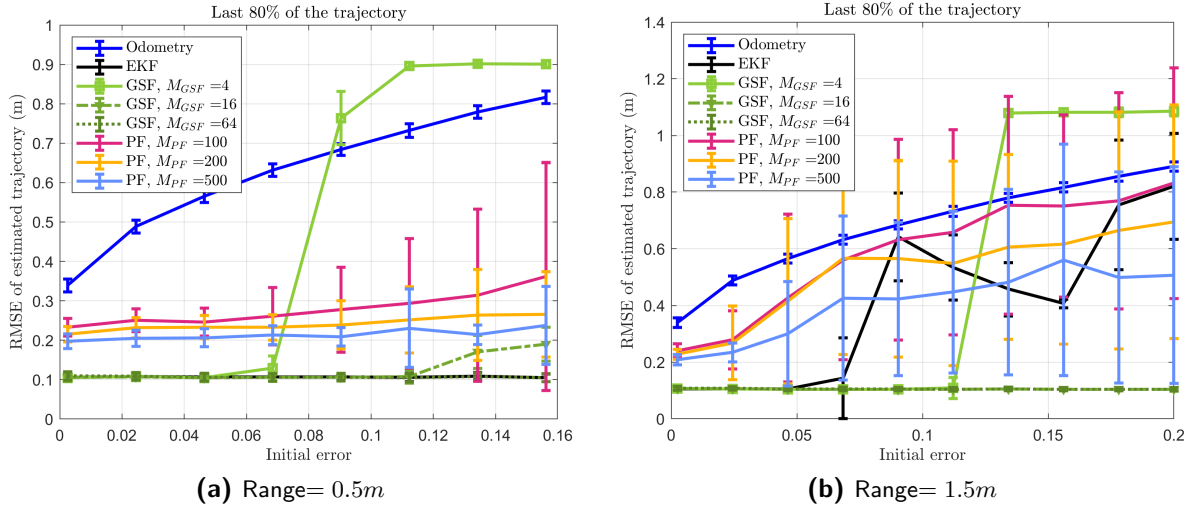


Figure B-4: The RMSE of the trajectory with different ranges for localization

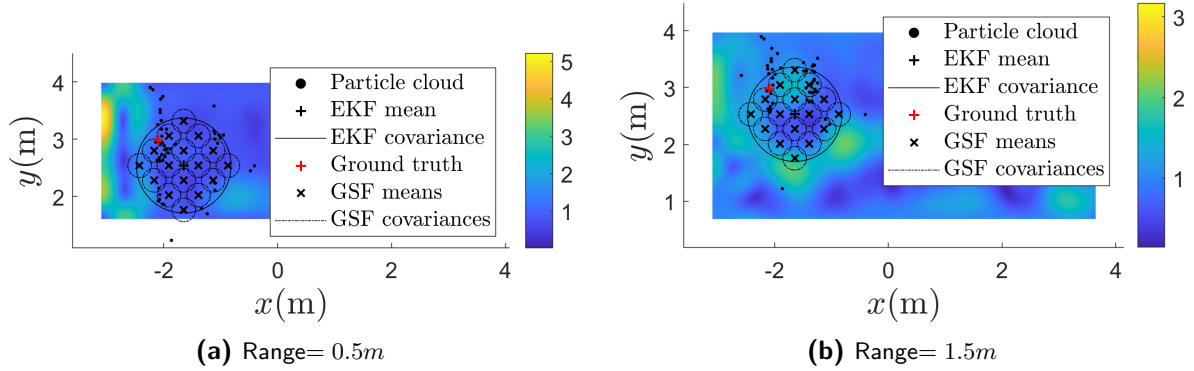


Figure B-5: The heat map of the trained magnetic field map with varied range for localization

cannot demonstrate the case that the EKF is not estimating well when the distribution is multimodal. As a result, 1.5 meters is the localization range decided after this evaluation, and this setting will be applied in later evaluations.

### B-3-1 Length scale $l_{SE}$

The length scale of the kernel for the GPs is also tested with different values and analyzed with the SMSE and NLPD.

The results are shown in Table B-2. The SMSE value in the norm form of the full-rank GP is similar when the length scale  $l_{SE}$  is set to 0.3 and 0.15, but the results of the reduce-rank GP is showing a larger value when the lengthscale  $l_{SE}$  is set to 1.5. Although the full-rank GP has better NLPD results with smaller length scale values, the setting of 0.3 for the length scale is preferred. This is because the GP that will be applied to localization is the reduced-rank GP and will be more focused. Furthermore, there is no outstanding performance of the full-rank GP when looking at the SMSE in both norm and vector form. Thus, 0.3 is the value selected for later evaluation.

Range (m)	$l_{SE}$	$\sigma_{SE}$	Data size	$\sigma_m$	SMSE (norm)		SMSE (vector)		NLPD	
					Reduced-rank	Full-rank	Reduced-rank	Full-rank	Reduced-rank	Full-rank
1.5	0.3	0.1	10376	0.1	0.3694	0.1371	0.6780 0.6398 0.4055	0.4080 0.37612 0.1322	$\infty$	13.9902
1.5	0.15	0.1	10336	0.1	0.4466	0.1379	0.6440 0.7128 0.2970	0.5621 0.2793 0.0395	$\infty$	-0.6821

**Table B-2:** Magnetic field map evaluation results with varied length scale  $l_{SE}$

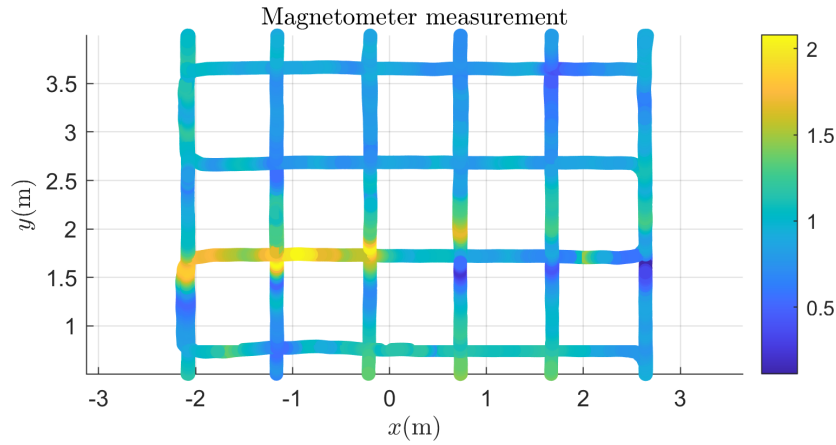


**Figure B-6:** A heat map showing the norm value of the true magnetometer measurement in different positions

### B-3-2 $\sigma_{SE}$

The hyperparameter of the squared exponential kernel  $\sigma_{SE}$  was also tried with different values to see how the performance of the learned maps would change.

The values tested were 0.1 and 1. The value “1” was chosen from observing the variance of the norm of the true magnetometer measurement. As shown in Figure B-6, the median of the measurements is around 1 and the difference between the maximum value and the medium is 1, so the value “1” was set for  $\sigma_{SE}$ . The value “0.1” was selected through random trial.

From the results shown in Table B-3, it is obvious that the map learned through the reduced-rank GP cannot converge and thus has extremely large values for the SMSEs and the error in the NLPD. As a result, “0.1” was chosen as the value to be applied in the later evaluation.

Range (m)	$l_{SE}$	$\sigma_{SE}$	Data size	$\sigma_m$	SMSE (norm)		SMSE (vector)		NLPD	
					Reduced- rank	Full- rank	Reduced- rank	Full- rank	Reduced- rank	Full- rank
1.5	0.3	0.1	10376	0.1	0.3694	0.1371	0.6780 0.6398 0.4055	0.4080 0.37612 0.1322	$\infty$	13.9902
1.5	0.3	1	10376	0.1	$2.4 \times 10^{88}$	0.6285	$1.19 \times 10^{88}$ $1.12 \times 10^{88}$ $1.55 \times 10^{87}$	0.7216 0.9595 0.0785	(error)	5.6167

**Table B-3:** Magnetic field map evaluation results with varied measurement noise  $\sigma_{SE}$

### B-3-3 Down sampling the data

As seen in previous evaluations, the NLPD values of the reduced-rank GP are infinity. This shows that the covariances of the reduced-rank GP are not appropriate. The values of the covariances were also found to be extremely small, and this will lead to infinity values when the actual difference between the estimated measurement and the true measurement is much larger than the level that the covariance matrix describes.

Although the actual reason for this phenomenon is still unknown, it is discovered that a smaller size of the training data set and a larger value of the guessed measurement noise  $\sigma_m$  might fix the problem that the estimated covariances of the reduced-rank GP is too small.

In this test, different numbers of the data size of the training data set implementing to the reduced-rank GP were tested and the results are analyzed with the values of the SMSE and the NLPD. The results are shown in Table B-4.

The value of the NLPD of the reduced-rank GP is not fixed by reducing the data size set for training the map. Furthermore, there is no obvious improvement or worsening in the SMSE results of the reduced-rank GP. Therefore, the data size applied in the later simulation will be set around 5000 for a lower computational cost.

### B-3-4 Measurement noise $\sigma_m$

As mentioned previously, the irregular NLPD value of the reduced-rank GP might be fixed by increasing the measurement noise  $\sigma_m$ . In this evaluation, two different values of  $\sigma_m$  were tested, 0.1 and 1.

The results of the SMSE and the NLPD are given in Table B-5. The NLPD value of the reduced-rank GP is now finite when  $\sigma_m$  was set to 1. Nonetheless, the norm form SMSE values are larger than the results of  $\sigma_m = 0.1$ .

As a result, the large  $\sigma_m$  value will not be adopted as the value for further simulations despite its better result in the NLPD.

One might argue that the difference is not large. Therefore, a set of simulations with the measurement noise set as 1 was also run and is shown in Appendix H. The results

Range (m)	$l_{SE}$	$\sigma_{SE}$	Data size	$\sigma_m$	SMSE (norm)		SMSE (vector)		NLPD	
					Reduced-rank	Full-rank	Reduced-rank	Full-rank	Reduced-rank	Full-rank
1.5	0.3	0.1	10376	0.1	0.3694	0.1371	0.6780 0.6398 0.4055	0.4080 0.37612 0.1322	$\infty$	13.9902
1.5	0.3	0.1	5188	0.1	0.3697	0.1371	0.6779 0.6408 0.4075	0.4080 0.37612 0.1322	$\infty$	13.9902
1.5	0.3	0.1	3459	0.1	0.3709	0.1371	0.6761 0.6401 0.4053	0.4080 0.37612 0.1322	$\infty$	13.9902
1.5	0.3	0.1	2076	0.1	0.3681	0.1371	0.6752 0.6419 0.4042	0.4080 0.37612 0.1322	$\infty$	13.9902
1.5	0.3	0.1	1153	0.1	0.3725	0.1371	0.6680 0.6450 0.4065	0.4080 0.37612 0.1322	$\infty$	13.9902
1.5	0.3	0.1	519	0.1	0.3736	0.1371	0.6608 0.6615 0.4133	0.4080 0.37612 0.1322	$\infty$	13.9902
1.5	0.3	0.1	260	0.1	0.3891	0.1371	0.6710 0.6887 0.4192	0.4080 0.37612 0.1322	$\infty$	13.9902

**Table B-4:** Magnetic field map evaluation results with varied data sizes for map estimation

Range (m)	$l_{SE}$	$\sigma_{SE}$	Data size	$\sigma_m$	SMSE (norm)		SMSE (vector)		NLPD	
					Reduced-rank	Full-rank	Reduced-rank	Full-rank	Reduced-rank	Full-rank
1.5	0.3	0.1	5188	0.1	0.3697	0.1371	0.6779 0.6408 0.4075	0.4080 0.37612 0.1322	$\infty$	13.9902
1.5	0.3	0.1	5188	1	0.4025	0.2705	0.6713 0.6595 0.4709	0.4717 0.4059 0.2707	10.7803	-0.2378

**Table B-5:** Magnetic field map evaluation results with varied measurement noise  $\sigma_m$

Range (m)	$l_{SE}$	$\sigma_{SE}$	Data size	$\sigma_m$
1.5	0.3	0.1	$\approx 5000$	0.1

**Table B-6:** Final decision of the parameters for establishing the magnetic field map using the reduce-rank GP

eventually lead to the same conclusion as the setting with the measurement noise  $\sigma_m$  set as 0.1. Therefore, it will not be included as the main discussion in this report.

### B-3-5 Final decision of the parameters

From the discussion of the range for localization, it is concluded that 1.5 meters is more suitable for the purpose of this thesis to discuss the performance of the algorithms while the distribution is multimodal. Furthermore, the values of length scale  $l_{SE}$  and hyperparameter  $\sigma_{SE}$  are set to 0.3 and 0.1 since these settings can lead to better values of SMSE in the norm form. As there's no obvious improvement in downsampling the data set used for training the map using the reduce-rank GP, the data size for training was set to half of the original dataset for a smaller computational cost than using all measurement data. For the value of the guessed measurement noise  $\sigma_m$ , as it leads to a worse SMSE norm value, it is decided not to set it to a large value just to make the NLPD results reasonable. Therefore, the final parameter settings after these evaluations are decided as shown in Table B-6.

This decision is also checked by plotting the norm of the estimated measurements and the true test data measurements in Figure B-7.

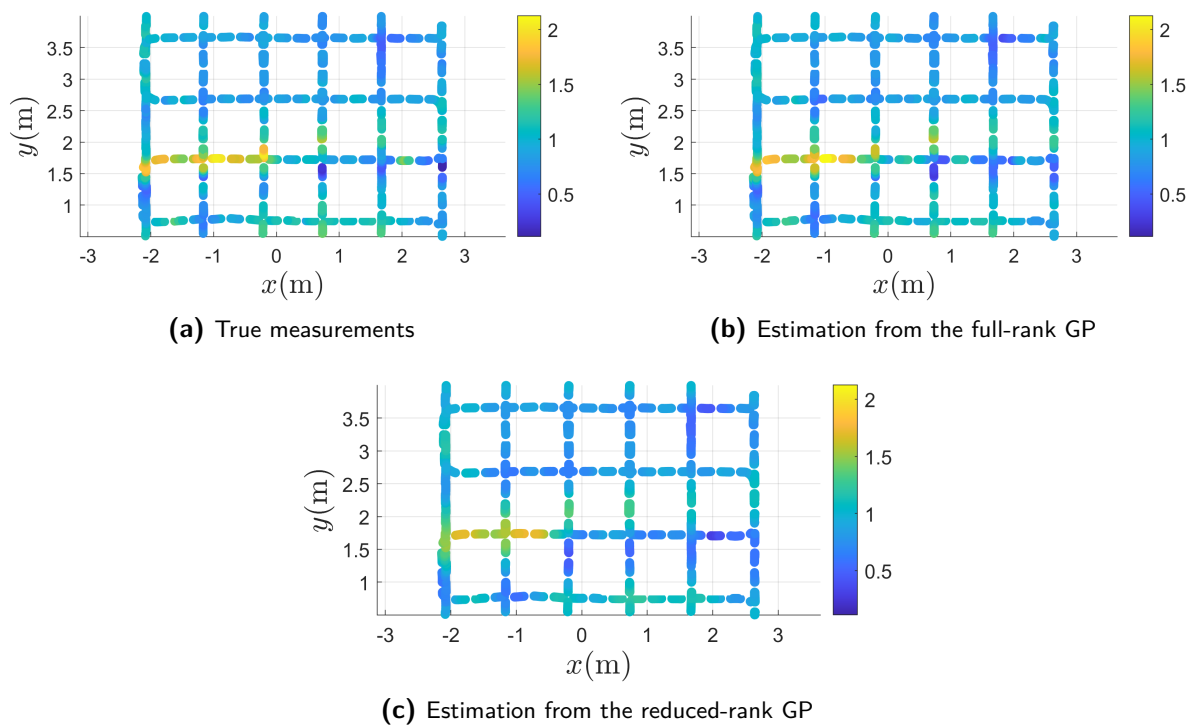


**Figure B-7:** The norm of the magnetometer measurements corresponding to their positions

# Unimodal Gaussian distribution

When considering a variable with uncertainty that has a mean and the probability density function (pdf) has a hill-like shape with the peak close to the mean, a unimodal Gaussian distribution is commonly utilized to represent its distribution. To represent a variable in  $\mathbb{R}$  with uncertainty using a Gaussian distribution, the mathematical expression of the variable can be written as

$$x \sim \mathcal{N}(\mu_x, \sigma_x^2), \quad (\text{C-1})$$

where  $x \in \mathbb{R}$  is the variable with uncertainty,  $\mu_x \in \mathbb{R}$  is the mean of the variable,  $\sigma_x^2 \in \mathbb{R}$  is the variance of the variable  $x$ , and  $\sigma_x$  is the standard deviation of the variable. Furthermore, the pdf of  $x$  can be written as

$$p(x) = \frac{1}{\sigma_x \sqrt{2\pi}} e^{-\frac{1}{2} \left( \frac{x - \mu_x}{\sigma_x} \right)^2} \quad (\text{C-2})$$

when the variable is assumed to have a Gaussian distribution [36].

Similarly, to represent the distribution of a variable in  $\mathbb{R}^n$  using a Gaussian distribution, it can be written as

$$x \sim \mathcal{N}(\mu_x, P_x), \quad (\text{C-3})$$

where  $x \in \mathbb{R}^n$  is the variable with uncertainty,  $\mu_x \in \mathbb{R}^n$  is the mean of the variable, and  $P_x \in \mathbb{R}^{n \times n}$  is the covariance of the variable  $x$ . The probability density function is then

$$p(x) = \frac{1}{\sqrt{(2\pi)^n \det(P_x)}} \exp\left(-\frac{1}{2}(x - \mu_x)^\top P_x^{-1}(x - \mu_x)\right) = \frac{1}{\sqrt{(2\pi)^n \det(P_x)}} \exp\left(-\frac{1}{2} \|(x - \mu_x)\|_{P_x^{-1}}^2\right), \quad (\text{C-4})$$

where  $\det(P_x)$  is the determinant of the matrix  $P_x$  [36].

Several theorems based on the assumption of Gaussian distribution are employed in the discussion of algorithms in Section 2-3 for position and orientation estimation. Therefore, these theorems are listed here, mostly based on the textbook [32].

## C-1 Joint distribution of Gaussian variables

When given distribution  $x \sim \mathcal{N}(\mu_x, P_x)$  and the measurement model

$$y = Cx + v, \quad v \sim \mathcal{N}(0, R), \quad (\text{C-5a})$$

the joint distribution of  $x$  and  $y$  is

$$\begin{pmatrix} x \\ y \end{pmatrix} \sim \mathcal{N} \left( \begin{pmatrix} \mu_x \\ C\mu_x \end{pmatrix}, \begin{pmatrix} P_x & P_x C^\top \\ CP_x & CP_x C^\top + R \end{pmatrix} \right) \quad (\text{C-5b})$$

[32].

## C-2 Marginal and conditional distributions of Gaussian variables

When the joint distribution of  $x$  and  $y$

$$p(x, y) = \mathcal{N} \left( \begin{pmatrix} x \\ y \end{pmatrix}; \begin{pmatrix} \mu_x \\ \mu_y \end{pmatrix}, \begin{pmatrix} P_x & P_{xy} \\ P_{yx} & P_y \end{pmatrix} \right) \quad (\text{C-6a})$$

is known, the marginal distributions of  $x$  and  $y$  are

$$x \sim \mathcal{N}(\mu_x, P_x), \quad (\text{C-6b})$$

$$y \sim \mathcal{N}(\mu_y, P_y), \quad (\text{C-6c})$$

and the conditional distributions are

$$x|y \sim \mathcal{N}(\mu_x + P_{xy}P_y^{-1}(y - \mu_y), P_x - P_{xy}P_y^{-1}P_{yx}), \quad (\text{C-6d})$$

$$y|x \sim \mathcal{N}(\mu_y + P_{yx}P_x^{-1}(x - \mu_x), P_y - P_{yx}P_x^{-1}P_{xy}) \quad (\text{C-6e})$$

[32]. This theorem is utilized when discussing the Kalman filter in Section D-1.

---

# Appendix D

---

## Extended Kalman filter

### D-1 Kalman filter (KF)

The Kalman filter (KF) was first introduced by R. E. Kalman in 1960 [13]. It estimates the state of a system by optimizing the minimum variance of the error between the reconstructed measurement values with the estimated states and the real measurement values as an observer in a system. Here, the derivation of this algorithm will be presented based on Bayesian theorems as shown in [32]. In this section, the linear model

$$x_{t+1} = Ax_t + e_{x,t}, \quad e_{x,t} \sim \mathcal{N}(0, Q), \quad (\text{D-1a})$$

$$y_t = Cx_t + e_{y,t}, \quad e_{y,t} \sim \mathcal{N}(0, R), \quad (\text{D-1b})$$

will be used to discuss the linear algorithm Kalman filter (KF), where  $x_t$  represents the state at time  $t$ ,  $A$  and  $C$  are the linear state-space matrices,  $y_t$  is the measurement signal at time  $t$ , and  $e_{x,t}$  and  $e_{y,t}$  are the zero-mean process noise and the measurement noise with the covariance denoted as

$$E \left[ \begin{bmatrix} e_{x,t} \\ e_{y,t} \end{bmatrix} \begin{bmatrix} e_{x,t}^\top & e_{y,t}^\top \end{bmatrix} \right] = \begin{bmatrix} R & S^\top \\ S & Q \end{bmatrix} \Delta(k-j) \geq 0, \quad (\text{D-2})$$

where  $R > 0$  and  $\Delta$  is the unit impulse. The covariance matrix  $S$  will be considered as a zero matrix in the following discussion since the process noise  $e_{x,t}$  and measurement noise  $e_{y,t}$  are considered to be uncorrelated.

As mentioned previously, the Kalman filter (KF) estimates the state by getting minimum error covariance. The algorithm is performed every time step with the current estimation results depending on the previous measurements and state estimations. In each time step, two main updates, the time and the measurement updates, will be carried out to result in the estimation of the state.

- **Time update**

For the time update, the state development under the model in Eq. (D-1) over time is analyzed with the states and the measurements from the previous time steps given. That is, with the density of  $x_{t-1}$  given measurements from time 1 to time  $t - 1$ , which is denoted as  $y_{1:t-1}$ , written as

$$p(x_{t-1}|y_{1:t-1}) = \mathcal{N}(x_{t-1}; \hat{x}_{t-1|t-1}, P_{t-1|t-1}), \quad (\text{D-3a})$$

and the density of  $x_t$  given  $u_t, x_{t-1}$ , and  $y_{1:t-1}$ , written as,

$$p(x_t|x_{t-1}, y_{1:t-1}) = \mathcal{N}(x_t; Ax_{t-1}, Q), \quad (\text{D-3b})$$

the density can be written as

$$\begin{aligned} p(x_t|y_{1:t-1}) &= \mathcal{N}(x_t; \hat{x}_{t|t-1}, P_{t|t-1}) \\ &= \mathcal{N}(x_t; A\hat{x}_{t-1|t-1}, AP_{t-1|t-1}A^\top + Q) \end{aligned} \quad (\text{D-4})$$

when given only the measurement  $y_{1:t-1}$ . The reader can refer to the joint and marginal distributions introduced in Section C-1 for the derivation of the distribution in Eq. (D-4).

With the results derived above, the estimation of the state and the covariance matrix at time  $t + 1$  can be written as

$$\hat{x}_{t+1|t} = A\hat{x}_{t|t}, \quad (\text{D-5a})$$

$$P_{t+1|t} = AP_{t|t}A^\top + Q \quad (\text{D-5b})$$

when given the estimated state at the previous time step  $t$ .

- **Measurement update**

After updating the estimation of the state by applying the known dynamic model matrices and the distribution of the previous states and noises, the estimation could be further calibrated by the error between the reconstructed measurements from the estimated states and the real measurements. With the relation as shown in Eq. (D-1b), the distribution of the measurement  $y_t$  is

$$p(y_t|x_t, y_{1:t-1}) = \mathcal{N}(y_t; Cx_t, R) \quad (\text{D-6})$$

when given  $x_t$  and  $y_{1:t-1}$ . Furthermore, the estimation of the state and its covariance matrix can be derived by applying the distribution D-4 and D-6 to conditional distribution mentioned in Section C-2. As a result, the estimation of the state and covariance matrix can be updated as

$$\hat{x}_{t|t} = \hat{x}_{t|t-1} + K_t(y_t - C\hat{x}_{t|t-1}), \quad (\text{D-7a})$$

$$P_{t|t} = P_{t|t-1} - K_t S_t K_t^\top, \quad (\text{D-7b})$$

where  $S_t \triangleq CP_{t|t-1}C^\top + R$  and  $K_t \triangleq P_{t|t-1}C^\top(CP_{t|t-1}C^\top + R)^{-1}$ .

## D-2 Extended Kalman filter

Due to the fact that most systems in practice are not linear, researchers adapted the KF for linear systems and designed the Extended Kalman filter (EKF) for nonlinear systems. To make the nonlinear system in the form

$$x_t = f(x_{t-1}) + e_{x,t}, \quad e_{x,t} \sim \mathcal{N}(0, Q), \quad (\text{D-8a})$$

$$y_t = h(x_t) + e_{y,t}, \quad e_{y,t} \sim \mathcal{N}(0, R) \quad (\text{D-8b})$$

applicable to the linear algebra operation that is shown in Section D-1, linearization using first-order Taylor approximation is utilized and results in the approximated system

$$x_{t+1} \cong f(\hat{x}_{t|t}) + \left. \frac{df(x_t, u_t)}{dx_t} \right|_{x_t=\hat{x}_{t|t}} (x_t - \hat{x}_{t|t}), \quad (\text{D-9a})$$

$$y_t \cong h(\hat{x}_{t|t-1}) + \left. \frac{dh(x_t)}{dx_t} \right|_{x_t=\hat{x}_{t|t-1}} (x_t - \hat{x}_{t|t-1}) \quad (\text{D-9b})$$

[1]. For notation convenience, the Jacobian matrices of the nonlinear functions  $f(\cdot)$  and  $h(\cdot)$  at the linearization point will be denoted as

$$F_t = \left. \frac{df(x_t)}{dx_t} \right|_{x_t=\hat{x}_{t|t}}, \quad (\text{D-10a})$$

$$H_t = \left. \frac{dh(x_t)}{dx_t} \right|_{x_t=\hat{x}_{t|t-1}}. \quad (\text{D-10b})$$

Similar to the KF introduced in Section D-1, the algorithm contains two updates that will be performed at each time step.

- **Measurement update**

The measurement update is similar to what is shown in Section D-1, with the measurement signal reconstructed with the function  $h(\cdot)$ , which is given as

$$\hat{x}_{t|t} = \hat{x}_{t|t-1} + K_t(y_t - h(\hat{x}_{t|t-1})), \quad (\text{D-11a})$$

and covariance matrix updated with Jacobian matrix  $H_t$ , which can be written as

$$P_{t|t} = P_{t|t-1} - K_t S_t K_t^T, \quad (\text{D-11b})$$

where  $S_t \triangleq H_t P_{t|t-1} H_t^T + R$  and  $K_t \triangleq P_{t|t-1} H_t^T S_t^{-1}$ .

- **Time update**

The time update for EKF is similar for KF, with the states updated with the dynamic function  $f(\cdot)$

$$\hat{x}_{t+1|t} = f(\hat{x}_{t|t}), \quad (\text{D-12a})$$

and the covariance updated with the Jacobian matrix  $F_t$  as

$$P_{t+1|t} = F_t P_{t|t} F_t^T + Q. \quad (\text{D-12b})$$

### D-3 Analytical expression of the general form of the EKF

The EKF mentioned in Section D-2 is shown in Algorithm 3.

---

**Algorithm 3:** Extended Kalman filter (EKF)

---

**Input:** Measurements  $\{y_t\}_{t=1}^N$ .

**Output:** Estimated states  $\{\hat{x}_{t|t}\}_{t=1}^N$ .

**Initialization:** Estimated state  $\hat{x}_{1|1}$ , and estimated covariance matrix  $P_{1|1}$ .

1 **for**  $t = 2, \dots, N$  **do**

2     Time update

$$\hat{x}_{t|t-1} = f(\hat{x}_{t-1|t-1}, u_t), \quad (\text{D-13a})$$

$$P_{t|t-1} = F_{t-1}P_{t-1|t-1}F_{t-1}^\top + Q. \quad (\text{D-13b})$$

3     Measurement update

$$\hat{x}_{t|t} = \hat{x}_{t|t-1} + K_t(y_t - h(\hat{x}_{t|t-1})), \quad (\text{D-14a})$$

$$P_{t|t} = P_{t|t-1} - K_t S_t K_t^\top, \quad (\text{D-14b})$$

$$S_t = H_t P_{t|t-1} H_t^\top + R, \quad (\text{D-14c})$$

$$K_t = P_{t|t-1} H_t^\top S_t^{-1}. \quad (\text{D-14d})$$

4 **end**

---

### D-4 Extended Kalman filter for magnetic field localization

The analytical expression of the EKF applied to magnetic field localization in Section 2-3-1 is presented in Algorithm 4.

---

**Algorithm 4:** EKF for magnetic field localization

---

**Input:** Odometry measurements  $\{\Delta p_t^w, \Delta q_t^b\}_{t=1}^N$ , magnetic field measurements  $\{y_t^b\}_{t=1}^N$ , and a magnetic field weight vector  $m$ .

**Output:** Estimated positions  $\{\hat{p}_{t|t}^w\}_{t=1}^N$  and estimated orientations  $\{\hat{q}_{t|t}^{wb}\}_{t=1}^N$ .

**Initialization:** An estimated position  $\hat{p}_{1|1}^w$ , an estimated orientation  $\hat{q}_{1|1}^{wb}$ , and an estimated covariance matrix  $P_{1|1}$ .

```

1 for  $t = 2, \dots, N$  do
2   for  $i = 1 : M_{GSF}$  do
3     Time update


$$\hat{p}_{t|t-1}^w = \hat{p}_{t-1|t-1}^w + \Delta p_t^w, \tag{D-15a}$$


$$\hat{q}_{t|t-1}^{wb} = \hat{q}_{t-1|t-1}^{wb} \odot \exp_{\mathbf{q}}(\Delta q_t^b), \tag{D-15b}$$


$$P_{t|t-1} = P_{t-1|t-1} + Q_{\zeta}. \tag{D-15c}$$


4     Measurement update


$$\hat{\zeta}_t = K_t(\hat{R}_{t|t-1}^{wb} y_t^b - \nabla \Phi(\hat{p}_{t|t-1}^w) m), \tag{D-16a}$$


$$P_{t|t} = P_{t|t-1} - K_t S_t K_t^T, \tag{D-16b}$$


$$S_t = H_t P_{t|t-1} H_t^T + \sigma_m^2 \mathcal{I}_3, \tag{D-16c}$$


$$K_t = P_{t|t-1} H_t^T S_t^{-1}. \tag{D-16d}$$


5     Linearized point correction


$$\hat{p}_{t|t}^w = \hat{p}_{t|t-1}^w + \hat{\delta}_t^w, \tag{D-17a}$$


$$\hat{q}_{t|t}^{wb} = \exp_{\mathbf{q}}(\hat{\eta}_t^w) \odot \hat{q}_{t|t-1}^{wb}. \tag{D-17b}$$


6   end
7 end

```

---



---

# Appendix E

---

## Particle filter

Similar to the Extended Kalman filter (EKF), the Particle filter (PF) is also known as a widely applied algorithm capable of estimating states of nonlinear systems [34, 2, 15]. Instead of linearizing the system and applying the linear algebra based on the assumption that the distributions are Gaussian, which is what the EKF does, the PF approximates the distribution of the state with particles whose corresponding weights are updated through iteration [9]. A PF approximates the posterior distribution at time  $t$  with a set of  $M_{PF}$  samples  $\{x_t^i\}_{i=1}^{M_{PF}}$ , which is called the particles when discussing a PF. Before the start of the iteration of the algorithm, an initialization of the particles is performed. That is,  $M_{PF}$   $x_1$  particles with a initial distribution  $p_{x_1}$  will be introduced and the weights of these particles are equally assigned, which can be mathematically denoted as  $x_1^i \sim p_{x_1}$  and  $w_{1|0}^i = 1/M_{PF}$  for all  $i \in \{1, 2, \dots, M_{PF}\}$ . For each time step, there will be  $M_{PF}$  measurement updates, one for each particle  $x_t^i$ . Following the measurement updates are the estimation, resampling, and  $M_{PF}$  time updates [9].

- **Measurement update**

For  $i \in \{1, 2, \dots, M_{PF}\}$ , the weight will be updated by

$$w_{t|t}^i = \frac{w_{t|t-1}^i p(y_t | x_t^i)}{\sum_{j=1}^N w_{t|t-1}^j p(y_t | x_t^j)}. \quad (\text{E-1})$$

- **Estimation**

After the weights are updated, the estimation of the mean can be determined by the resulting particle clouds and the corresponding weights.

- **Resampling**

The particle cloud  $\{x_{1:t}^i\}_{i=1}^{M_{PF}}$  is updated depending on the corresponding weights. That is, the particles with lower weights will have a higher chance of being replaced

by the particles with higher weights. After the update of the particle cloud, the weights are then reset to  $w_{t|t}^i = 1/M_{PF}$ . Note that this step is optional because resampling means dropping information, which might further introduce more uncertainty [9].

- **Time update**

Similar to measurement update, the time update is also run  $M_{PF}$  times with the distribution of  $x_{t+1}^i$  updated as

$$x_{t+1}^i \sim \pi(x_{t+1}|x_t^i, y_{t+1}), \quad (\text{E-2a})$$

where  $\pi(x_{t+1}|x_t^i, y_{t+1})$  represents the proposal distribution (also called importance distribution in [30]), and the weight is further updated depending on this distribution as

$$w_{t+1|t}^i = w_{t|t}^i \frac{p(x_t^i|x_{t-1}^i)}{\pi(x_t^i|x_{t-1}^i, y_t)}. \quad (\text{E-2b})$$

The choice of proposal distribution  $\pi(x_{t+1}|x_t^i, y_{t+1})$  depends on the property that is preferred. A list of different proposal distributions and their characteristics can be found in Section 9.5 in [9].

The updates of the weights in the time and measurement updates are sometimes combined in the same loop. By taking Eq. (E-1) into Eq. (E-2b), the update of the weights can be simplified to

$$w_{t|t}^i \propto w_{t-1|t-1}^i \frac{p(y_t|x_t^i)p(x_t^i|x_{t-1}^i)}{\pi(x_t^i|x_{t-1}^i, y_t)}. \quad (\text{E-3})$$

The analytical expression for the general form of the PF is given in Algorithm 5.

The PF adjusted for magnetic field localization is shown in Algorithm 6.

---

**Algorithm 5:** Particle filter (PF) with the prior distribution as the proposal distribution

---

**Input:** Measurements  $\{y_t\}_{t=1}^N$ .

**Output:** Estimated states  $\{\hat{x}_t\}_{t=1}^N$ .

**Initialization:** Weights  $w_1^i = \frac{1}{M_{PF}}$  and a particle cloud  $\hat{x}_1^i \sim \mathcal{N}(\hat{x}_1, P_1)$  for all  $i \in \{1, \dots, M_{PF}\}$ .

```

1 for  $t = 2, \dots, N$  do
2   for  $i = 1 : M_{PF}$  do
3     Time update
4
5         
$$\hat{x}_t^i = f(\hat{x}_{t-1}^i) + e_{x,t} \tag{E-4a}$$

6
7     Measurement update
8
9         
$$w_t^i = w_{t-1}^i p(y_t; h(\hat{x}_t^i), R). \tag{E-5a}$$

10
11     Resampling
12     Select a new set of particles from the current particle set to build a new particle
13     cloud. The chance of the particles being selected depends on their weights.
14     Particles could be selected repeatedly.
15   end
16   Estimation
17   The trajectory of the particle with the largest weight will be taken as the output.
18 end

```

---

---

**Algorithm 6:** PF for magnetic field localization
 

---

**Input:** Odometry measurements  $\{\Delta p_t^w, \Delta q_t^b\}_{t=1}^N$ , magnetic field measurements  $\{y_t^b\}_{t=1}^N$ , and a magnetic field weight vector  $m$ .

**Output:** Estimated positions  $\{\hat{p}_t^w\}_{t=1}^N$  and estimated orientations  $\{\hat{q}_t^{wb}\}_{t=1}^N$ .

**Initialization:** Weights  $w_1^i = \frac{1}{M_{PF}}$ , a position particle cloud  $\hat{p}_1^{w,i} \sim \mathcal{N}(\hat{p}_1^w, P_1)$ , and an orientation particle cloud  $\hat{q}_1^{wb,i} = q_1^{wb}$  for  $i \in \{1, \dots, M_{PF}\}$ .

```

1 for  $t = 2, \dots, N$  do
2   for  $i = 1 : M_{PF}$  do
3     Time update

$$\hat{p}_t^{w,i} = \hat{p}_{t-1}^{w,i} + \Delta p_{t-1} + e_{p,t}^w, \quad (\text{E-6a})$$


$$\hat{q}_t^{wb,i} = \hat{q}_{t-1}^{wb,i} \odot \exp_q(\Delta q_{t-1}^b + e_{p,t}^b). \quad (\text{E-6b})$$

4     Measurement update

$$w_t^i = w_{t-1}^i p(R_t^{wb,i} y_t^b; f, \sigma_m^2 \mathcal{I}_3), \quad (\text{E-7a})$$


$$f = \nabla \Phi(\hat{p}_t^{w,i}) m. \quad (\text{E-7b})$$

5     Resampling
      Select a new set of particles from the current particle set to build a new particle
      cloud. The chance of the particles being selected depends on their weights.
      Particles could be selected repeatedly.
6   end
7   Estimation
      The trajectory of the particle with the largest weight will be taken as the output.
8 end

```

---

---

## Appendix F

---

### Gaussian sum filter

In this chapter, the process of how the diamond shape Gaussian sum filter (GSF) was designed in this thesis will be introduced.

The GSF was designed to have the means and the 68% confidence ellipsoids approximate the 68% confidence ellipsoid of the Extended Kalman filter (EKF). First, a square was formed with the sides calculated from the covariance value of the EKF. That is, the side of the square that was parallel to the  $X$  direction had a length of  $2\sqrt{P_{1|1,(x,x)}}$  and the side parallel to the  $Y$  direction had a length of  $2\sqrt{P_{1|1,(y,y)}}$ . The position of the center of this square was designed to be the mean of the EKF as introduced in Section 4-1-3. Thus, the means of the Gaussian components would be

$$\hat{p}_{x,1|1}^{w,i} \in [\hat{p}_{x,1|1}^w - \sqrt{P_{1|1,(x,x)}}, \hat{p}_{x,1|1}^w + \sqrt{P_{1|1,(x,x)}}], \quad (\text{F-1a})$$

and

$$\hat{p}_{y,1|1}^{w,i} \in [\hat{p}_{y,1|1}^w - \sqrt{P_{1|1,(y,y)}}, \hat{p}_{y,1|1}^w + \sqrt{P_{1|1,(y,y)}}], \quad (\text{F-1b})$$

where  $\hat{p}_{x,1|1}^w$  and  $\hat{p}_{y,1|1}^w$  are the estimated position on  $X$  and  $Y$  axes of the EKF, and  $P_{1|1,(x,x)}$  and  $P_{1|1,(y,y)}$  are the variances of the  $X$  and  $Y$  position of the EKF.

However, in the simulations of magnetic field localization, the initial estimated position of the EKF was often introduced in a diagonal or opposite diagonal direction from the ground truth, and this increases the chance of the ground truth to overlap with one of the mean of the Gaussian components. To avoid such coincidence as the possible reason for the good performance of the GSF, the area the Gaussian components were scattered in is rotated  $\frac{\pi}{4}$  counterclockwise and turned into a diamond shape. The resulting means of the Gaussian components will then be

$$\begin{bmatrix} \hat{p}_{x,1|1}^{w,i} \\ \hat{p}_{y,1|1}^{w,i} \end{bmatrix} = R \begin{bmatrix} \delta \hat{p}_{x,1|1}^{w,i} \\ \delta \hat{p}_{y,1|1}^{w,i} \end{bmatrix} + \begin{bmatrix} \hat{p}_{x,1|1}^w \\ \hat{p}_{y,1|1}^w \end{bmatrix}, \quad (\text{F-2a})$$

where

$$\delta \hat{p}_{x,1|1}^{w,i} \in [-\sqrt{P_{1|1,(x,x)}}, \sqrt{P_{1|1,(x,x)}}], \quad (\text{F-2b})$$

$$\delta \hat{p}_{y,1|1}^{w,i} \in [-\sqrt{P_{1|1,(y,y)}}, \sqrt{P_{1|1,(y,y)}}], \quad (\text{F-2c})$$

$$R = \begin{bmatrix} \cos(0.25\pi) & -\sin(0.25\pi) \\ \sin(0.25\pi) & \cos(0.25\pi) \end{bmatrix}. \quad (\text{F-2d})$$

An illustration of the difference before and after the rotation is shown in Figure F-1. In Figure F-1a, the ground truth is close to the mean of a Gaussian component that is placed on the down-left corner of the square. On the other hand, the ground truth shown in Figure F-1b is further away from the means of the Gaussian components with the design of the diamond shape. Therefore, it is obvious that the design with a diamond shape will avoid the overlapping of the ground truth and the mean of a Gaussian component as long as the number of the Gaussian component on each side is kept even.

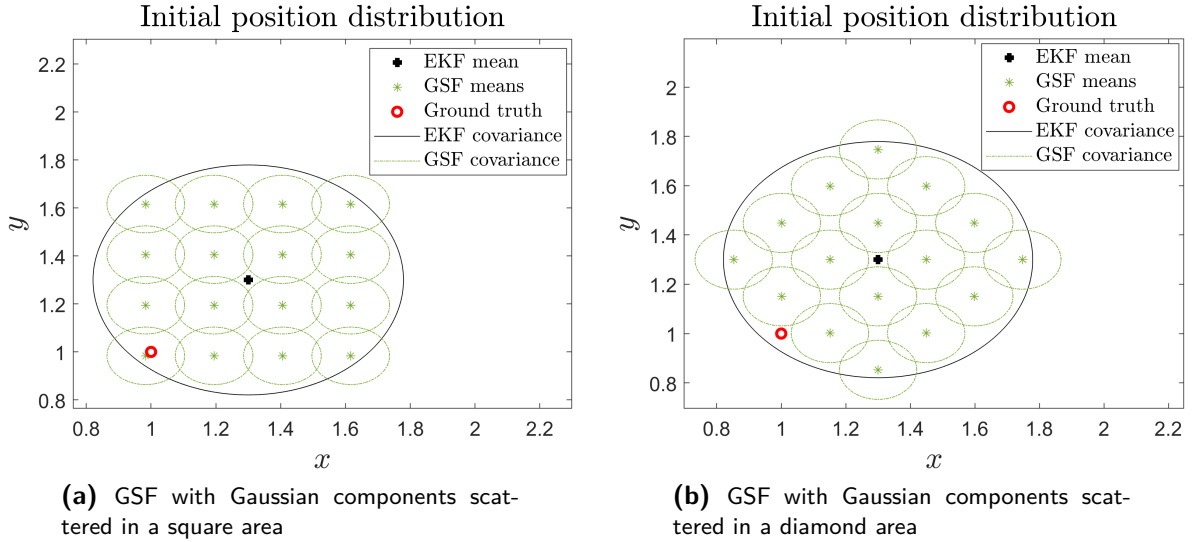


**Figure F-1:** An example of the GSF with different shapes designed for the initial arrangement of the Gaussian components

# Analysis of the performance of the Gaussian sum filter (GSF) in Section 4-2-3 and 5-3-3

## G-1 Results from Section 4-2-3

In Section 4-2-3, it is shown that the accuracy of the GSF was not influenced by the large initial covariance value. This is not an expected result as the Extended Kalman filter (EKF) core of the GSF might not work properly when there are large covariance values [1, 33, 24].

To find out the possible reason for this phenomenon, the weights, covariances, and the root mean squared error (RMSE) of the trajectories of the Gaussian components of the GSF that were initially placed in the position closest to the ground truth were analyzed. The indices of the four Gaussian components that were placed close to the ground truth when initializing the GSF are shown in Figure G-1. The weights, covariance matrices, and the RMSE of the trajectories of the Gaussian components with index  $i \in \{2, 3, 6, 7\}$  were analyzed, which are the four Gaussian components placed nearest to the ground truth in the initialization.

The average weights of these four Gaussian components that developed through time are plotted in Figure G-2. Since there were 100 experiments run for each value of the parameter  $P_{1|1,(x,x)}^i$ , the weight value shown is the average of the 100 results. The weights of each value of the parameter  $P_{1|1,(x,x)}^i$  are plotted in separate lines. From the figure, there is no Gaussian component that has consistently dominating weights throughout the entire simulation. This indicates the good performance of the GSF is not mainly due to the existence of the Gaussian components that were set close to the ground truth when initializing the GSF.

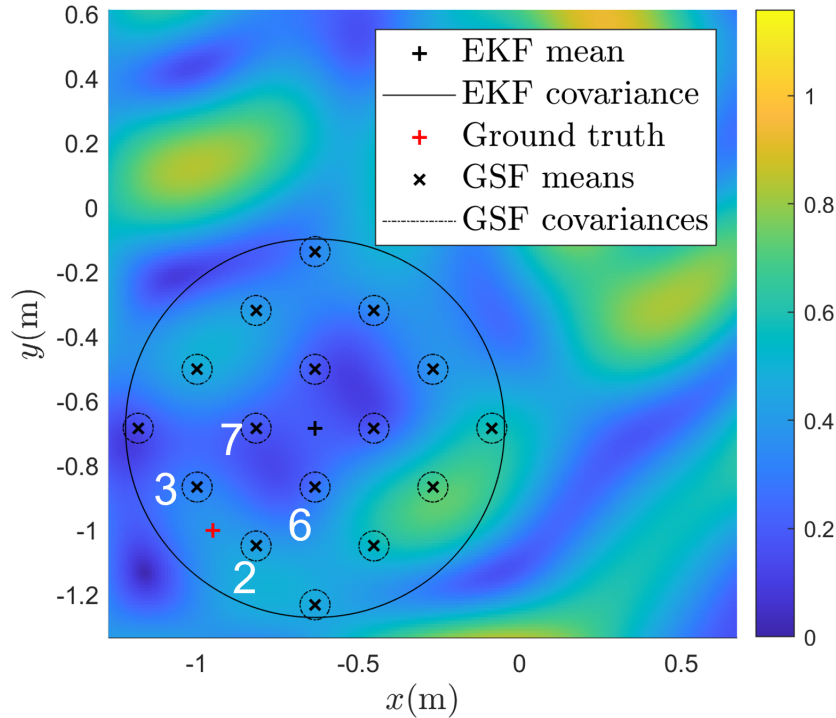


**Figure G-1:** The indices of the 4 Gaussian components which were initially closest to the ground truth (marked with white numbers)

Besides the weights of the four closest Gaussian components, their RMSE of the trajectories were also checked. The RMSE of the four Gaussian components are shown in Figure G-3. As the RMSE does not vary with the different ranges of the trajectories, it indicates that the inaccuracy is not due to the relatively unstable time when the localization just started. As the four Gaussian components all have large RMSE compared to the GSF, it is again confirmed that the four initially closest Gaussian components did not dominate the estimation results of the GSF.

Moreover, the covariances of the four Gaussian components were analyzed by checking their maximum eigenvalues through the simulation time. In Figure G-4, the maximum eigenvalues of covariance matrices are plotted for the Gaussian components that were initially placed close to the ground truth for each value of the initial covariances. The eigenvalues of all Gaussian components dropped rapidly in the first few time steps, and this can be a reasonable cause why the RMSE of the estimation of the GSF is not significantly influenced by the values of the initial covariance matrices. The possible reason for this sudden drop is the small measurement noise  $\sigma_m$  set for the GSF. When the covariance of the measurement noise is small, the covariance of the states will be set to small values in the measurement update.

However, it is worth noticing that the maximum eigenvalues of the Gaussian components' covariance matrices grow slightly through time as shown in Figure G-5. This is a sign that as the localization duration increases, the higher risk there are the covariances of the Gaussian components grow too large for the GSF to estimate accurately. Therefore, for a longer period of localization, a strategy to decompose Gaussian components

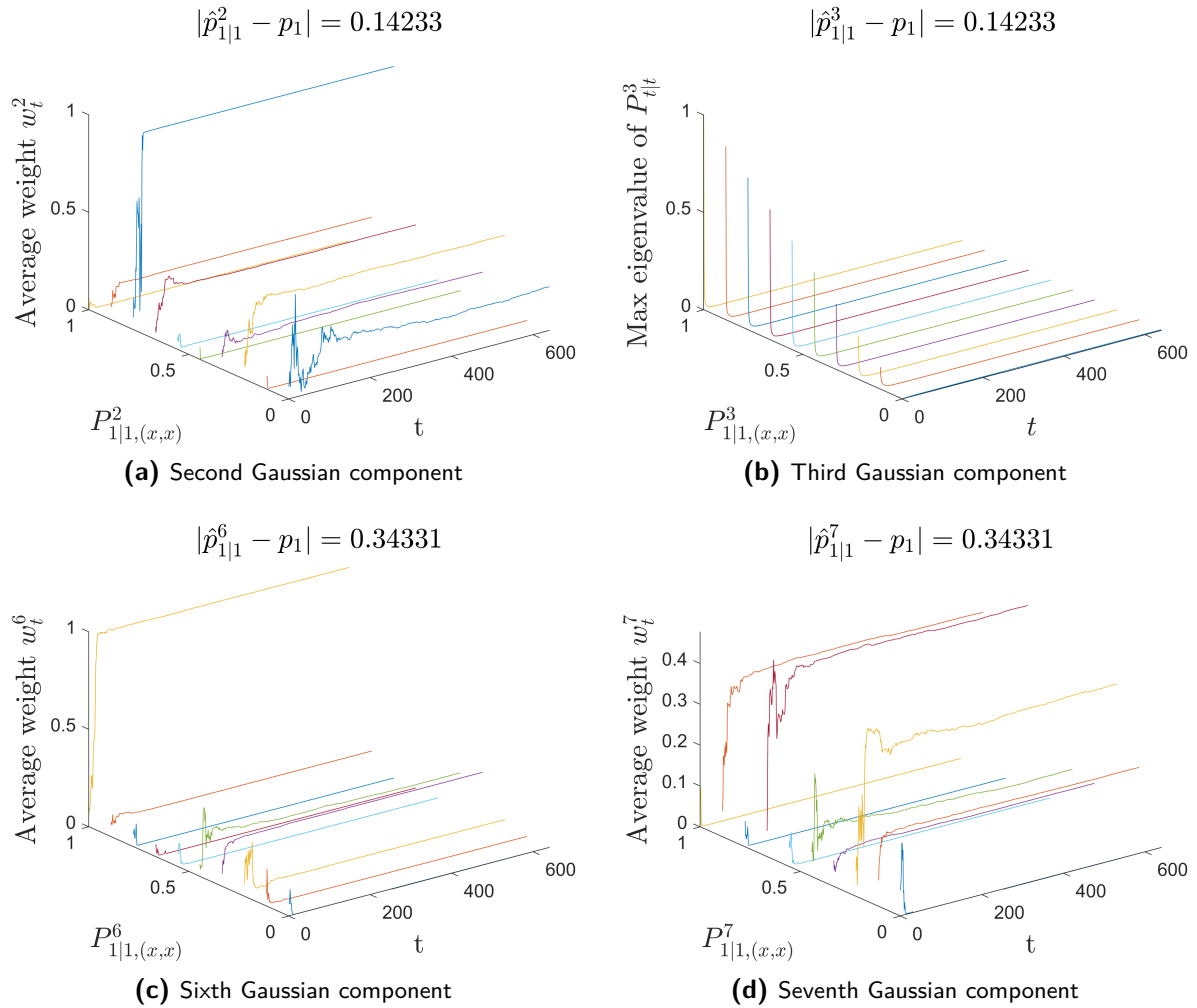


**Figure G-2:** The weights change through time for different initial covariance values of the Gaussian components of the GSF

with large covariance values will be needed.

## G-2 Results from Section 5-3-3

Same as what was done in the purely simulated system in Appendix G-1, an analysis of the Gaussian components by observing the weights, covariance values, and the RMSE through the simulation was conducted. This analysis was carried out to see what is the possible reason that the GSF is performing well even with large covariance values set initially.

The GSF with 16 Gaussian components is selected for this analysis and the results of the 4 Gaussian components that were initially placed in the position closest to the ground truth will be presented for discussion. The indices of these four Gaussian components and their position in  $X - Y$  plane are shown in Figure G-6.

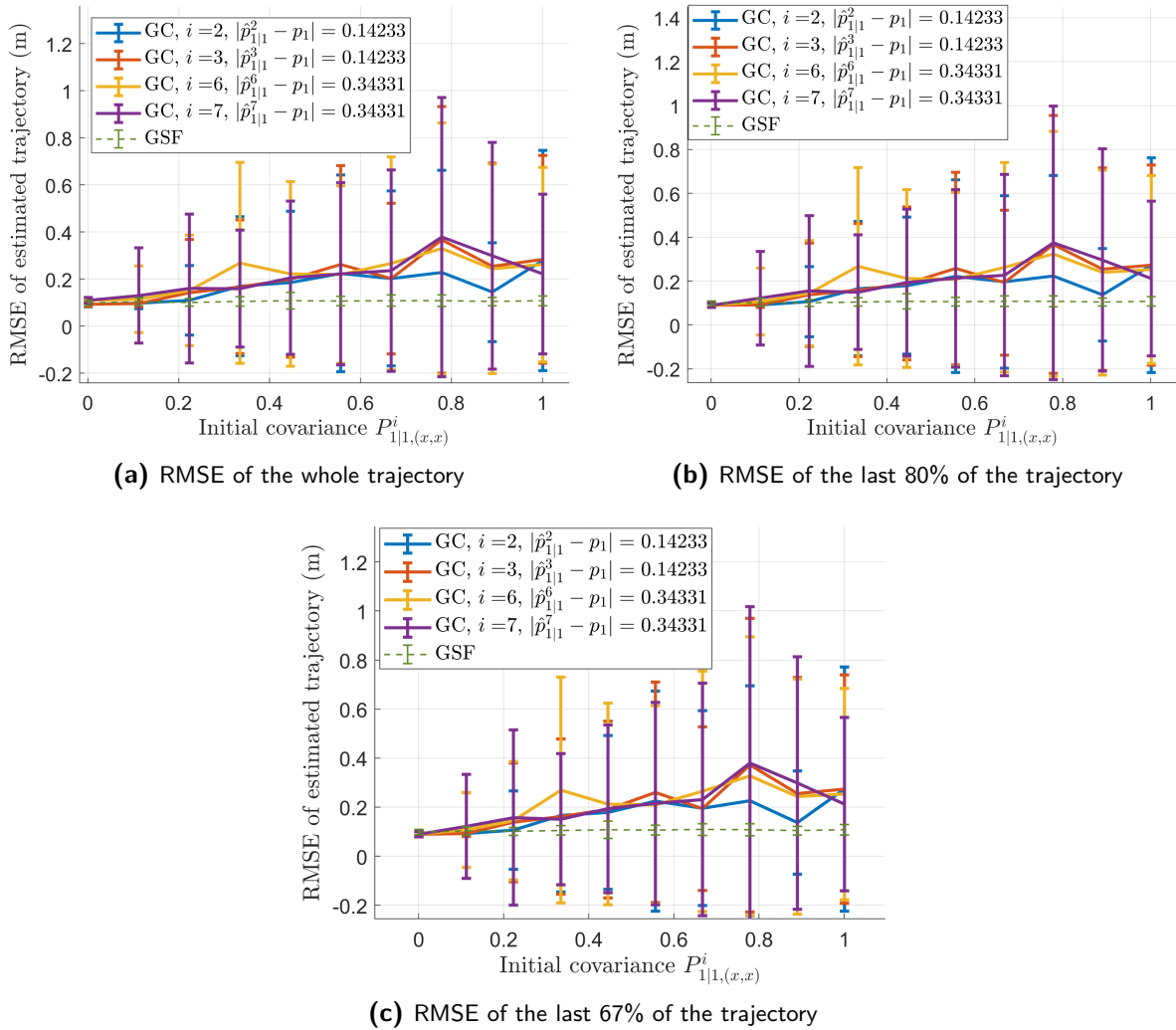


**Figure G-3:** The RMSE of the Gaussian components of the GSF that were initially closest to the ground truth

In Figure G-7, the results of the weights developed through time show that the Gaussian components that were set closest to the ground truth are not dominating the estimations and leading to good results. Furthermore, from the RMSE of each Gaussian component shown in Figure G-8, it is obvious that not only one Gaussian component is converging to the final estimated results of the GSF. This indicates that it is reasonable that the accuracy of the GSF is good even when the closest Gaussian components were not weighting the most.

Although the results in this simulation show that there is no need to implement a decomposing strategy to avoid large covariance values while localizing in this thesis project, such a decomposing strategy might be necessary in practice. As shown in Figure G-9, the maximum eigenvalues grow as time increases. This indicates that as the localizing time is long enough, the covariance values may grow too large for the GSF to estimate well.

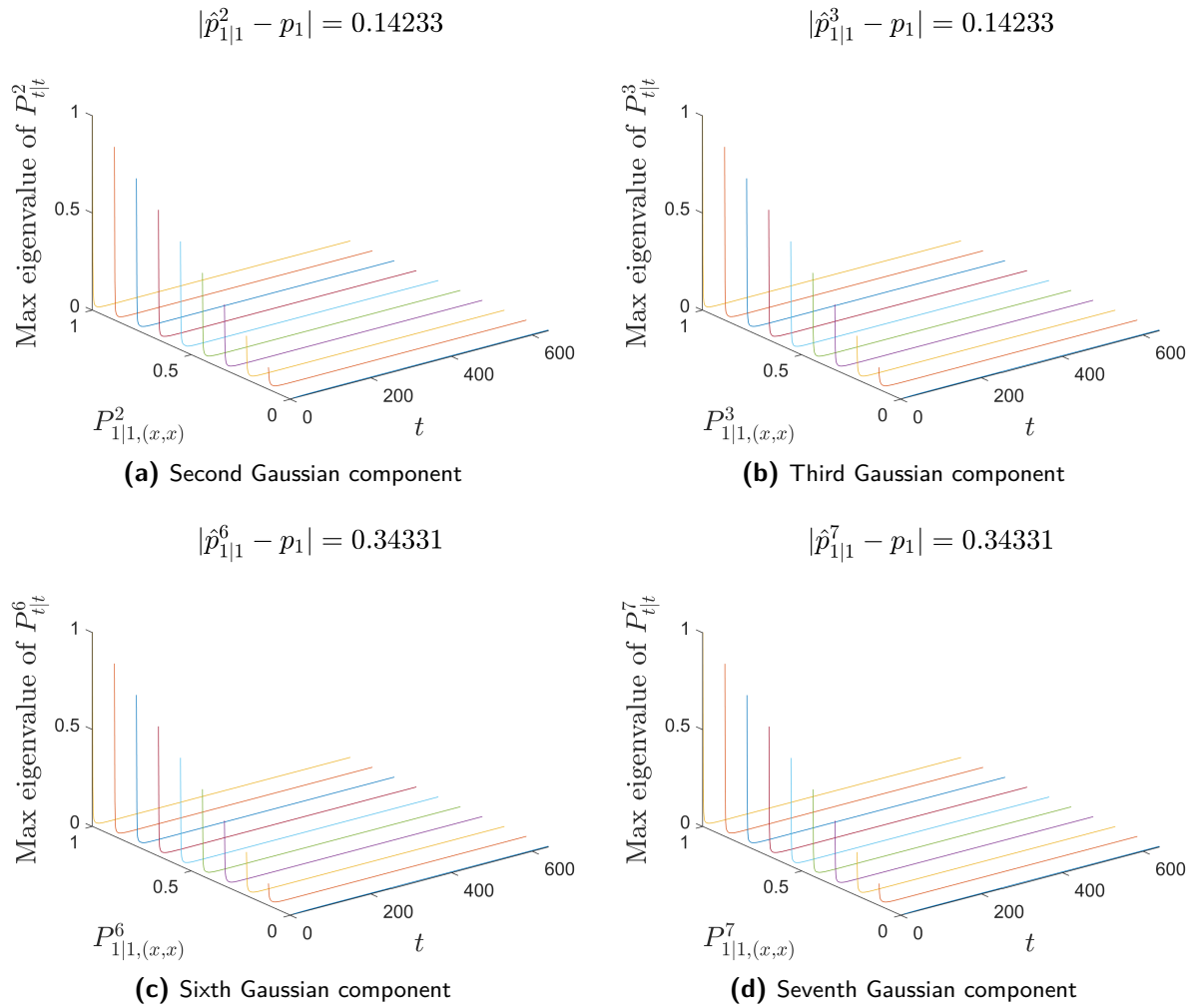


**Figure G-4:** The max eigenvalues of the covariance matrices change through time for different initial covariance values of the Gaussian components of the GSF

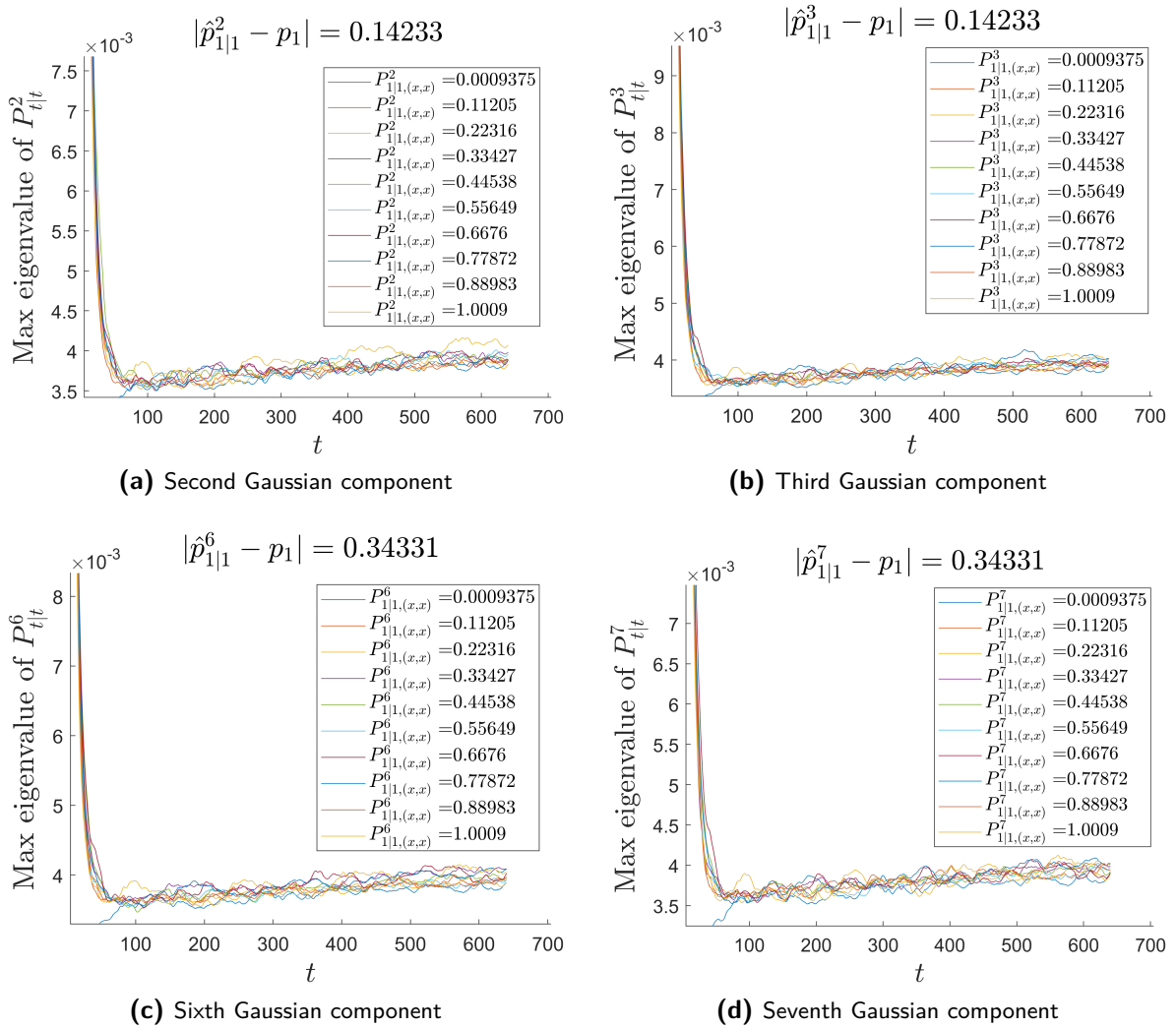


**Figure G-5:** The max eigenvalues of the covariance matrices change through time for different initial covariance values of the Gaussian components of the GSF (enlarged two-dimensional plots of the figures shown in Figure G-4)

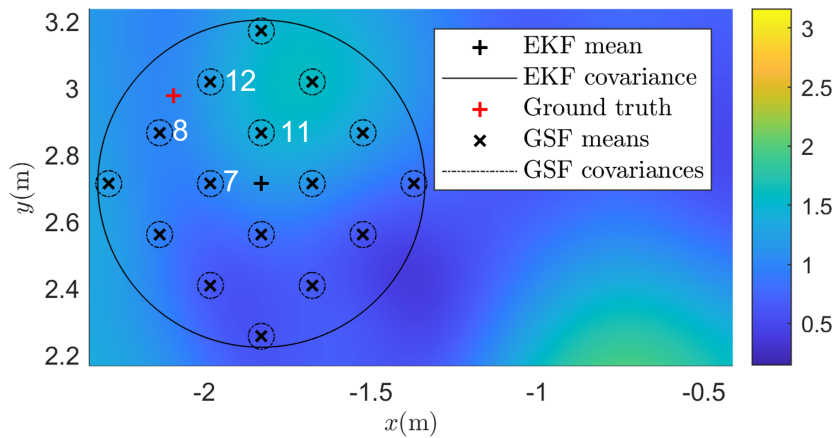


**Figure G-6:** The indices of the 4 initially closest Gaussian components and the ground truth

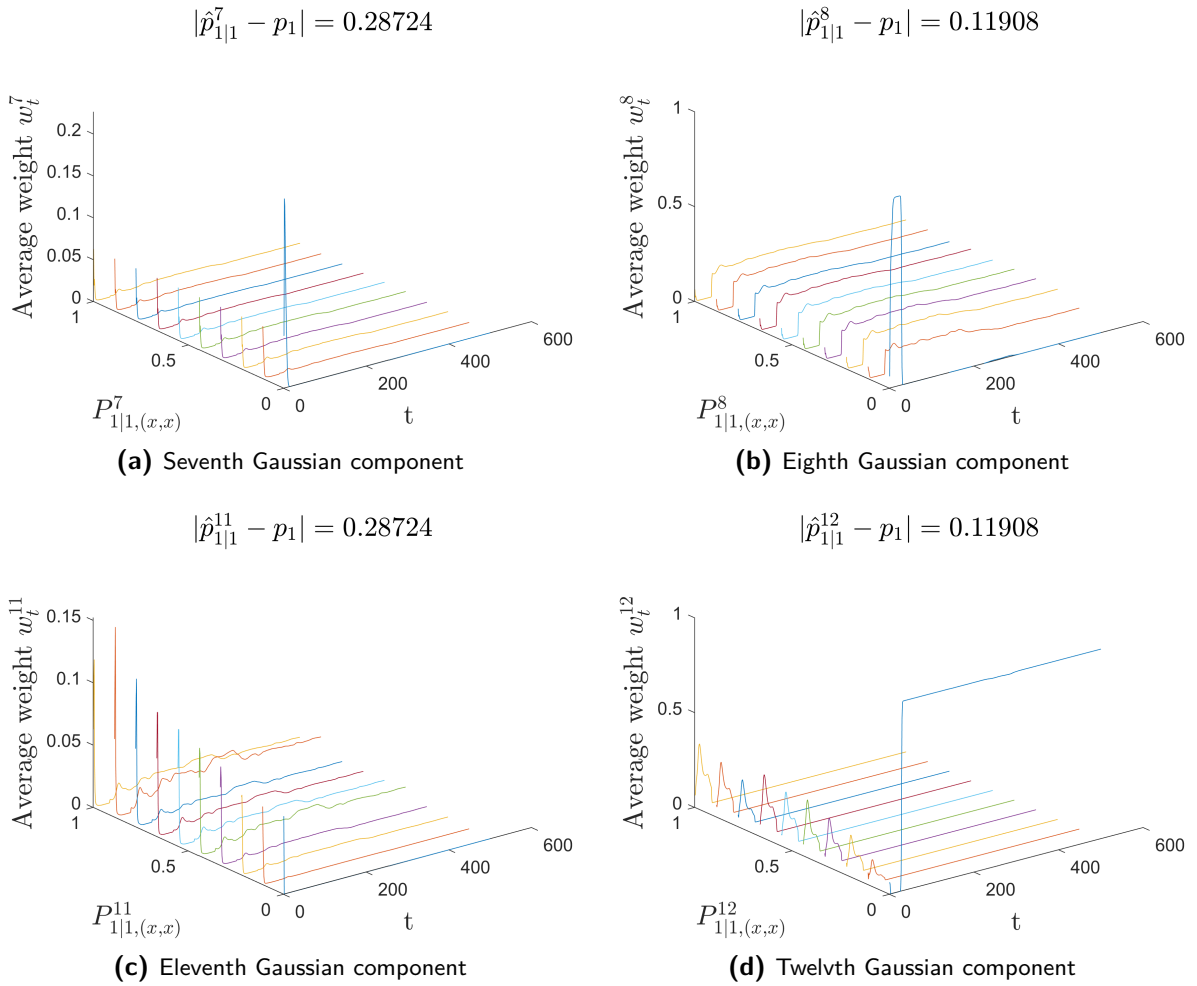


**Figure G-7:** The weights change through time for different initial covariance values of the Gaussian components of the GSF

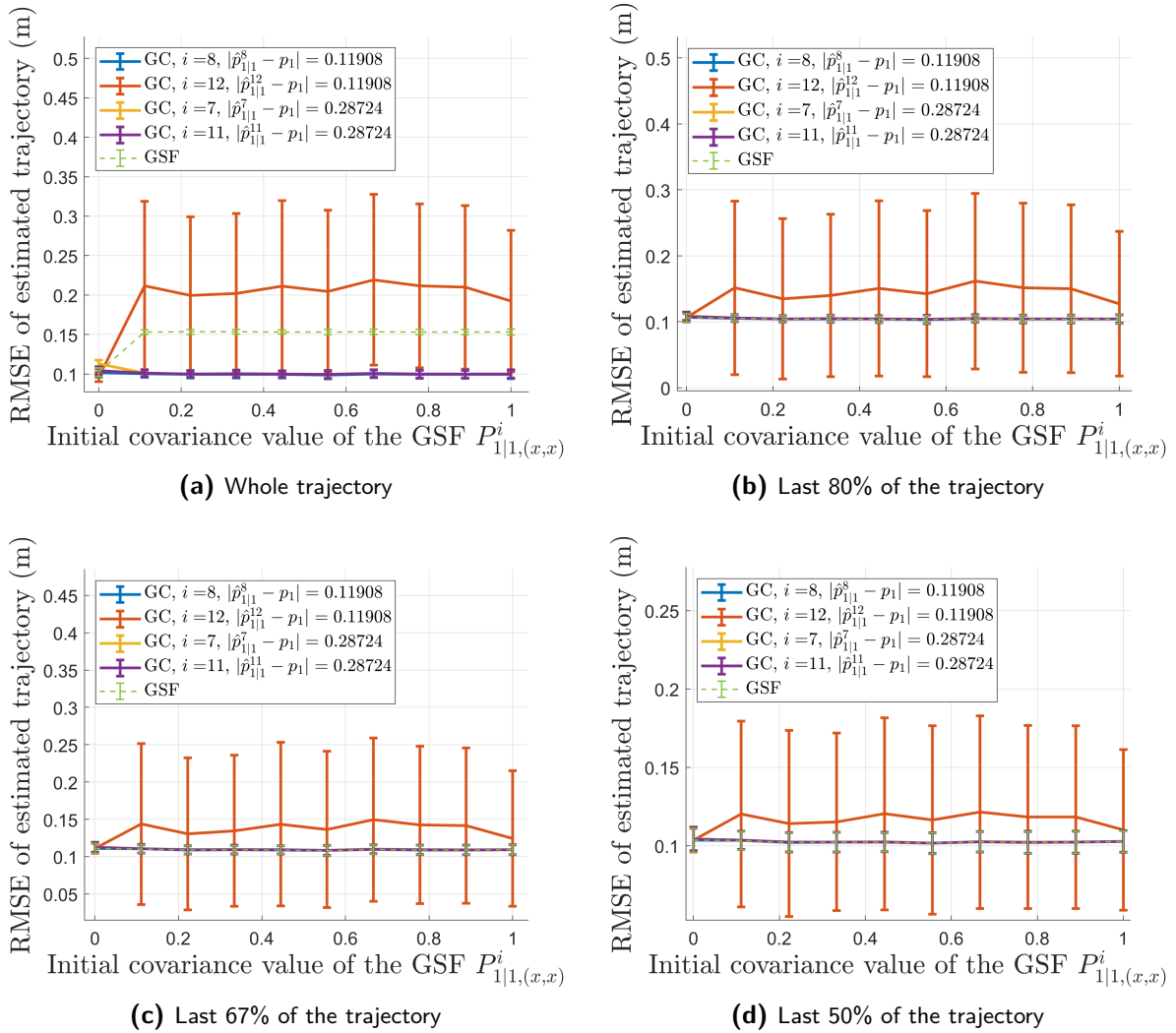
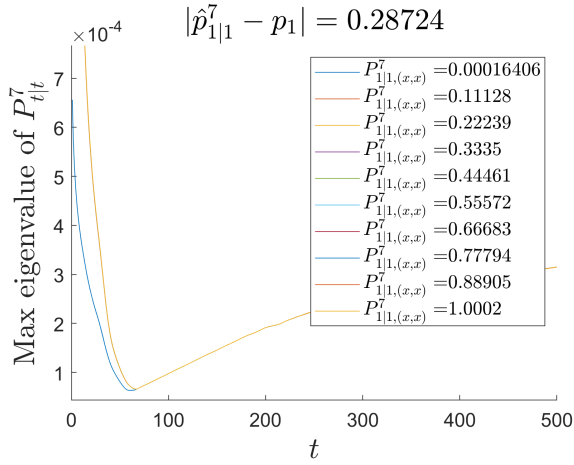
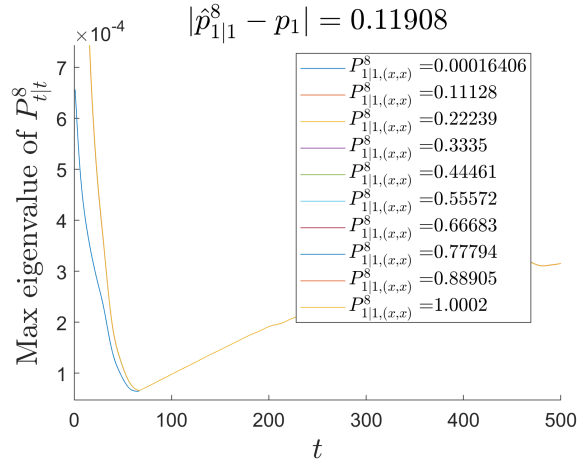


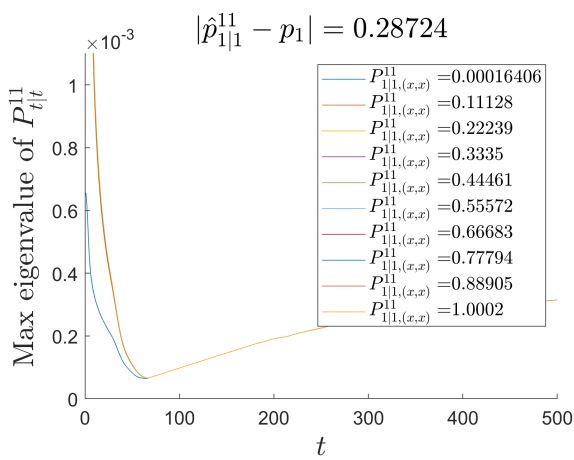
**Figure G-8:** The RMSE of the estimated trajectories of Gaussian components and the GSF under varied values of the initial covariances of the GSF  $P_{1|1}^i$



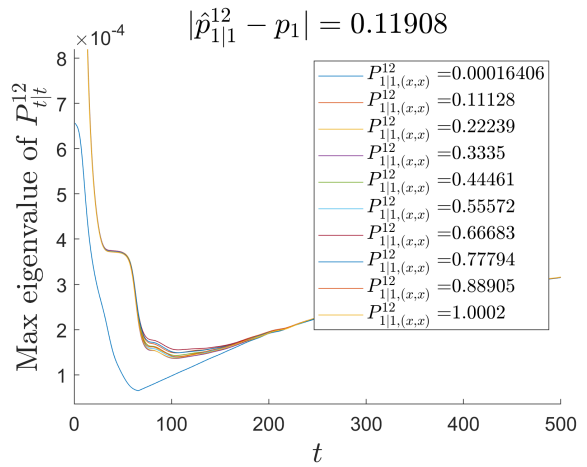
(a) Seventh Gaussian component



(b) Eighth Gaussian component



(c) Eleventh Gaussian component



(d) Twelfth Gaussian component

**Figure G-9:** The max eigenvalues of the covariance matrices change through time for different initial covariance values of the Gaussian components of the GSF



## Simulation results with measurement noise $\sigma_m$ set as 1

In Appendix B, it is mentioned that the results of the maps with different measurement noise  $\sigma_m$  are not significantly distinct. To show that the conclusions of the simulations applying different values of measurement noise  $\sigma_m$  are similar, the simulation results with the measurement noise set as 1 will be shown in this appendix.

The parameters that were applied for the reduced-rank Gaussian process (GP) magnetic field map are listed in Table H-1.

Range (m)	$l_{SE}$	$\sigma_{SE}$	Data size	$\sigma_m$
1.5	0.3	0.1	$\approx 5000$	1

**Table H-1:** Parameters for building the magnetic field map using reduced-rank GP

### H-1 Simulation results

The simulations run under the map settings shown in Table H-1 were mostly set as the same as introduced in Section 5-3, except for the initial error. The initial error for simulations in Section H-1-2 and H-1-3 were set to 0.25 to show the multimodality of the magnetic field localization system. Therefore, the introduction of the settings of the simulations will not be repeated here.

#### H-1-1 Varied initial error $\epsilon_0$

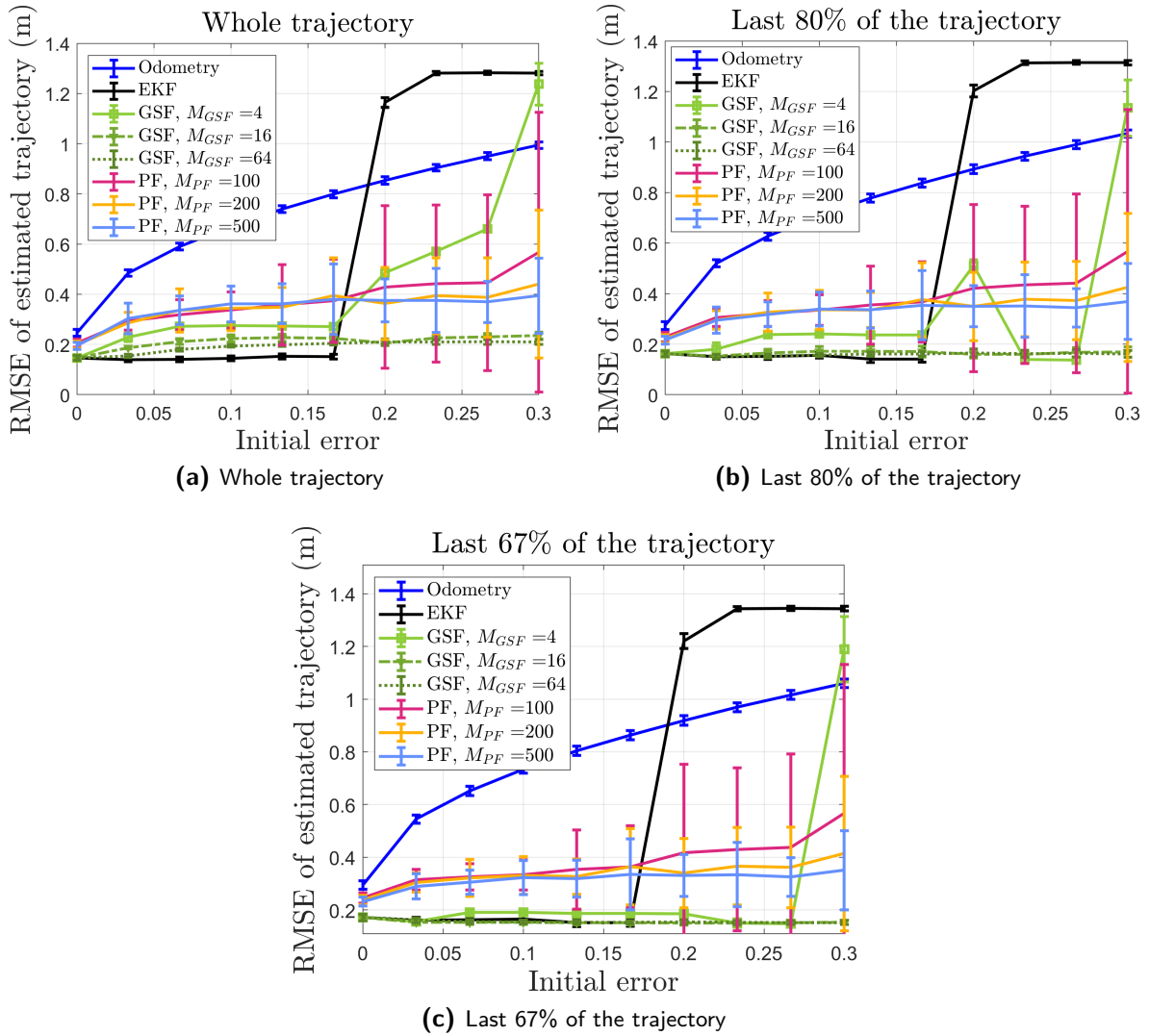


**Figure H-1:** The root mean squared error (RMSE) of the estimated trajectories of different algorithms under varied values of initial error  $\epsilon_0$

## H-1-2 Varied number of Gaussian components of the Gaussian sum filter (GSF)

$M_{GSF}$

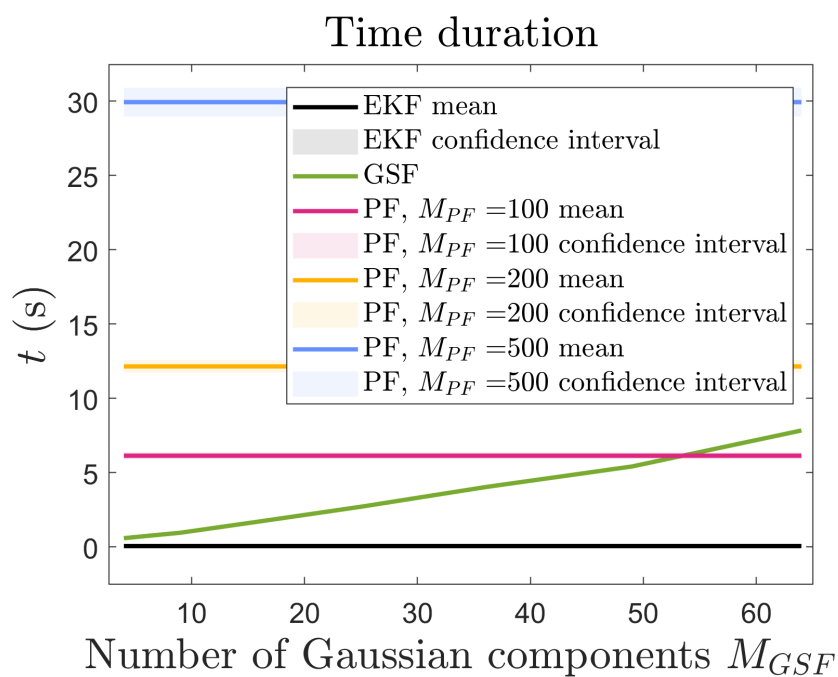


**Figure H-2:** Time duration of the algorithms under different values of the number of Gaussian components of the GSF  $M_{GSF}$

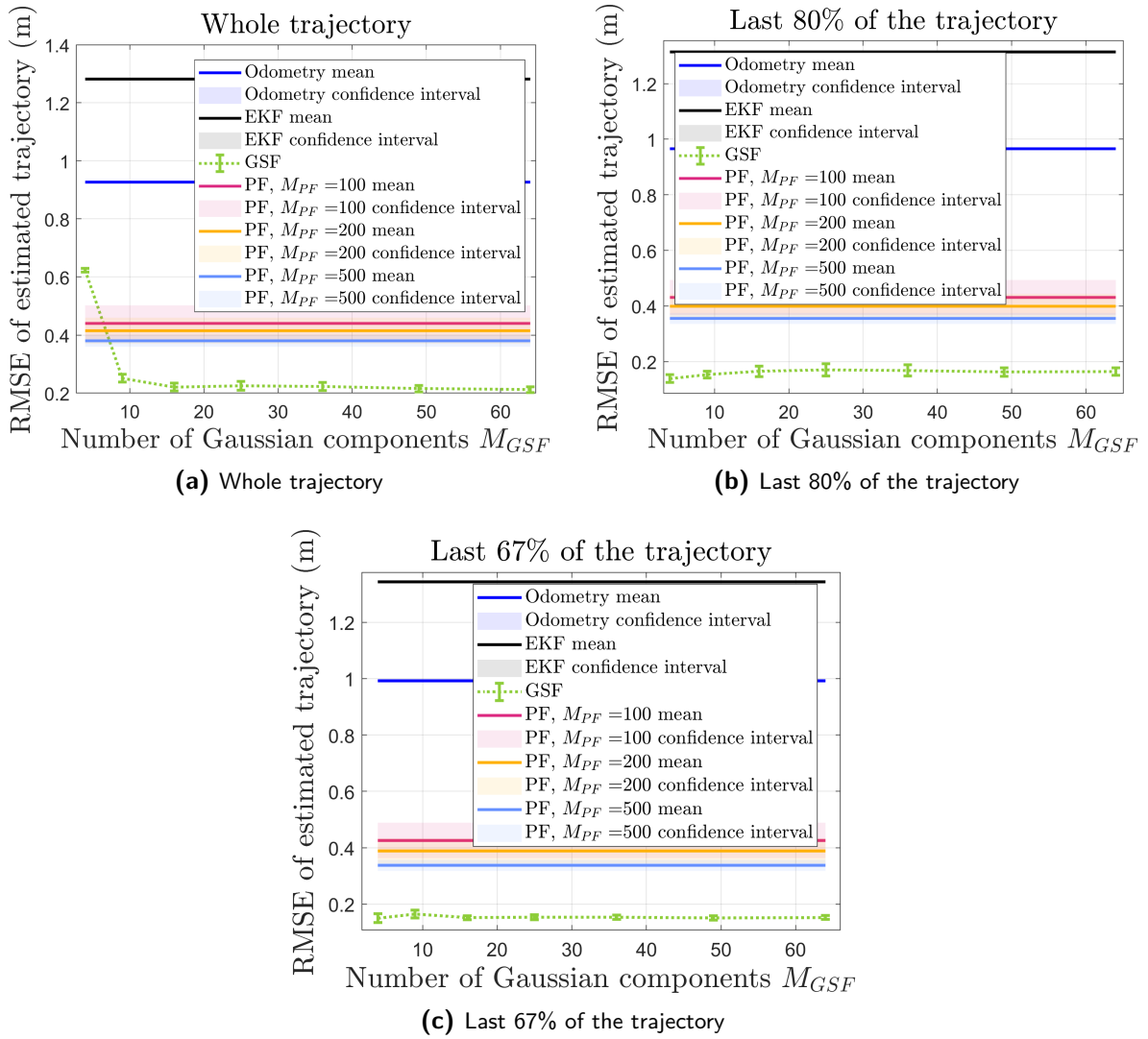


**Figure H-3:** The RMSE of the estimated trajectories of different algorithms under varied values of the number of the Gaussian components of the GSF  $M_{GSF}$

**H-1-3 Varied initial covariance matrices of the GSF  $P_{1|1}^i$**

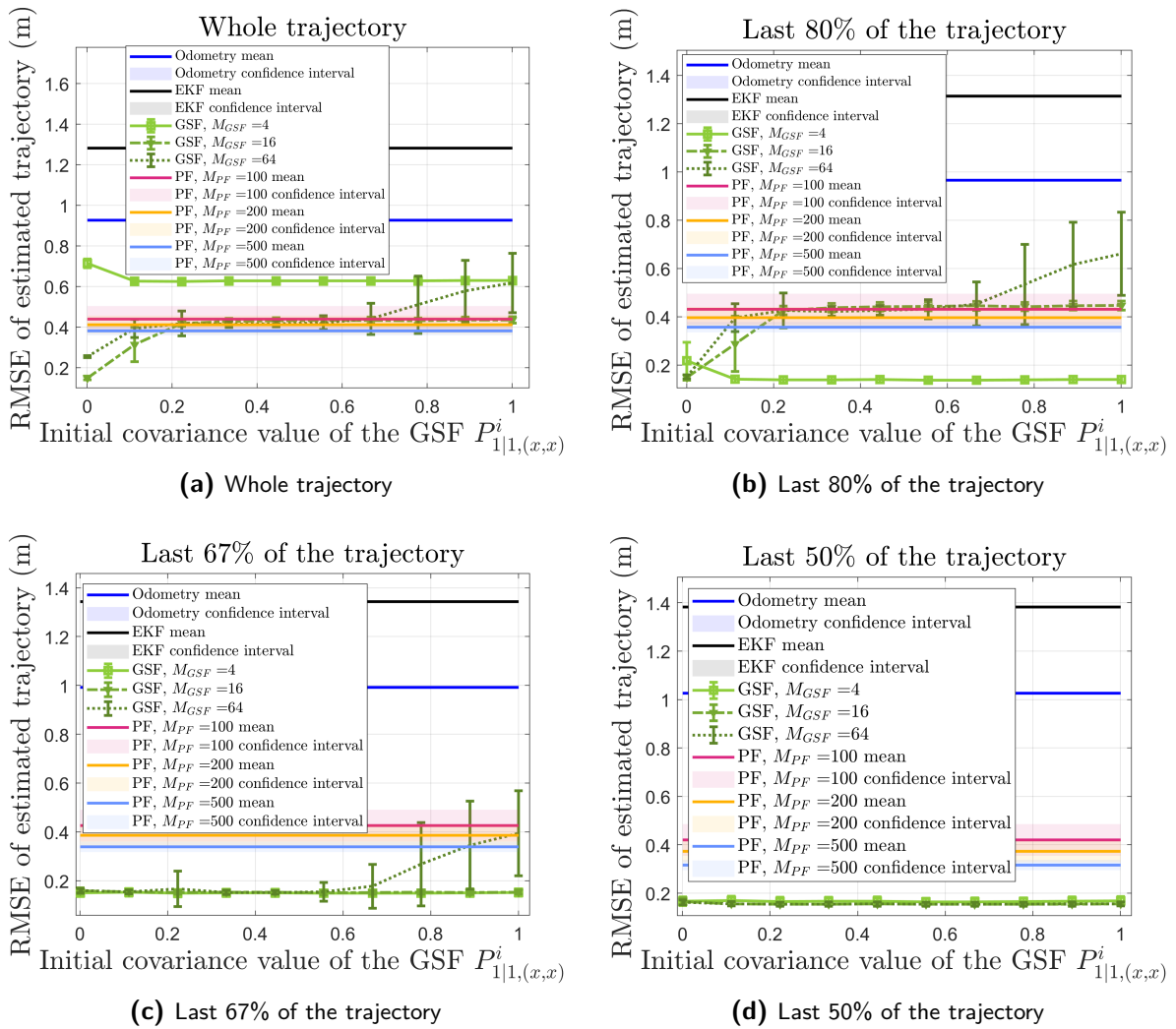


**Figure H-4:** The RMSE of the estimated trajectories of different algorithms under varied values of the initial covariances of the GSF  $P_{1|1}^i$



---

# Bibliography

- [1] Brian D. O. Anderson and John B. Moore. *Optimal Filtering*. Courier Corporation, May 2012.
- [2] M.S. Arulampalam, S. Maskell, N. Gordon, and T. Clapp. A tutorial on particle filters for online nonlinear/non-Gaussian Bayesian tracking. *IEEE Transactions on Signal Processing*, 50(2):174–188, February 2002.
- [3] Tímea Bagosi and Zoltan Baruch. Indoor localization by WiFi. In *2011 IEEE 7th International Conference on Intelligent Computer Communication and Processing*, pages 449–452, August 2011.
- [4] Luca Barbieri, Mattia Brambilla, Andrea Trabattoni, Stefano Mervic, and Monica Nicoli. UWB Localization in a Smart Factory: Augmentation Methods and Experimental Assessment. *IEEE Transactions on Instrumentation and Measurement*, 70:1–18, 2021.
- [5] Luka Batistić and Mladen Tomic. Overview of indoor positioning system technologies. In *2018 41st International Convention on Information and Communication Technology, Electronics and Microelectronics (MIPRO)*, pages 473–478, May 2018.
- [6] Michael Bloesch, Hannes Sommer, Tristan Laidlow, Michael Burri, Gabriel Nuetzi, Péter Fankhauser, Dario Bellicoso, Christian Gehring, Stefan Leutenegger, Marco Hutter, and Roland Siegwart. A Primer on the Differential Calculus of 3D Orientations, October 2016.
- [7] Eric Foxlin. Chapter 7. Motion Tracking Requirements and Technologies. *Handbook of virtual environment technology*, 8:163–210, 2002.
- [8] Brandon Gozick, Kalyan Pathapati Subbu, Ram Dantu, and Tomyo Maeshiro. Magnetic Maps for Indoor Navigation. *IEEE Transactions on Instrumentation and Measurement*, 60(12):3883–3891, December 2011. Conference Name: IEEE Transactions on Instrumentation and Measurement.

- [9] Fredrik Gustafsson. *Statistical Sensor Fusion*. Studentlitteratur, 2010.
- [10] Janne Haverinen and Anssi Kemppainen. Global indoor self-localization based on the ambient magnetic field. *Robotics and Autonomous Systems*, 57(10):1028–1035, October 2009.
- [11] Christopher J. Hegarty and Eric Chatre. Evolution of the Global Navigation Satellite System (GNSS). *Proceedings of the IEEE*, 96(12):1902–1917, December 2008.
- [12] Markus Heinonen, Henrik Mannerström, Juho Rousu, Samuel Kaski, and Harri Lähdesmäki. Non-Stationary Gaussian Process Regression with Hamiltonian Monte Carlo. In *Proceedings of the 19th International Conference on Artificial Intelligence and Statistics*, pages 732–740. PMLR, May 2016. ISSN: 1938-7228.
- [13] R. E. Kalman. A New Approach to Linear Filtering and Prediction Problems. In *Journal of Basic Engineering*, volume 82, pages 35–45, March 1960.
- [14] Sanket Kamthe, Jan Peters, and Marc Peter Deisenroth. Multi-modal filtering for non-linear estimation. In *2014 IEEE International Conference on Acoustics, Speech and Signal Processing (ICASSP)*, pages 7979–7983, May 2014.
- [15] Taeyun Kim, Jinwhan Kim, and Seung-Woo Byun. A Comparison of Nonlinear Filter Algorithms for Terrain-referenced Underwater Navigation. *International Journal of Control, Automation and Systems*, 16(6):2977–2989, December 2018.
- [16] Manon Kok, Jeroen D. Hol, and Thomas B. Schön. Using Inertial Sensors for Position and Orientation Estimation. *Foundations and Trends® in Signal Processing*, 11(1-2):1–153, November 2017.
- [17] Manon Kok and Thomas B. Schön. Magnetometer Calibration Using Inertial Sensors. *IEEE Sensors Journal*, 16(14):5679–5689, July 2016.
- [18] Manon Kok and Arno Solin. Scalable Magnetic Field SLAM in 3D Using Gaussian Process Maps. In *2018 21st International Conference on Information Fusion (FUSION)*, pages 1353–1360, July 2018.
- [19] Xinran Li and Mian Chen. Research of the Wireless Localization Technology Based on ZigBee. In *2012 Second International Conference on Business Computing and Global Informatization*, pages 699–701, October 2012.
- [20] Achille Murangira, Christian Musso, and Karim Dahia. A mixture regularized rao-blackwellized particle filter for terrain positioning. *IEEE Transactions on Aerospace and Electronic Systems*, 52(4):1967–1985, August 2016.
- [21] C. Musso and N. Oudjane. Particle methods for multimodal filtering. Application to terrain navigation. In *IEE Colloquium on Target Tracking: Algorithms and Applications (Ref. No. 1999/090, 1999/215)*, pages 6/1–6/5, November 1999.
- [22] Alwin Poulouse, Odongo Steven Eyobu, and Dong Seog Han. An Indoor Position-Estimation Algorithm Using Smartphone IMU Sensor Data. *IEEE Access*, 7:11165–11177, 2019.

- 
- [23] Alwin Poullose, Jihun Kim, and Dong Seog Han. Indoor Localization with Smartphones: Magnetometer Calibration. In *2019 IEEE International Conference on Consumer Electronics (ICCE)*, pages 1–3, January 2019.
- [24] Mark L. Psiaki, Jonathan R. Schoenberg, and Isaac T. Miller. Gaussian Sum Reapproximation for Use in a Nonlinear Filter. *Journal of Guidance, Control, and Dynamics*, 38(2):292–303, February 2015.
- [25] Jan Racko, Peter Brida, Arto Perttula, Jussi Parviainen, and Jussi Collin. Pedestrian Dead Reckoning with Particle Filter for handheld smartphone. In *2016 International Conference on Indoor Positioning and Indoor Navigation (IPIN)*, pages 1–7, October 2016.
- [26] Carl Edward Rasmussen and Christopher K. I. Williams. *Gaussian processes for machine learning*. Adaptive computation and machine learning. MIT Press, Cambridge, Mass., 3. print edition, 2008.
- [27] Patrick Robertson, Martin Frassl, Michael Angermann, Marek Doniec, Brian J. Julian, Maria Garcia Puyol, Mohammed Khider, Michael Lichtenstern, and Luigi Bruno. Simultaneous Localization and Mapping for pedestrians using distortions of the local magnetic field intensity in large indoor environments. In *International Conference on Indoor Positioning and Indoor Navigation*, pages 1–10, October 2013.
- [28] Arno Solin, Manon Kok, Niklas Wahlström, Thomas B. Schön, and Simo Särkkä. Modeling and Interpolation of the Ambient Magnetic Field by Gaussian Processes. *IEEE Transactions on Robotics*, 34(4):1112–1127, August 2018.
- [29] Arno Solin and Simo Särkkä. Hilbert space methods for reduced-rank Gaussian process regression. *Statistics and Computing*, 30(2):419–446, March 2020.
- [30] Arno Solin, Simo Särkkä, Juho Kannala, and Esa Rahtu. Terrain navigation in the magnetic landscape: Particle filtering for indoor positioning. In *2016 European Navigation Conference (ENC)*, pages 1–9, May 2016.
- [31] Yi Sun, Yubin Zhao, and Jochen Schiller. An autonomic indoor positioning application based on smartphone. In *2014 IEEE Wireless Communications and Networking Conference (WCNC)*, pages 3326–3331, April 2014.
- [32] Simo Särkkä. *Bayesian Filtering and Smoothing*. Cambridge University Press, September 2013.
- [33] Kostas Tsampourakis and Víctor Elvira. An Augmented Gaussian Sum Filter through a mixture Decomposition. In *ICASSP 2023 - 2023 IEEE International Conference on Acoustics, Speech and Signal Processing (ICASSP)*, pages 1–5, June 2023.
- [34] Burak Turan and Ali Türker Kutay. Particle filter studies on terrain referenced navigation. In *2016 IEEE/ION Position, Location and Navigation Symposium (PLANS)*, pages 949–954, April 2016.

- [35] Rudolph van der Merwe, Arnaud Doucet, Nando de Freitas, and Eric Wan. The Unscented Particle Filter. In *Advances in Neural Information Processing Systems*, volume 13. MIT Press, 2000.
- [36] Michel Verhaegen and Vincent Verdult. *Filtering and System Identification: A Least Squares Approach*. Cambridge University Press, 2010.
- [37] Frida Viset, Jan Tommy Gravdahl, and Manon Kok. Magnetic field norm SLAM using Gaussian process regression in foot-mounted sensors. In *2021 European Control Conference (ECC)*, pages 392–398, June 2021.
- [38] Frida Viset, Rudy Helmons, and Manon Kok. An Extended Kalman Filter for Magnetic Field SLAM Using Gaussian Process Regression. *Sensors*, 22(8):2833, January 2022.
- [39] Niklas Wahlström, Manon Kok, Thomas B. Schön, and Fredrik Gustafsson. Modeling magnetic fields using Gaussian processes. In *2013 IEEE International Conference on Acoustics, Speech and Signal Processing*, pages 3522–3526, May 2013.
- [40] Jie Xiong and Kyle Jamieson. ArrayTrack: A Fine-Grained Indoor Location System. In *10th USENIX Symposium on Networked Systems Design and Implementation (NSDI 13)*, pages 71–84, 2013.
- [41] Faheem Zafari, Athanasios Gkelias, and Kin K. Leung. A Survey of Indoor Localization Systems and Technologies. *IEEE Communications Surveys & Tutorials*, 21(3):2568–2599, 2019.
- [42] Yanhong Zhang, Dong Liu, Guangbin Liu, and Fei Cao. Gaussian sum filtering based on uniformly Random Design with application to terrain navigation. In *2011 4th International Congress on Image and Signal Processing*, volume 5, pages 2659–2663, October 2011.

---

# Glossary

## List of Acronyms

<b>IMU</b>	Inertial measurement unit
<b>KF</b>	Kalman filter
<b>EKF</b>	Extended Kalman filter
<b>PF</b>	Particle filter
<b>GSF</b>	Gaussian sum filter
<b>GM</b>	Gaussian mixture
<b>UGSF</b>	Uniformly random design based Gaussian sum filter
<b>GNSS</b>	Global navigation satellite system
<b>GPS</b>	Global positioning system
<b>RMSE</b>	root mean squared error
<b>pdf</b>	probability density function
<b>UPF</b>	Unscented particle filter
<b>SMSE</b>	Standardized mean squared error
<b>NLPD</b>	Negative log predictive density
<b>GP</b>	Gaussian process

